AFRL-VS-HA-TR-98-0015

DISCRIMINATION OF SEISMIC SOURCES USING ISRAEL SEISMIC NETWORK

Avi Shapira
Vladimir Pinsky
Yefim Gitterman

Geophysical Institute of Israel
P.O.B. 2286, Holon 58122
ISRAEL

November 1997

Final Report
June 1995-October 1997

DEPARTMENT OF ENERGY
Office of Non-Proliferation
  And National Security
WASHINGTON, DC 20585

AIR FORCE RESEARCH LABORATORY
Space Vehicles Directorate
29 Randolph Road
AIR FORCE MATERIEL COMMAND
HANSCOM AFB, MA 01731-3010

19980508 075

DTIC QUALITY INSPECTED 4

SPONSORED BY
Department of Energy
Office of Non-Proliferation and National Security

MONITORED BY
Air Force Research Laboratory
CONTRACT No. F19628-95-K-0006

REPORT DOCUMENTATION PAGE

1. AGENCY USE ONLY (Leave blank)	2. REPORT DATE November 1997	3. REPORT TYPE AND DATES COVERED Final Report (June 1995 – October 1997)

4. TITLE AND SUBTITLE **Discrimination of seismic sources using Israel Seismic Network** 6. AUTHOR(S) **Avi Shapira, Vladimir Pinsky, Yefim Gitterman**	5. FUNDING NUMBERS PE 69120H PR DENN TA GM WU AL Contract F19628-95-K-0006

7. PERFORMING ORGANIZATION NAME(S) AND ADDRESS(ES) **The Geophysical Institute of Israel P.O.B. 2286, Holon 58122 ISRAEL**	8. PERFORMING ORGANIZATION REPORT NUMBER 555/53/96(10)

9. SPONSORING/MONITORING AGENCY NAME(S) AND ADDRESS(ES) Air Force Research Laboratory 29 Randolph Road Hanscom AFB, MA 01731-3010 Contract Manager: James Battis/ VSBI	10. SPONSORING/MONITORING AGENCY REPORT NUMBER AFRL-VS-HA-TR-98-0015

11. SUPPLEMENTARY NOTES   This research was sponsored by the Department of Energy, Office of Non-Proliferation and National Security, Washington, DC 20585

12a. DISTRIBUTION/AVAILABILITY STATEMENT Approved for Public Release; Distribution Unlimited	12b. DISTRIBUTION CODE

13. ABSTRACT (Maximum 200 words)

We addressed the problem of automated event discrimination in both the local and teleseismic ranges using the Israel Seismic Network, as an example of a dense regional seismic network. A new high resolution technique was developed, based on multistation representation of the seismic signal: spectral semblance, measuring coherency of spectral shapes, and velogram, characterizing kinematic features. Semblance and energy spectral ratio statistics, applied to a wide variety of local and teleseismic events, showed, for specific spectral bands, almost total separation of explosions and earthquakes. Efficient automated classifiers based on combinations of different physical features of the events have been designed. The discrimination results for the teleseismic data were compared for the ISN and NORESS, showing almost equivalent performance. Noise recordings and teleseismic signals were used to evaluate the ISN detectability by array technique, including adaptive beamforming, optimal detectors, maximum likelihood estimators and phase correlation analysis, applied to the ISN subnetworks with promising results.

Experimental relationships between charge weight and magnitude for local single quarry shots and underwater Dead Sea explosions with outstanding high coupling were developed, providing a basis for the execution of effective calibration explosions currently lacking in the region.

14. SUBJECT TERMS Regional discrimination, seismic network, velogram analysis, spectra modulation and coherency, spectral ratios, multivariate discrimination procedures	15. NUMBER OF PAGES 90
	16. PRICE CODE

17. SECURITY CLASSIFICATION OF REPORT Unclassified	18. SECURITY CLASSIFICATION OF THIS PAGE Unclassified	19. SECURITY CLASSIFICATION OF ABSTRACT Unclassified	20. LIMITATION OF ABSTRACT SAR

TABLE OF CONTENTS

ILLUSTRATIONS

TABLES

APPENDIX A

ACKNOWLEDGEMENTS

PUBLICATIONS RESULTING FROM SPONSORSHIP OF THE CONTRACT:

Shapira, A., Gitterman, Y., Pinsky, V. and Malitzky, A., 1995. Detection, location and discrimination of seismic events by the Seismic Network of Israel, Proceedings, 17th Seismic Research Symposium on Monitoring a CTBT, September 1995, AZ, 911-919.

Gitterman, Y., Pinsky, V. and Shapira, A., 1996. Semblance and energy spectral statistics for discrimination of seismic events, Abstracts of the Annual Meeting of Isr. Geol. Survey, March, 1996.

Pinsky, V., Shapira, A. and Gitterman, Y., 1996. Multi-channel velogram analysis for discriminating between earthquakes and quarry blasts, 27th Nordic Seminar on Detection Seismology, XXV ESC General Assembly, September 1996, Reykjavik, Iceland, 581-586.

Gitterman, Y., Shapira, A. and Pinsky, V., 1996. Spectral semblance statistics as effective regional discriminants of seismic events in Israel, 27th Nordic Seminar on Detection Seismology, XXV ESC General Assembly, September 1996, Reykjavik, Iceland, 587-592.

Shapira, A., Gitterman, Y., and Pinsky, V., 1996. Discrimination of seismic sources using the Israel Seismic Network, Proceedings of 18th Seismic Research Symposium on Monitoring a CTBT, September 1996, Annapolis, 612-621.

Gitterman, Y. and Pinsky, V., 1997. Identification of Eurasian nuclear explosions recorded by the Israel Seismic Network, Abstracts of Annual Conference of the Israel Geological Society, Kefar Giladi, 15-17 April, 1997.

Gitterman, Y., Pinsky, V. and Shapira, A., 1997. Comparative Discrimination Analysis of Eurasian Nuclear Tests and Earthquakes Recorded by Israel Seismic Network and NORESS Array, Abstracts of the 29th General Assembly of the International Association of Seismology and Physics of the Earth Interior, August 18-28, 1997, Thessaloniki, Greece.

Pinsky, V., Gitterman, Y. and Shapira, A., 1997. Performance of the complexity discriminant applied to the Israel Seismic Network recordings from the nuclear test sites and earthquake sources, Abstracts of the 29th General Assembly of the International Association of Seismology and Physics of the Earth Interior, August 18-28, 1997, Thessaloniki, Greece.

Shapira, A., Pinsky, V., Gitterman, Y. and Malitzky, A., 1997. Improvements in Monitoring the CTBT in the Middle East by the Israel Seismic Network. Proceedings of the 19th Symposium on Monitoring a Comprehensive Test Ban Treaty, Orlando, 162-170.

Pinsky, V., Gitterman, Y. and Shapira, A., 1997. Multivariate discrimination of regional and teleseismic events, using the Israel Seismic Network recordings. Proceedings of the 19th Symposium on Monitoring a Comprehensive Test Ban Treaty, Orlando, 432-441.

Gitterman, Y., Pinsky, V. and Shapira, A., 1997. Application of spectral semblance and ratio statistics for discrimination of regional and teleseismic events recorded by ISN and NORESS, Proceedings of the 19th Symposium on Monitoring a Comprehensive Test Ban Treaty, Orlando, 369-378.

Gitterman, Y., Pinsky, V. and Shapira, A., 1997. Spectral classification methods in monitoring small local events by the Israel Seismic Network, approved for publication in the Journal of Seismology, Kluwer Publishers.

Gitterman, Y., Ben-Avraham, Z. and Ginzburg, Z., 1997. Spectral analysis of underwater explosions in the Dead Sea, Submitted to the Geophys. J. Int.

Pinsky, V. and Shapira, A., 1997. Kinematic Multistation Discriminator Between Local Quarry Blasts and Earthquakes, Submitted to the Geophys. J. Int.

SUMMARY

The regional and teleseismic signals from a set of short period stations of the Israel Seismic Network were investigated with the primary objective of seismic source discrimination. The regional database includes 212 ripple-fired and single shot quarry blasts, underwater explosions and earthquakes of local magnitudes M_L=1.0-3.1, at distances 5-250 km from various areas in Israel, Jordan and the Mediterranean Sea. Teleseismic data consist of 68 earthquakes and nuclear tests from Eurasia (m_b=5.2÷6.5). Also included in the study are NORESS recordings, comprising 36 events, almost completely intersecting with ISN dataset.

The multichannel seismograms and their smoothed spectra, calculated for the whole signal, demonstrate several specific features (S-wave group velocity, coherency of spectral shapes, spectral energy distribution) essentially different for regional earthquakes, quarry blasts and underwater explosions. These features were used to construct several new efficient scalar and vector statistics calculated in specific frequency bands: *spectral semblance (SS), energy spectral ratio (SR)* of low and high frequencies and *spectrograms*, as well as *velogram parameter C (VPC)* estimated in the time domain.

Owing to dominant low-frequency, low-velocity surface waves and source spectral modulation in seismograms, quarry blasts and underwater explosions showed, as a rule, higher SR and SS values, and lower VPC as compared to local earthquakes. Different frequency bands were tested: the ratio (1-3 Hz)/(6-8 Hz) and semblance (1-12 Hz) provided the best discriminant performance, with a success rate of 97% for the whole database.

The majority voting as well as automatic classifiers: the Fisher Linear Discrimination Function (LDF) and the non-linear Artificial Neural Network (ANN) applied to combinations of the above mentioned discriminants, were tested on quarry blasts and earthquakes in three separate regions of Israel and Jordan. The performance of the different classification schemes, determined by the {classifier, parameter vector} pair, was compared on the basis of error probability estimation using the leave-one-out cross-validation procedure. The best result, with an error probability of 0.006, was achieved when ANN was applied to the 5-band *spectrogram* in the (1-11 Hz) frequency range, averaged over an ISN subnetwork.

The SS, the SR and the ratio of *P/P-coda* spectral maxima were effective for classification of teleseismic events. Contrary to observations of local data, SS and SR values calculated from ISN seismograms in time windows containing P and P-coda waves, are higher for earthquakes. The best performance is provided in the frequency ranges (0.6-1 Hz)/(1-3 Hz) for SR and (0.6-2 Hz) for the SS. Joint application of the two discriminants showed 95% separation between the two populations. None of the individual statistics resolved nuclear tests

and earthquakes completely, but *majority voting* on some combinations provided total separation. The *leave-one-out* cross-validation test revealed the LDF as the best automatic classifier (only one misidentification for the dataset without deep earthquakes).

Teleseismic ISN and NORESS array discrimination performances were compared. The NORESS records showed the same (as the ISN) relation between *SR* values for earthquakes and explosions, whereas the character of *SS* was reversed. By applying (0.6-0.8 Hz)/(0.6-10 Hz) ratio, we obtained full separation of the two populations. In general, *SR* performance appears to be better for NORESS recordings, whereas *SS* is better for the ISN data.

We tested array methods, applied to the different ISN configurations and investigated teleseismic detectability and slowness estimation. The standard beam (SBT) and adaptive beamforming technique (ABT) were compared for ISN subnetworks containing 7-16 stations. Theoretical analysis and experimental results yielded that only ABT is capable of improving the detectability, providing the best SNR at the output. Estimation of slowness using the adaptive optimal detector, maximum-likelihood onset estimator and phase correlation analysis, provided deviation of slowness as <0.003 sec/km and azimuth <0.5° for two small events ($m_b \leq 5.4$).

Some physical phenomena and experimental properties related to local explosive sources were analyzed based on ISN recordings. Unique spectral features of seismic waves from the deep experimental detonations in the Dead Sea, caused by source (bubble oscillation) and path propagation (reverberations) effects, were observed and interpreted. The two effects produce a distinct spectral modulation by two series of harmonics at frequencies corresponding well to those estimated from the source parameters and the physical properties of the Dead Sea water.

Seismic efficiency of local explosions and peak amplitude attenuation were experimentally investigated. A clear correlation between charge weight and magnitude is observed for instantaneous quarry shots and single underwater explosions (unlike ripple-fired blasts with specific delays and geometry). A dependence of peak particle velocity on the scaled distance was evaluated. A high coupling for Dead Sea UWE is also observed: an 0.3 ton charge corresponds to $M_L=3.1$, exceeding magnitude values of quarry blasts of several dozens tons. This observation should be considered when planning calibration explosions, currently lacking in the region, and necessary for the improvement of CTBT monitoring. According to the equations developed, a Dead Sea UWE of 5,000 kg will "produce" $M_L > 4.0$ and might be observed at distances up to 2600 km, i.e. might be recorded by most of seismic stations and local networks operating in the Eastern Mediterranean and Middle East.

1. INTRODUCTION

Seismological means of detecting and identifying nuclear tests are the most powerful methods, but still need further improvement. Under the Comprehensive Test Band Treaty (CTBT), monitoring of seismic events as small as $m_b=2.5$ may become a crucial issue (Wallace et al., 1992), especially when considering evasion scenarios such as decoupling (Murphy et al., 1987). The weak events, including those resulting from human activities such as construction and mining, must be discriminated from nuclear explosions (Stump et al., 1994).

The wavefields of these small events are only well recorded at regional distances, thus attracting interest to regional seismic networks. The ISN is one of the best in the Middle East, where international studies concerning the CTBT have just begun. Physical factors affecting regional discrimination of man-made and natural seismic events (generation of dominant low-frequency surface waves by quarry blasts, associated with subsurface sediments; differences in spectral content, kinematic parameters of seismograms and spatial coherency of spectral shapes) were investigated by Kafka (1990), Båth (1975), Alexander et al. (1995), Gitterman and van Eck (1993) and others. The physical phenomena observed at a regional dense seismic network, provide a basis for development of efficient classification algorithms, optimally accounting for the multichannel character of the system.

A successful Integrative Approach using majority voting, artificial neural network, linear Fisher and other multivariate classifiers applied to combinations of discriminants, was demonstrated (e.g. Wuster, 1993; Pully, 1995 and Dowla, 1995) to further enhance the resolving power of discrimination. The optimal parameter vectors and best classifier algorithms can be elaborated on the basis of error probability estimation (Tsvang et al., 1993) through a leave-one-out cross-validation procedure (Fukunaga and Hummels, 1989).

The ISN potential to contribute to teleseismic monitoring has not been evaluated. Enhancement of the ISN detectability can be achieved through the application of the array technique to its subnetworks. New adaptive optimal detector and beamforming (Kushnir et al., 1990) together with phase-correlation technique (Gelchinsky et al., 1985) were applied to the data yielding additional noise suppression and accurate slowness estimates for precise location of weak teleseismic events.

A number of CTBT studies claim lack of calibration explosions in the Middle East region and, in particular, for areas along the Dead Sea transform (Baumgardt, 1996). Design and execution of such experiments require empirical assessment of explosion effectivity and attenuation of seismic waves for regional geological and geotechnical settings.

2. DATABASE.

2.1 Regional Events.

Regional data include seismograms from 212 quarry blasts, underwater explosions (UWE) and local earthquakes of magnitudes M_L=1.0-2.8 and depths H=0-28 km from geologically different areas in Israel, Jordan and the Mediterranean Sea. The events were recorded at distances of 5-250 km by the vertical short-period stations of the Israel Seismic Network (50 Hz sampling rate, 0.2-12.5 Hz bandpass filtering). We examined all the traces and eliminated records that appeared to be affected by glitches, spikes, noise bursts, or malfunctions. Most explosions were supplied by ground-truth information acquired from quarry operators. Basic parameters of the selected events and information about the quarries are presented in Tables 1 and 2 and the locations are shown on a map (Fig. 1). Complete information, regarding earthquake parameters, blast ground-truth information and event numbers used in this report, is available from the Scientific Report No. 1 (Gitterman et al., 1996b); data about Jordanian quarries are taken from the USGS report (Wilburn et al., 1996).

Table 1. Local database used in the study

#	Region, dataset	Number of Earthquakes	Number of Explosions	Comments
1	Galilee, Northern Israel	30	39	Earthquake depth H = 0-21 km Quarry blasts: W=2000-14000 kg
2	Southern Dead Sea and Negev desert, Israel	16	26	H = 0 - 24 km Quarry blasts W=1700-10500 kg
3	Gilad region, Jordan, Israel-Jordan border	19	15	H = 2 - 18 km Quarry blasts - no GTI
4	Tyre region, Mediterranean sea	8	16	H = 6 - 17 km UWE - unauthorized fishing, no Ground Truth Information
5	Dead Sea basin, seismic refraction profile	-	28	UWE for seismic prospecting depth h = 70 m; W=16-304 kg
6	Jordan/Saudi Arabian border	-	5	Jordanian quarry blasts W = 15000-17000 kg
7	Quarries Revaya, Mt. Nitzim	-	10	Single quarry blasts (no delays) W = 900 - 2800 kg
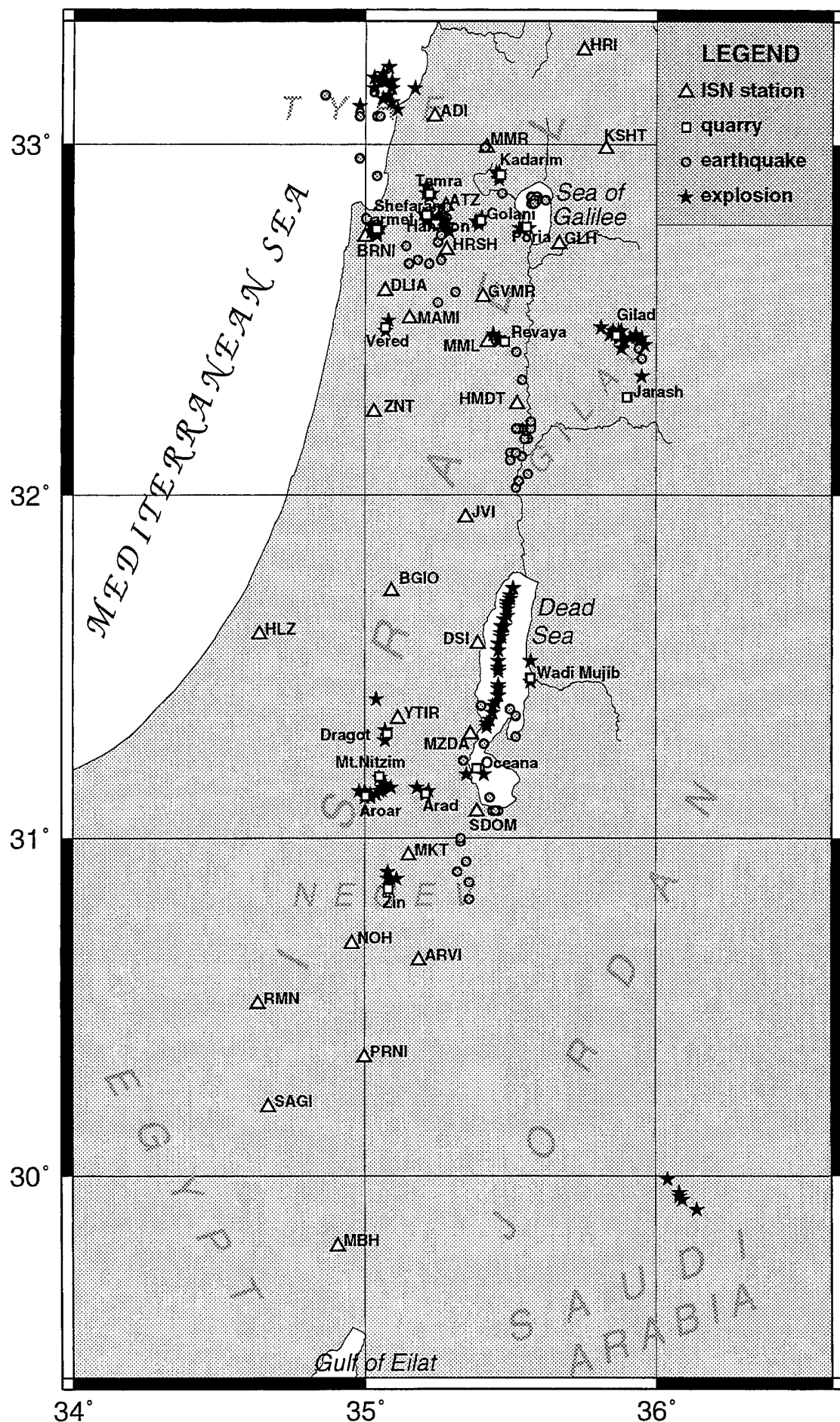
Fig. 1. Locations of ISN stations, quarries and local seismic events used in the study.

Table 2. Information about open-pit quarries presented in the study.

#	NAME	CODE	LAT.	LONG.	PRODUCT
ISRAEL					
1	Aroar	aror	31.125	35.003	phosphates
2	Carmel	nshr	32.758	35.040	dolomites (construction, roads)
3	Dragot	drgt	31.309	35.078	phosphates
4	Golani	goln	32.782	35.397	aggregate, blocks, beton
5	Hanaton	hntn	32.773	35.241	dolomites (construction, roads)
6	Kadarim	kdar	32.913	35.465	limestone, dolomite (construction, roads)
7	Mt.Nitzim	ntzm	31.184	35.051	calcium carbonates
8	Oceana	ocea	31.208	35.385	salt aggregates
9	PhosphArad	arad	31.131	35.210	phosphates
10	PhosphZin	pzin	30.851	35.082	phosphates
11	Poria	pori	32.764	35.553	basalt, aggregate, asphalt, beton
12	Revaya	rvya	32.439	35.480	limestone (construction, roads)
13	Shefaram	shfr	32.797	35.211	aggregate, asphalt, beton
14	Tamra	tmra	32.858	35.220	carbonate, chalk, cement
15	Vered	verd	32.479	35.069	dolomites
JORDAN					
1	Jarash		32.28	35.90	stone
2	Wadi Mujib		31.47	35.57	gypsum, sulphur
3	Gilad		32.46	35.86	stone

Some of the collected data are included in the Ground-Truth Database (GTDB), developed by Multimax and presented on the Web site (see Fig. 2):

http://es1.multimax.com/~gtdb/galilee/index.html

(Grant et al., 1997). The data were used by other researchers in a discrimination study (Walter et al., 1997) and in an estimation of chemical explosions effectivity (Khalturin and Richards, 1997)

6

select earthquakes or quarry blasts from the maps below
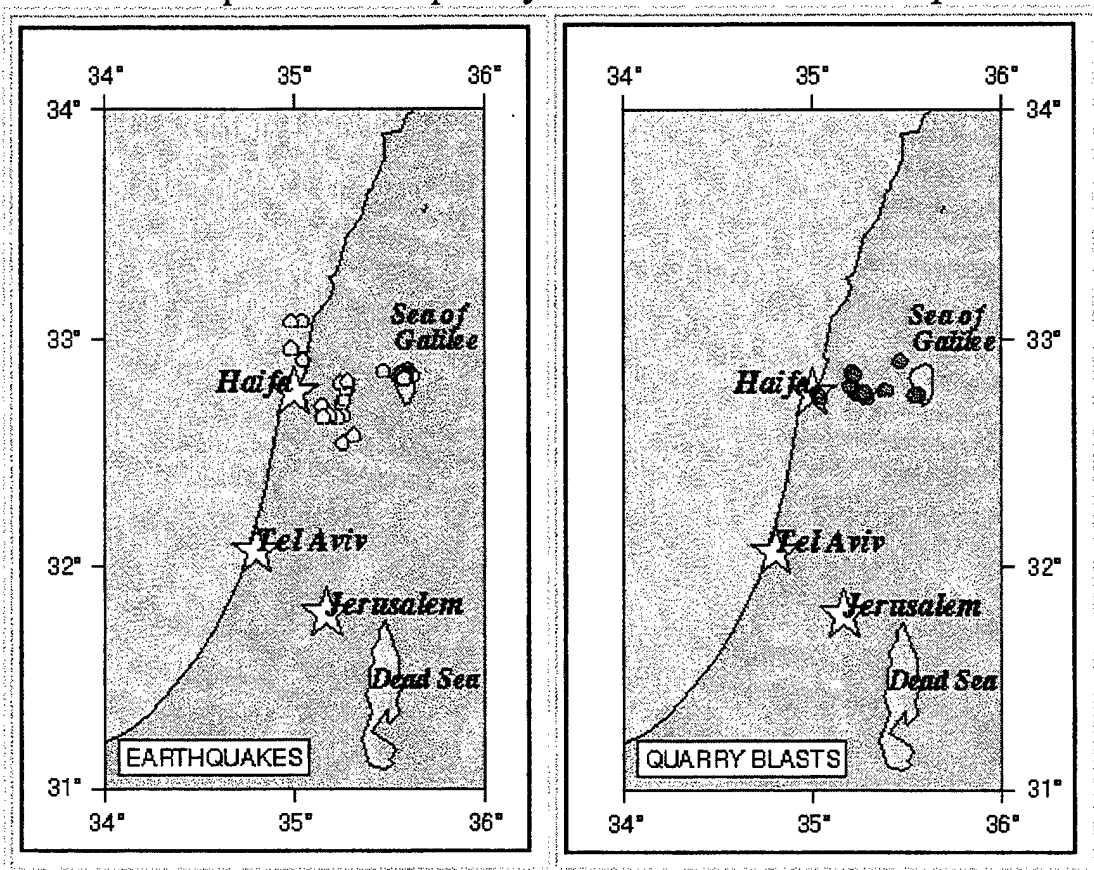
[**Earthquakes** | **Quarry Blasts**]

How to Get the Galilee Data Set

About the Israeli Seismic Network   About the Galilee Dataset

Galilee Home | News | Credits | References

lori@otter.mmiwest.com

Fig. 2. The Web page prepared by Multimax with Israel local events selected and checked in the project.

Spectral computations, necessary for estimating spectral discriminants used in the study, are made for a time window of about 20-30 sec, which is the same for all stations for a fixed event, and includes the whole signal up to the end of the coda waves. This window was selected to avoid picking out separate wave phases at short distances and accumulated information regarding source features being kept in all wave forms, thus enhancing the resolving power of the discriminants considered. The spectra were instrument-corrected and smoothed in a fixed 0.5 Hz moving window to provide equivalent spectral resolution for different stations.

2.2 Teleseismic Events

The teleseismic database consists of 29 nuclear tests from the test sites in China (Lop Nor), Kazakhstan (Semipalatinsk), and Russia (W. Siberia, N.Zemlya), 12 deep (H>50 km) earthquakes from Afghanistan and 27 shallow earthquakes from China and Tajikistan. These events were recorded by the ISN and their magnitudes are in the range $m_b=5.2 \div 6.5$. (For several Chinese nuclear explosions, we used in addition recordings of the Israel broad-band station BGIO). In parallel, during the visit to NORSAR we collected and processed NORESS seismograms of 20 explosions and 14 earthquakes and two additional earthquakes (non-readable on ISN tapes). Other events available to the ISN were inaccessible in the NORESS database. Detailed source information is presented in Tables 3 and 4; event locations are shown on Fig. 3. Location, origin time, magnitude (m_b) and focal depth are taken from PDE (NEIC) bulletins, distance and azimuth are calculated relative to the station BGIO of the ISN.

The records (2-2.5 minutes in length) contain only P-wave and P-coda waves owing to the restricted recording time of the acquisition system. A time window about 13-15 sec comprising the P-signal, was used for the spectral analysis, the spectra were smoothed in 0.2 Hz window. ISN spectra were instrument-corrected.

3. ANALYSIS OF LOCAL EXPLOSIVE SOURCES.

3.1 Some Spectral Features of Underwater Explosions in The Dead Sea.

A series of single-shot underwater explosions with charges of W=16-304 kg was detonated in the Dead Sea at a depth of d=70 m. For the analysis we selected a representative dataset of 28 explosions of four different charge sizes, distributed uniformly along a line in the middle of the northern basin of the Dead Sea (see map in Fig. 1).   Ground-truth information,

Test sites & earthquakes
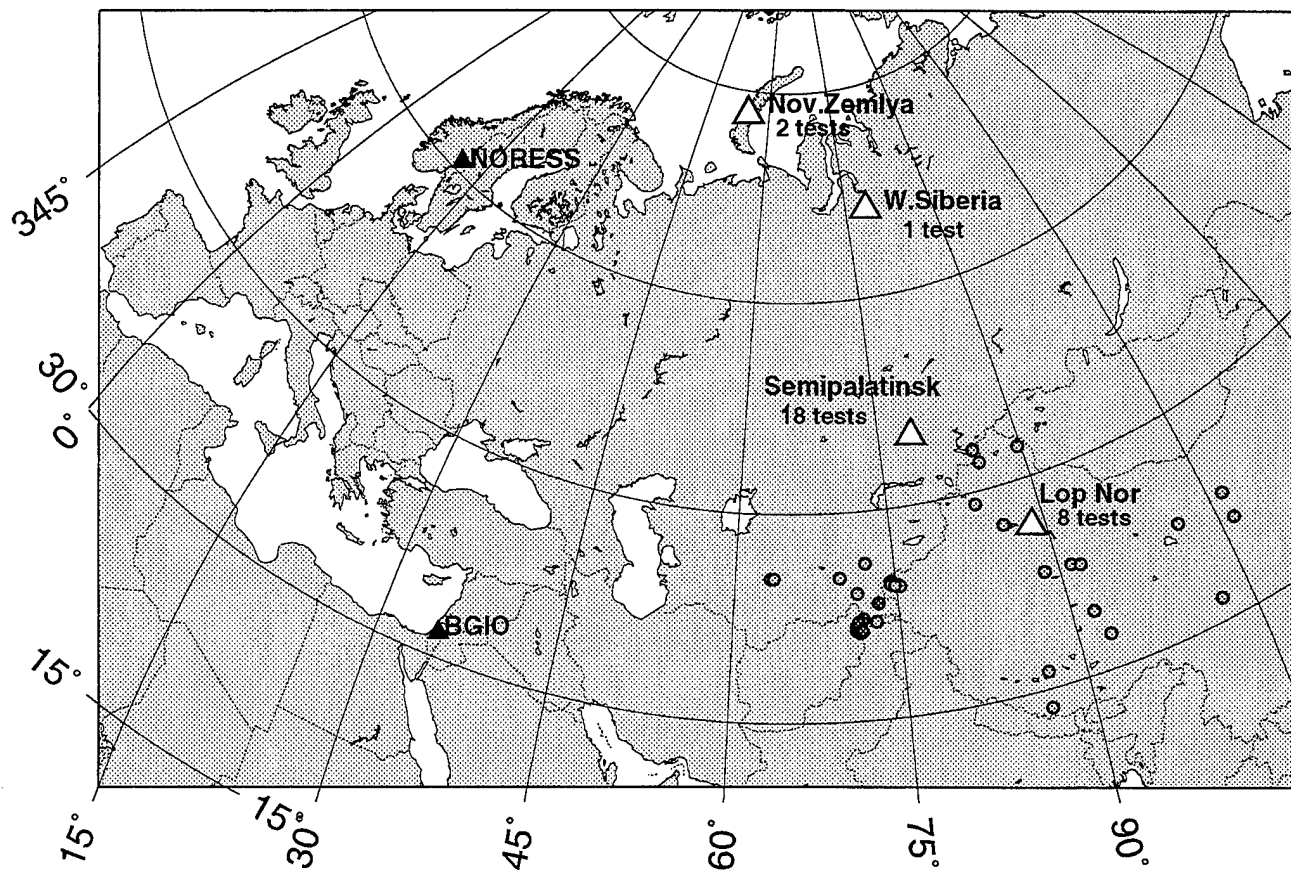
Fig. 3. Locations of nuclear test sites and teleseismic events used in the study. Deep
(Afghan) earthquakes are indicated by darker circles. Israel Seismic Network is
indicated by the station BGIO (Bar-Giyyora) placed in the middle of ISN.

including accurate coordinates, charge weight, shot depth and local time of explosions is presented in Gitterman et al. (1996).

Detonations in deep water produce seismic waves bearing spectral features caused by the source (bubble oscillation) and path propagation effect (reverberations). The bubbling effect produces a low-frequency azimuth-invariant spectral modulation as the complete harmonic series of spectral maxima with a fundamental frequency f_{1b}, which is characterized by the detonation depth, d (m), and the explosive yield, W (kg of TNT) (see e.g. Willis, 1963):

$$f_b = (d+10)^{5/6} / (2.1 W^{1/3}); \quad f_{nb} = n * f_b, \quad n = 1, 2,... \qquad (3.1)$$

The bubbling actually affects all types of recorded seismic waves throughout the entire wavetrain shown in Fig. 4, but is better manifested in spectra of the initial body-wave portion (P and P-coda). A complete harmonic series (3, 6, and 9 Hz) resulting from the bubbling effect is presented in Fig. 5a for the largest explosion EX1 with charge weight W=304 kg. Spectra of the whole signal are much more complicated and mixed with reverberations maxima (Fig. 5b), however low-frequency spectral modulation minima (4.5 and 7.5 Hz), corresponding to the bubbling interference, are sharpened and expressed more distinctly.

Using ground truth information and taking into account the high density of salt water in the Dead Sea i.e. $\rho \approx 1.11$ gr/cm^3 compared to the usual $\rho \approx 1.03$ gr/cm^3 (Prof. Z. Ben-Avraham, oral communication) we estimated from Eq. 3.1 the fundamental bubbling frequency for explosion EX1 as $f_b \approx 2.9$ Hz. This corresponds well to the observed value ~3.0 Hz presented in Fig. 5a. (The usual density yields an estimate $f_b \approx 2.7$ Hz).

In contrast to the complete harmonic series caused by the bubbling effect, water reverberations produce two odd harmonic series with fundamentals f_H and f_d (Weinstein, 1968):

$$f_H = V_0/4H, \quad f_{nb} = (2n-1) * f_b, \quad n = 1, 2,... \qquad (3.2)$$

$$f_d = V_0/4d, \quad f_{nb} = (2n-1) * f_b, \quad n = 1, 2,... \qquad (3.3)$$

where H is the water depth in meters and d is the detonation depth in meters.

For the P velocity in the Dead Sea $V_0 \approx 1770$ m/sec, and for an average depth of $H \approx 310$ m (Neev and Hall, 1979), we estimated from Eqs. 2 and 3, $f_H \approx 1.4$ Hz, and $f_d \approx 6.3$ Hz. The spectral modulation caused by reverberations is better manifested in the spectra of the
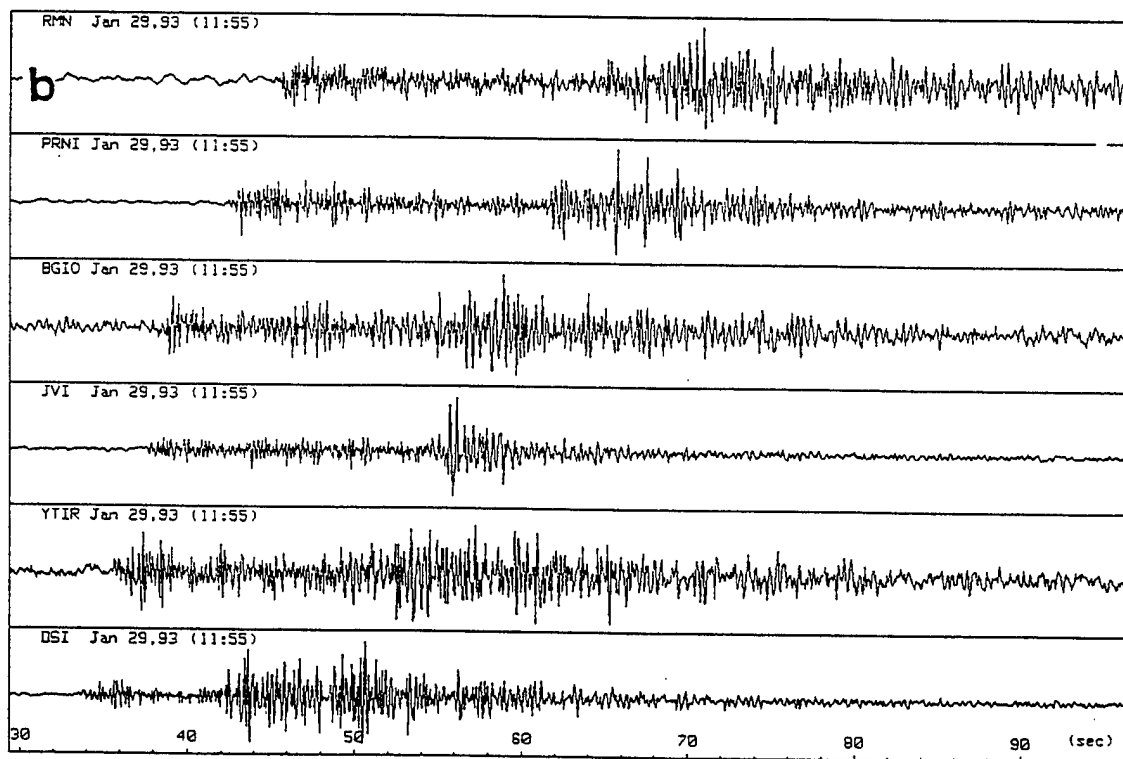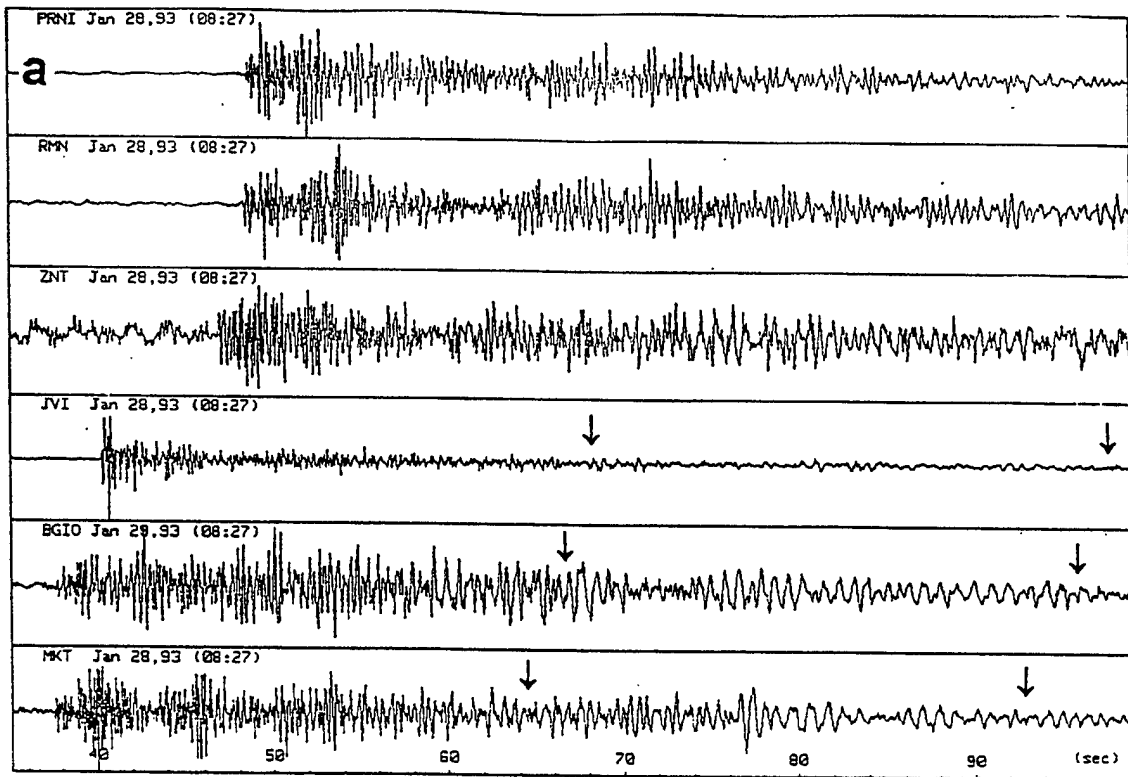
Fig. 4. Seismograms of Dead Sea underwater explosions: (a) the largest explosion EX1 with charge weight W=304 kg; arrows show a coda window used in the analysis (see Fig. 5c); (b) a small explosion EX13 showing some earthquake wave features (e.g. the largest amplitudes of the S/Rayleigh arrivals at each station). Amplitudes at this and following figures are not scaled.

11
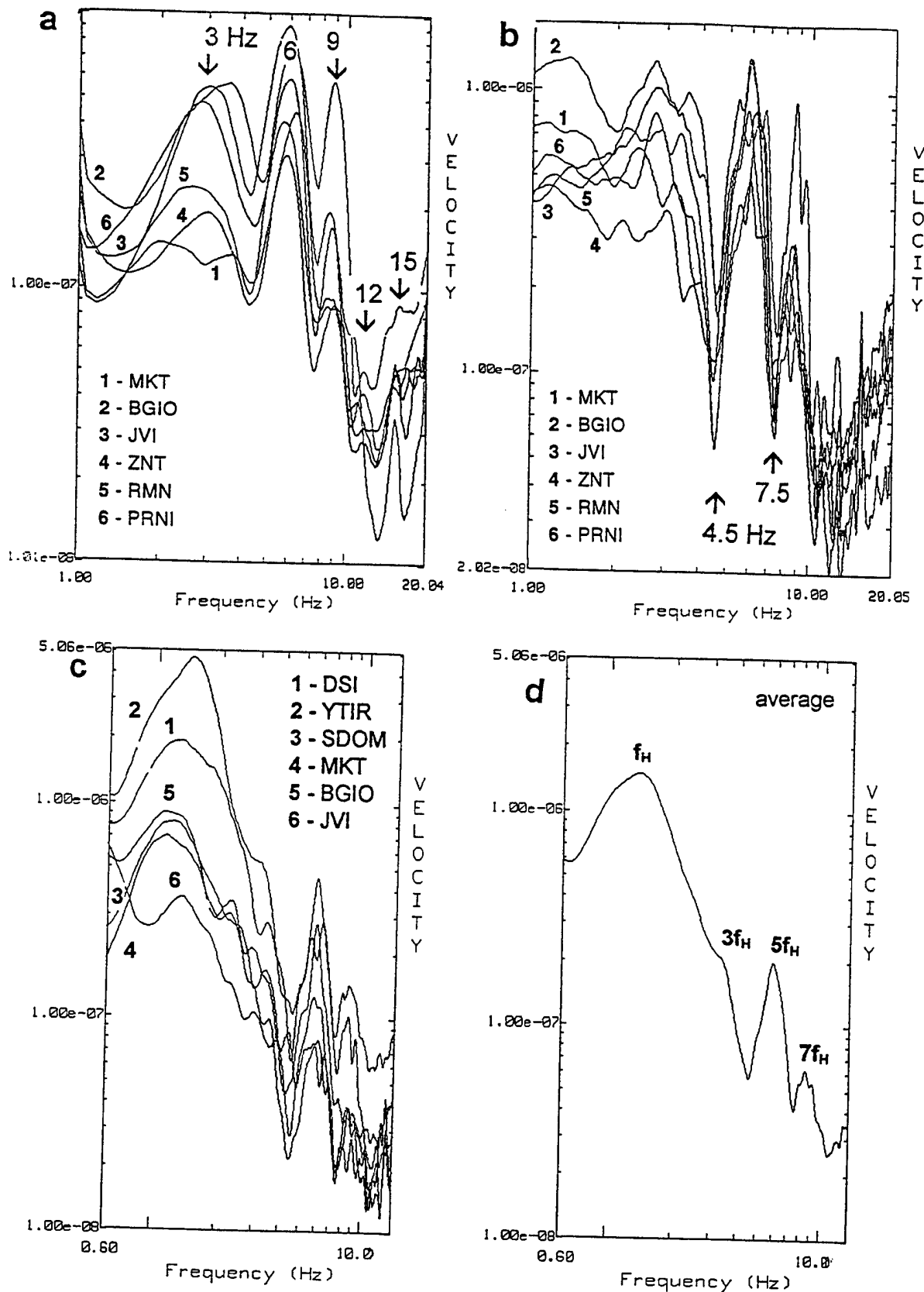
Fig. 5. Smoothed spectra for EX1 at several stations for various time windows: (a) the first 8 sec of P and P-coda waves; (b) the whole signal (about 60 sec); (c) a coda window (about 30 sec), marked on Fig. 4a; (d) an average spectrum for the coda window. An outstanding spectral modulation is observed due to the bubbling effect (a,b) and reverberations (c,d).

12

coda window shown on Fig. 4a. The spectra on Fig. 5c,d demonstrate distinct maximum frequencies, fitting the estimated f_H, odd harmonics $5f_H$ and $7f_H$ and a less visible harmonic $3f_H$. A noticeable maximum at about 6 Hz contains supposedly joint contributions of the close $5f_H$ (7 Hz), f_d (6.3 Hz) and $2f_b$ (5.8 Hz) harmonics.

Correct interpretation of spectral features of recorded seismic waves is useful in evaluating energy distribution in the frequency domain depending on different effects, source and medium parameters and, thus, in estimating spectral discriminants performance.

Simple comparison of the seismograms of explosions (Fig. 4a) and earthquakes (Fig. 6a) shows differences that are due to features of the source. For the "typical" earthquake seismograms the S/Rayleigh waves can usually be identified and have the largest amplitudes at each station. For "typical" explosions (especially for UWE), the largest amplitudes are usually in the P-group with S/Rayleigh onsets being difficult to identify. However, there are some events which demonstrate anomalous amplitude characteristics; for example, a small explosion EX13 shows some earthquake wave features, i.e. the largest amplitudes of the S/Rayleigh arrivals at each station (Fig. 4b) and explosion-like wave features for an earthquake QS12 can be observed (Fig. 6b). For reliable identification of seismic events in the region, therefore, simple visual analysis of seismograms is not sufficient and require additional spectral analysis

3.2 Experimental Relationships of Explosion Effectivity and Attenuation.

There are well established correlations between the magnitude and yield of underground nuclear explosions for different test sites (e.g. Ringdal et al., 1992):

$$m_b = 4.45 + 0.75 * \log_{10} Y_{(kton)} \qquad (3.4)$$

We have checked similar relations for different types of blast sources presented in our database. Most studies of ripple-fired quarry blasts show no correlation between total charge weight of a blast and magnitude (or PGV - peak ground velocity), one example is the investigation by Jarpe et al. (1996), who studied production and waste shots of 10-180 tons, with delays of mostly 65 and 100 msec between 30-100 short rows of charges oriented diagonally to the bench, at the Carlin open-pit gold mine. However, in the case of big Kursk mining blasts of 200-1000 tons with delays of mainly 20 and 35 msec between three long rows of charges oriented along the bench, a clear dependence of magnitude on total charge was observed (Leith et al., 1997). Following a simple analysis of superposition and interference of
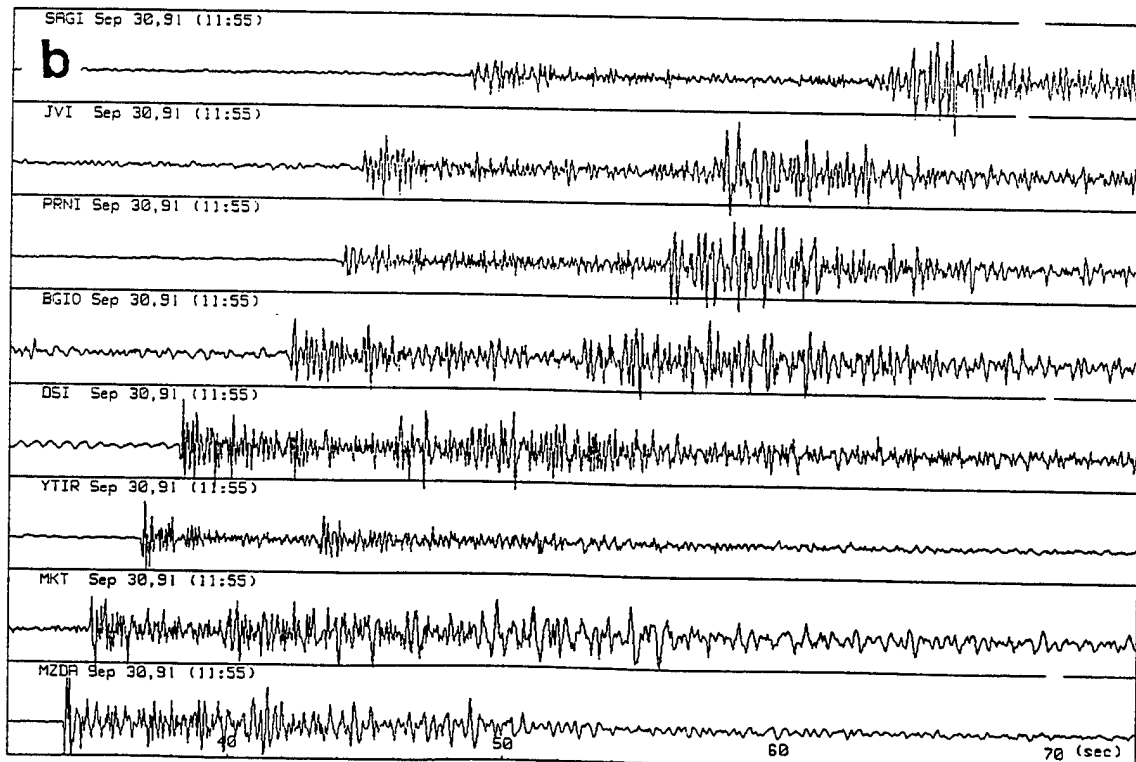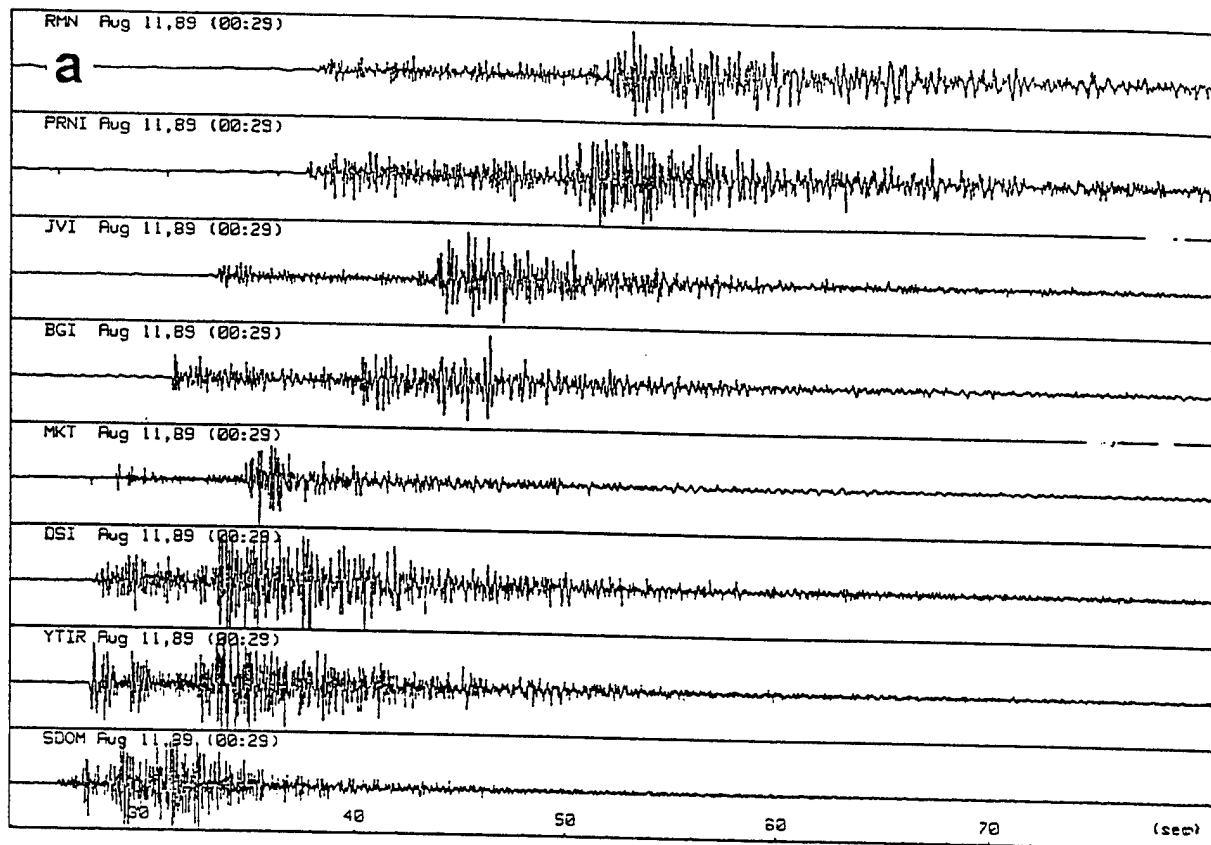
Fig. 6. Examples of Dead Sea earthquakes: (a) "typical" seismograms of QS3; (b) explosion-like wave features for QS12 (the largest amplitudes in the P-group for the five closest stations).

seismic waves for ripple-fired blasts (e.g. Gitterman, 1982), the main factors affecting amplitude of recorded seismic waves (and appropriate magnitude) are the charge weight exploded simultaneously (per delay), delay time and number of delays. This analysis permits an easy explanation of the observed differences for the Carlin and Kursk quarry blasts.

Fig. 7 plots magnitude versus charge weight of 59 ripple-fired quarry blasts in the Galilee, the Negev and in Jordan, showing considerable variance and no correlation for charges of 2-10 tons and a weak dependence for charges of 10-17 tons. The blasting parameters used, i.e. delays of 20-40 msec between 10-40 short, diagonally oriented rows of charges (Gitterman and van Eck, 1993), are close to those at the Carlin mine. In this case the blast size is enlarged due to the increasing number of delayed rows of hole charges, producing a prolongation of radiated energy and duration of signal with no significant rise in recorded amplitudes. It should be noted that local magnitude M_L estimates based on coda duration (Shapira, 1988) are not much affected by this duration increase of 1-1.5 sec. A slight rise in magnitude for larger blasts is due to some increase in exploded charge per delay.

Contrary to these observations, a clear correlation between charge weight and magnitude is observed for 10 simultaneous quarry shots (see Fig. 7) and 9 Dead Sea underwater explosions. Preliminary approximate relationships are estimated (see Fig. 8):

for single quarry blasts: $\qquad M_L = -2.6 + 1.3 * \log_{10} W_{(kg)}$ $\qquad\qquad$ (3.5)

for Dead Sea UWE: $\qquad M_L = -0.01 + 1.2 * \log_{10} W_{(kg)}$ $\qquad\qquad$ (3.6)

Data for 3 Tajikistan UWE (kindly presented by Dr.V.Khalturin) show similar estimates, as Dead Sea explosions. A little bit lower magnitude values are possibly due to weaker coupling (smaller water density and depth), and/or a different magnitude evaluation.

We have also evaluated attenuation of seismic waves as dependence of Peak Ground Velocity (PGV) on the scaled distance $R = r_{(km)} / W_{(kg)}^{1/3}$, measuring maximal amplitude on seismograms, for three UWE in the Dead Sea with charges 304, 192 and 24 kg, and for 10 single blasts (Fig. 9):

for single quarry blasts: $\qquad PGV_{(\mu k/sec)} = 4.65 * R^{-1.3}$ $\qquad\qquad$ (3.7)

for Dead Sea UWE: $\qquad PGV_{(\mu k/sec)} = 67.4 * R^{-1.3}$ $\qquad\qquad$ (3.8)

The high efficiency of the Dead Sea UWE should be emphasized here: very small charges of W=300 kg yield high amplitudes and a local magnitude of M_L=3.1, which is equivalent to an
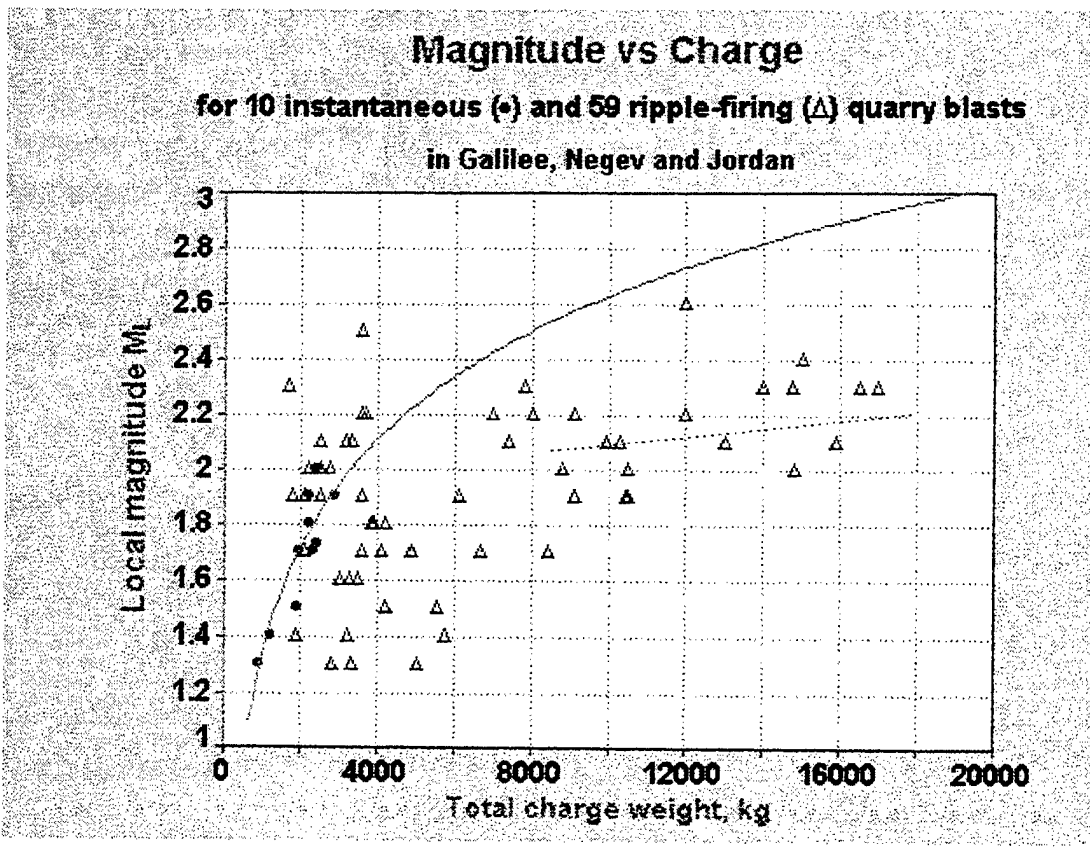
Fig. 7. Seismic efficiency of local ripple-firing blasts, compared with single blasts.
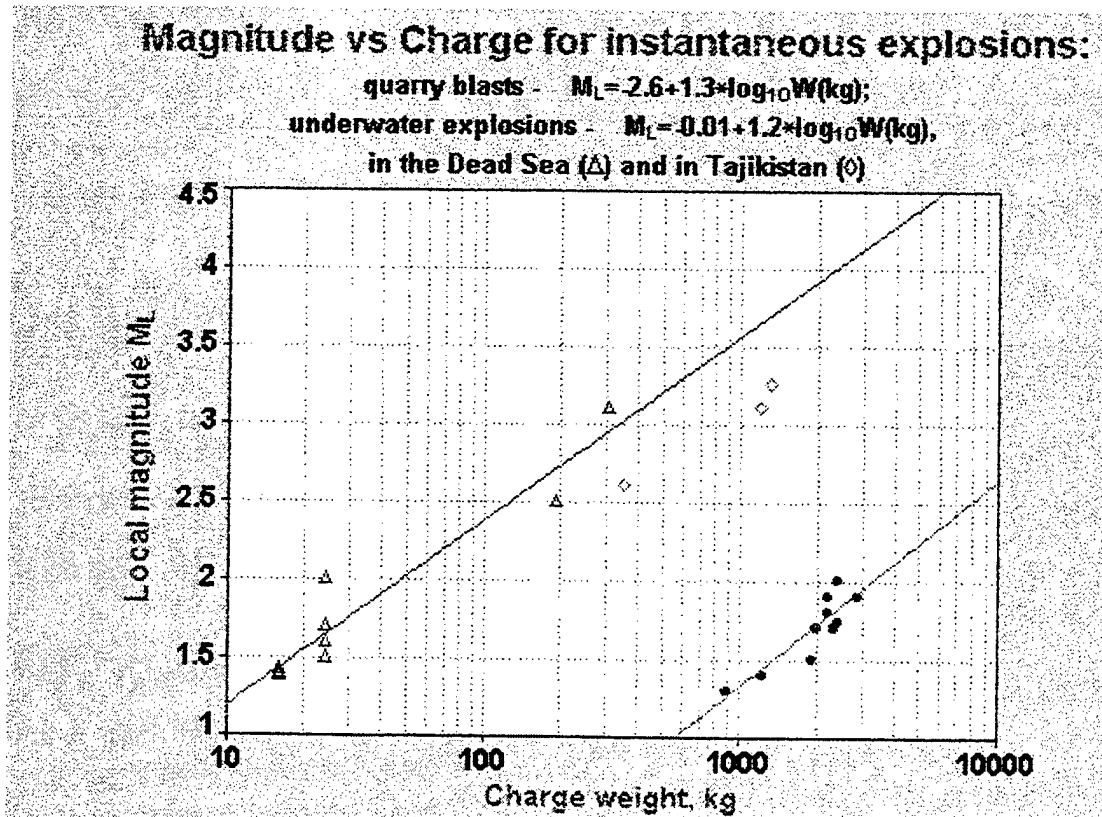
Fig. 8. Seismic efficiency of instantaneous quarry blasts and underwater explosions. Outstanding strong coupling for Dead Sea UWE is observed.

16
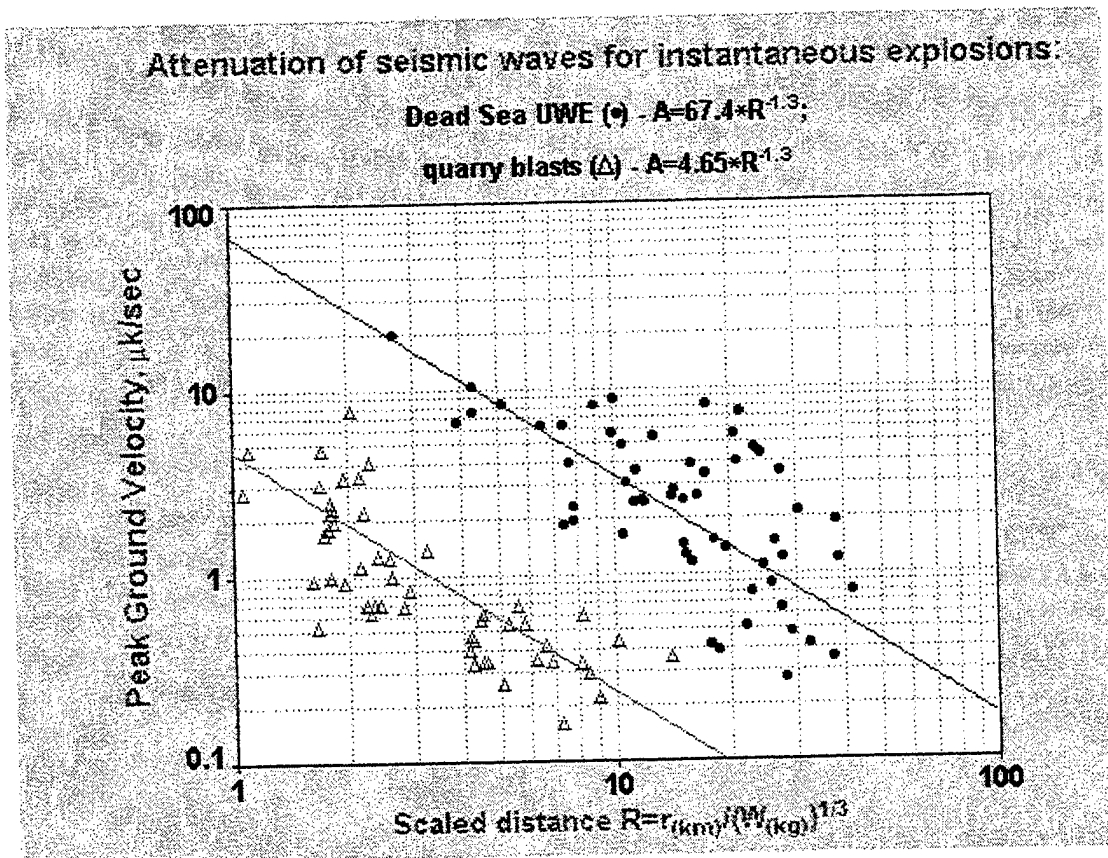
Fig. 9. Empirical attenuation of seismic waves for instantaneous explosions: Peak Ground Velocity versus scaled distance.

instantaneous quarry blast of more than 25,000 kg (Eq.3.5). According Eq. 3.4, a rough estimate of a nuclear yield producing a similar magnitude $m_b=3.1$, equals to 16,000 kg. A strong coupling (and minimal energy losses), caused in particular by the dense salt water and relatively large detonation depth provides effective conditions for calibration explosions currently lacking in the region and necessary for the improvement of monitoring the CTBT.

The equations developed can be used to estimate the efficiency of various calibration explosions (referring to a signal amplitude value of 0.1 μ/sec as the detection threshold). For example, for a simultaneous explosion in a quarry, placed in several dozens of spaced holes, it was estimated (Eq. 3.5,3.7) magnitude and maximal observational distance:

$$W = 20,000 \text{ kg}; \quad M_L \approx 3.0; \quad R_{max} \approx 500 \text{ km},$$

whereas, a smaller explosion in the Dead Sea seems to be much more efficient (Eq. 3.6,3.8):

$$W = 5,000 \text{ kg} : \quad M_L \approx 4.0\text{-}4.2; \quad R_{max} \approx 2600 \text{ km},$$

(R_{max} is the greatest distance at which the event might be observed on the seismograms). Similar UWE in the Dead Sea will probably be recorded by most of the seismic stations and local networks operating in the Eastern Mediterranean and Middle East.

4. DISCRIMINATION METHODS USED IN THE STUDY.

4.1 Known/Modified Discriminants.

4.1.1 *Failed Discriminants: P/S ratio, Coda wave statistics and spectral nulls.*

P/S ratio is the most frequently used discriminant in the family of Pn/Sn, Pn/Lg ratios which is reported to be successful by Pomeroy et al. (1982), Baumgardt and Young (1990) and others. However, these short-period discriminants are heavily dependent upon the structure and constitution of the uppermost crust. Their performance varies from region to region and should be tested on a reliable database with ground truth information in every case study. Most of the investigations mentioned were conducted for a single station or beamed array data. Kim et al. (1994) showed that discrimination based on a single-station discriminant (P/S spectral ratio) enhances significantly when it is averaged over the New York State seismic network. We obtained similar results in this study by averaging amplitude P/S and energy spectral ratios over the ISN.

It is expected that the P/S ratio for explosions will be greater than that for earthquakes. In practice, this appeared to be true for only a limited number of ISN stations at distances greater than 100 km and was realized only for a small part of the data base with strong enough events.

We tested this statistic in the form of ratio of seismogram envelope maximums P_{max}/S_{max} in the P and S (Lg, Rg) velocity domains and showed (Gitterman, et al., 1996) that only 18 events (8 explosions and 10 earthquakes) out of 69 events in the Galilee with $M_L>2$ had SNR large enough at distances greater than 100 km. For these data only six remote sites out of 30 stations of the ISN had P/S values that produced separation between earthquakes and explosions, but at relatively low efficiency. Averaging of the ratio over these six stations enhances the resolving power. No data were available for the remaining 41 events of the data base, hence it would appear to be useless for the most part of our local seismicity.

Coda wave statistics: Following the method of Su et al.(1991), we extracted from the coda wave records (Galilee dataset) spectral amplitude $A_0(f)$ and quality factor $Q(f)$ characterizing the first-order scattering coda wave model of Aki and Chouet (1975). The parameter $A_0(f)$ measures time-independent spectral amplitude of the coda, carrying spectral peculiarities of the source. van Eck (1988) reported that coda spectra of explosions are richer in lower frequency energy as compared to earthquakes. As shown in Gitterman et al. (1996), the ratios $R=A_0(1.5\ Hz)/A_0(10\ Hz)$, averaged over ISN subnetwork recordings of 28 earthquakes and 30 explosions in the Galilee, show much overlapping being only in average higher for explosions than for the earthquakes. The spectral ratio of low-to-high frequency energy measured for the whole signal and averaged over a subset of stations appeared to be much more efficient.

Seismograms of explosions usually have dominant surface waves; these waves propagate at the upper crust layer with high attenuation owing to relatively low Q at low frequencies. However, for the given Galilee dataset this method did not provide separation for the two populations, even for the stronger events. Analysis showed that the method is very sensitive to the SNR and, even for regions where it is applicable, it will be limited to cases of SNR > 10.

Spectral nulls. Contrary to natural earthquakes, underground nuclear tests are characterized by shallow focal depths (several hundreds of meters and by the spherical symmetry of the initial radiation from the source. These features lead to strong destructive interference between the downgoing *P* wave energy and the *pP* wave reflected from the Earth's surface. This interference, however, is complicated by non-linear surface effects on the *pP* reflection (Lay, 1991).

The interference produces modulation minima in the spectra of teleseisms at frequencies:

$$f_m \approx nv/2h \quad (n = 1, 2 ...)$$

(4.1)

where v is the compressional-wave velocity of the medium above the source and h is the depth. For many nuclear tests conducted at depths $h = 500-700$ m and for $v = 1.1-1.5$ km/sec, Eq. 4.1 gives $f_m \approx 1$ Hz. For deeper sources the velocity increases and the frequency value does not change a great deal. Spectra of the initial part (4-7 sec) of the teleseismic records of nuclear explosions detonated at the Nevada test site demonstrated pronounced minima (nulls) near 1 Hz, which could be interpreted in terms of interference of P and pP-wave (Kulhanek, 1971).

Being a source-like effect, the spectral null is apparent at about the same frequency in spectra of different stations of a network and can be used to discriminate nuclear tests from deep earthquakes. This phenomenon was also observed for ISN short-period (Fig. 10) and broad-band (Fig. 11) records of several Chinese tests, with almost identical deep spectral minima, which suggests that the locations and depths of these explosions are very close. (An identity of SP and BB seismograms and spectra should be noted, thus confirming absence of significant distortions in low-frequencies of teleseismic P-waves recorded by short-period instruments).

We tried to check the azimuthal independence inherent to this source-like effect and compare spectra of the P-waves group at different ISN stations. Some explosions (e.g. NT15 on Fig. 12) demonstrate a distinct spectral modulation and high coherency of spectral shapes at many stations, with minima at about 1 Hz (several multiple minima can be observed at 2, 3, 4 and 5 Hz). Nevertheless many explosions revealed strong variability of the null frequency (Fig. 13), which can hardly be identified for some stations. On the other hand, several earthquakes (e.g. QT26) also show the same spectral null phenomenon, possibly caused by interference of rupture sub-events (see Fig. 14). We conclude that this spectral feature cannot be utilized here as a reliable discriminant.

4.1.2 *Successful Discriminants: energy spectral ratio, spectrogram and P/P-coda ratio.*

Energy spectral ratio (SR). ISN seismograms of quarry blasts demonstrate more low-frequency content of seismic waves than local earthquakes (Fig. 15). It has been suggested that spall mechanisms contribute to low frequency seismic energy and the general tendency for quarry blasts to appear deficient in high frequency energy (Barker et al., 1993). We suggest that the phenomenon is mainly due to dominant surface waves (including Rg on the vertical component) generated by quarry blasts and associated with the regional crustal structure of widespread unconsolidated, low velocity and low Q subsurface sediments (e.g. Ginzburg and
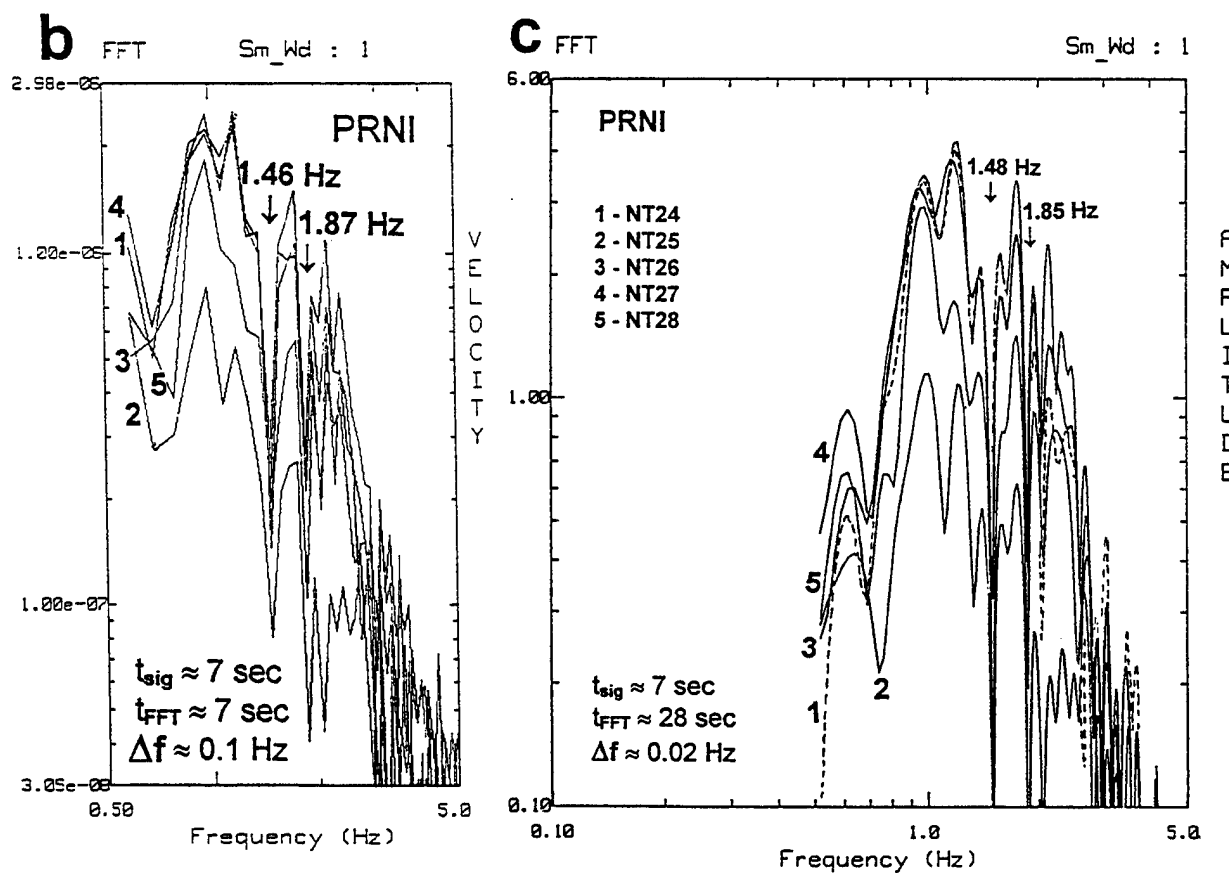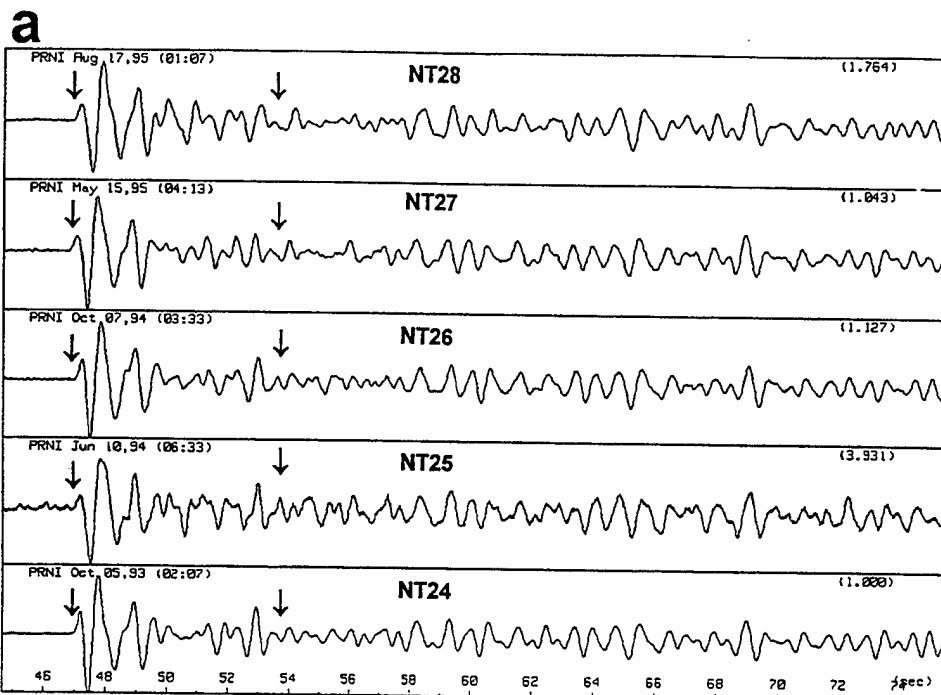
Fig. 10. Several Chinese tests recorded at the ISN station PRNI (a). Instrument-corrected spectra of time windows about 7 sec, marked by arrows, show distinct spectral nulls (b), almost identical for all events. After enhancement of spectra resolution by expanding the analyzed signal by zeros to 28 sec, and reducing Δf from 0.1 Hz to 0.02 Hz, the spectral nulls became deeper and better expressed (c).

21
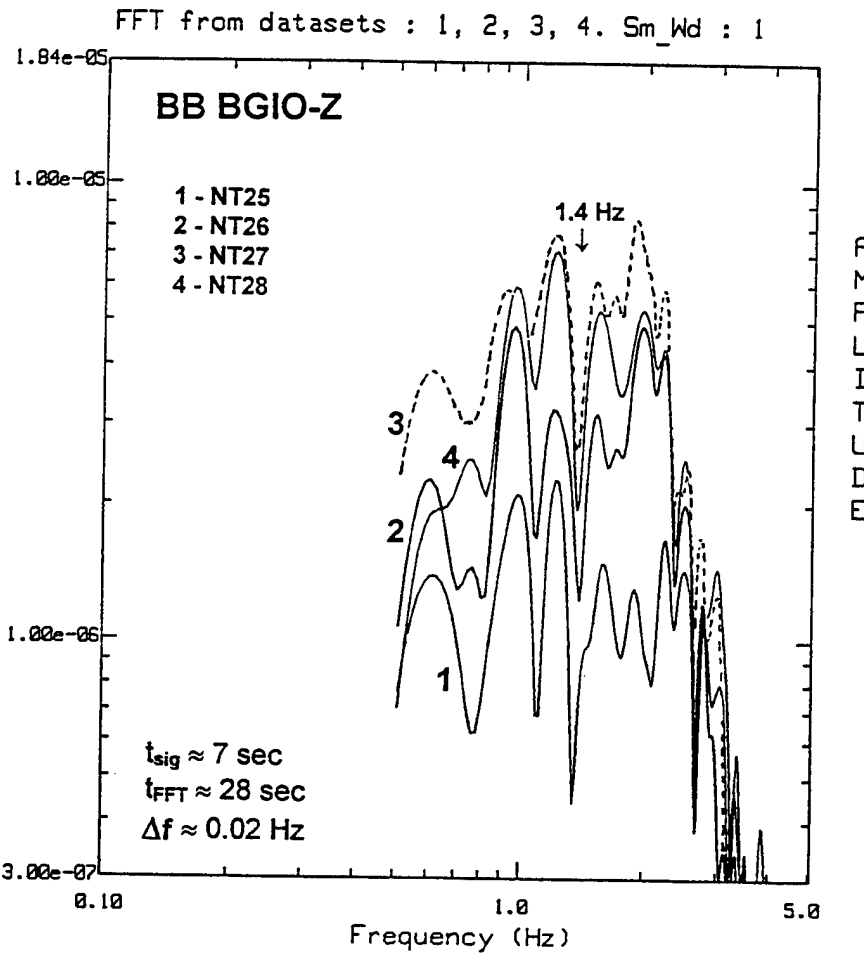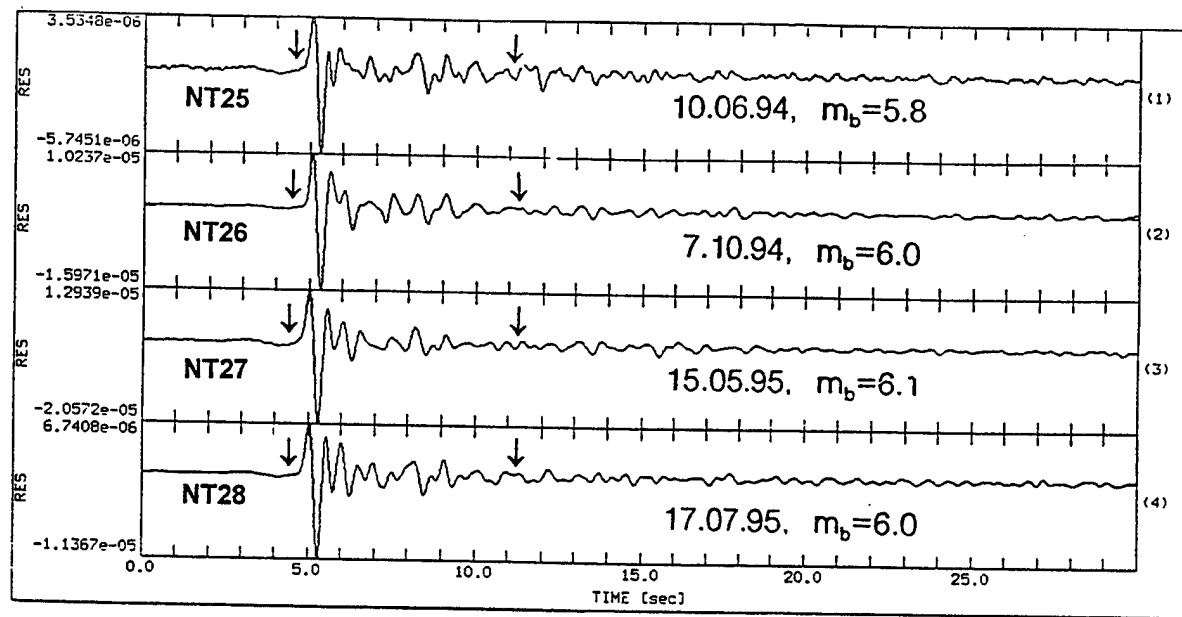
Fig. 11. Records and spectra of the Chinese tests at the BB station BGIO (vertical component) demonstrating similarity to ISN short-period data. The analyzed signal in time windows about 7 sec, marked by arrows, was expanded by zeros to 28 sec, for better spectra resolution.

Nuclear test NT15 88/08/22, W.Siberia, 66°N 78.5°E , m_b=5.3
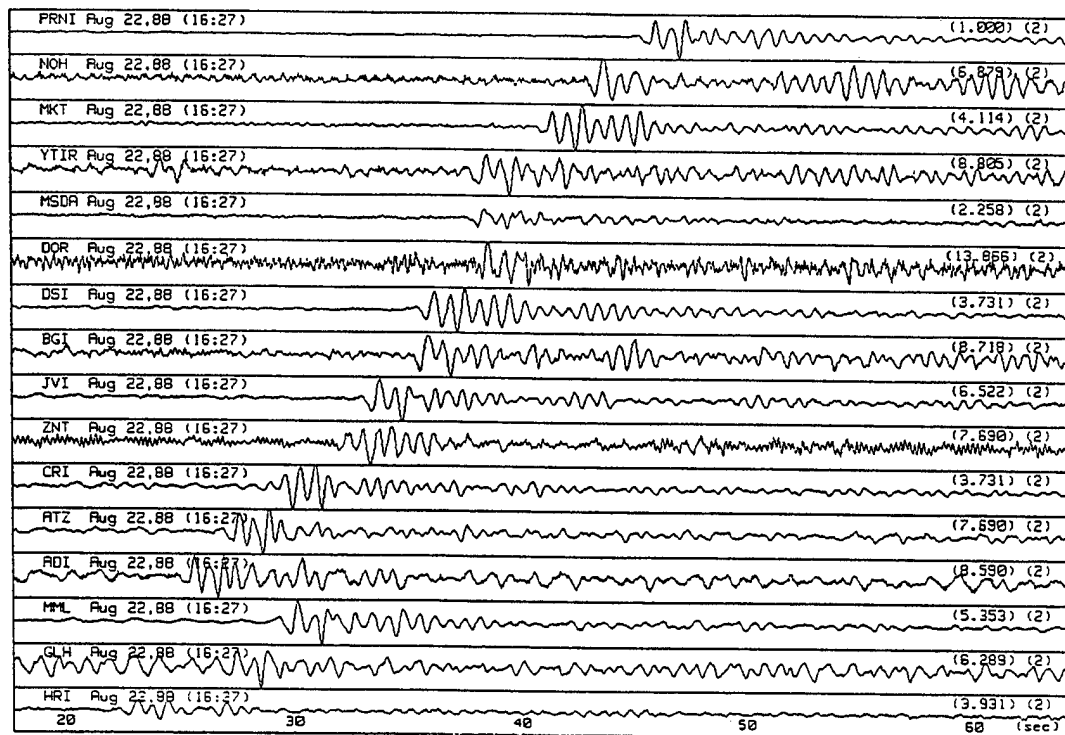
FFT spectra at ISN stations, time window [0-15 sec]
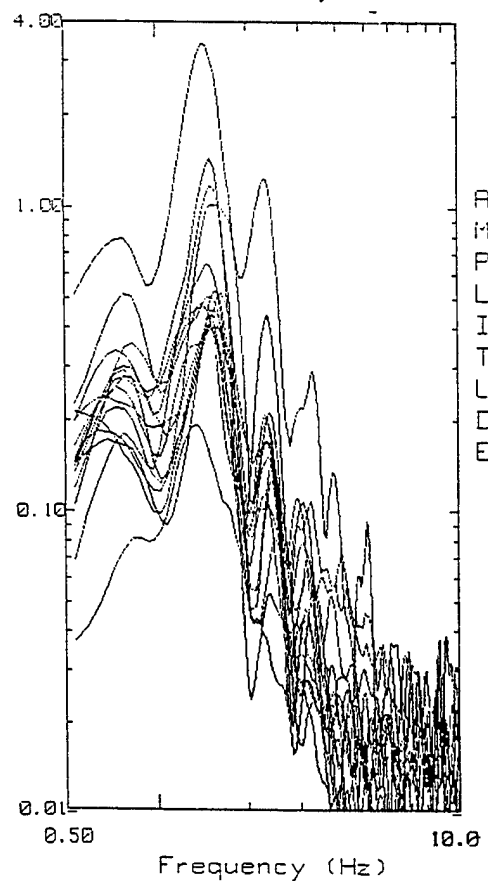
Fig. 12. The nuclear test NT15, demonstrating distinct spectral nulls and modulation and high coherency of spectral shapes at different stations.

Nuclear test NT27 95/05/15, China (Lop Nor), 42°N 89°E, m_b=6.1
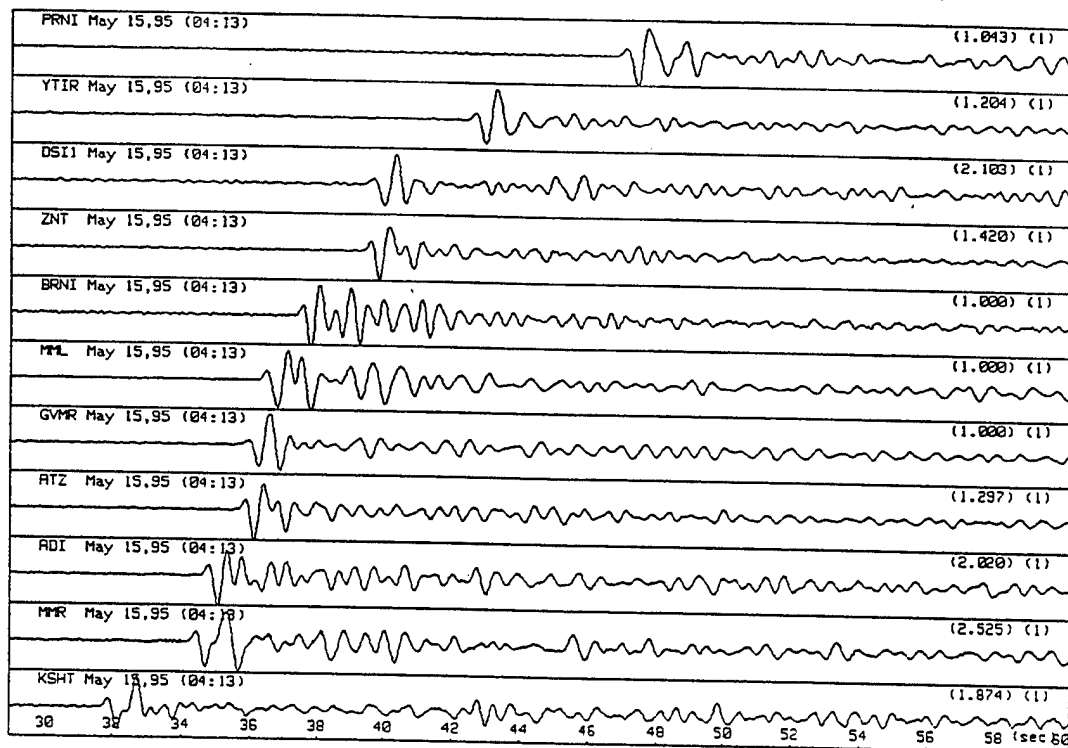
FFT spectra at ISN stations, time window [0-15 sec]
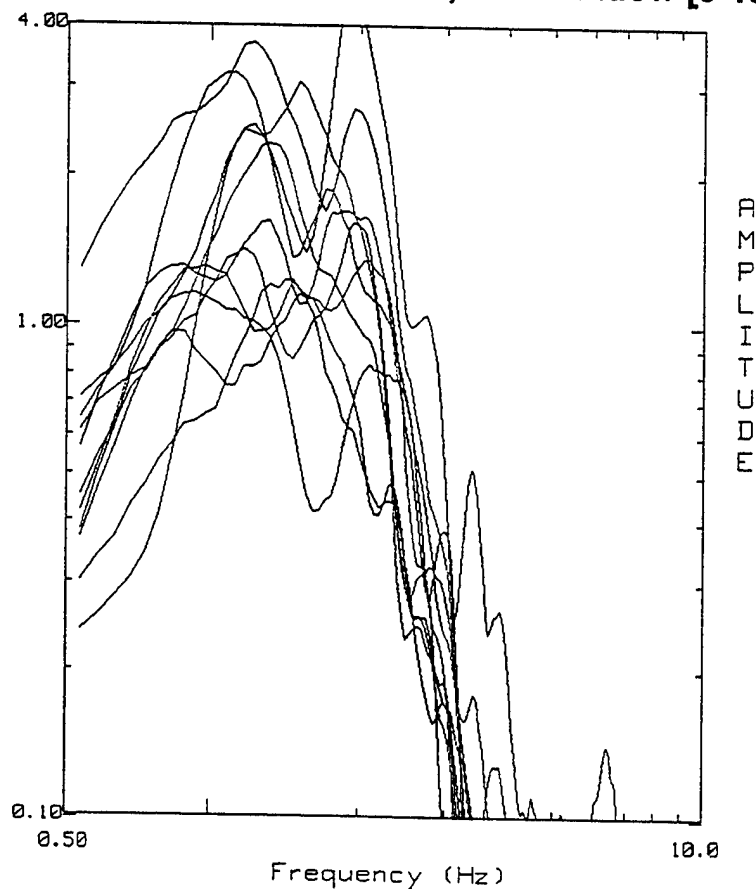
Fig. 13. The nuclear explosion NT27 showing strong variability of the null frequency and spectral shapes.

24

Earthquake QT.26 91/08/19, China, 47°N 85°E, H=44 km, m$_b$=5.7
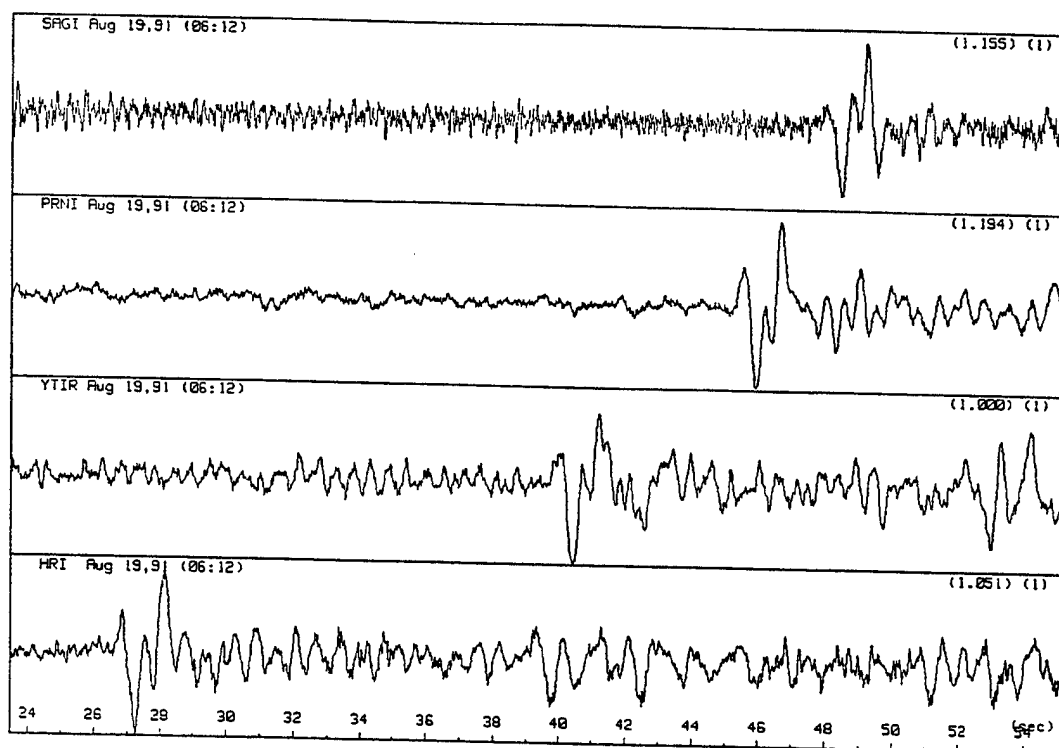
FFT spectra at ISN stations, time window [0-15 sec]
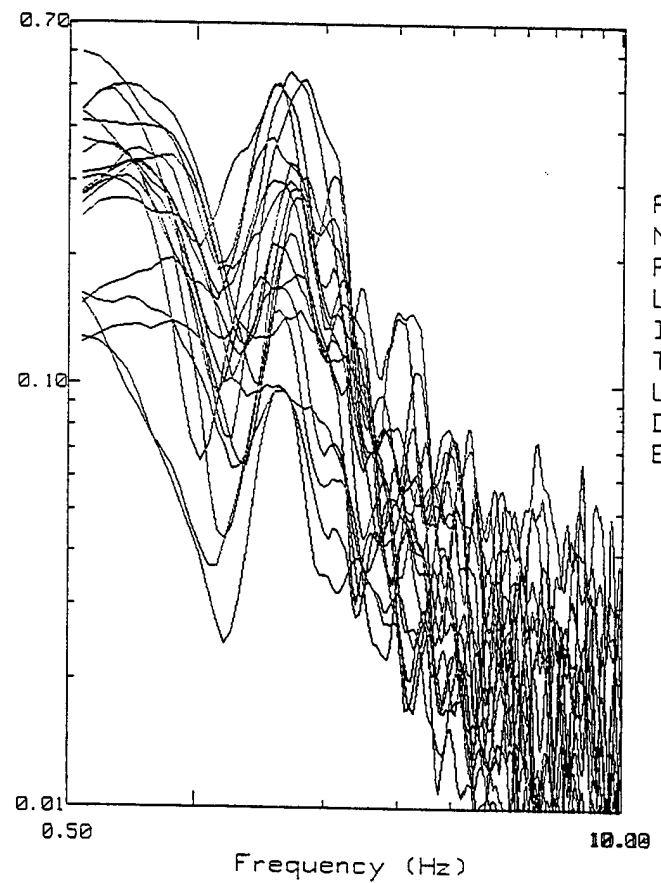
Fig. 14. The earthquake QT.26, revealing explosion-like nulls about 1 Hz, modulation and high coherency in spectra for 19 stations. Seismograms of four stations only are presented for better observation of characteristic interference features in the P-wave.
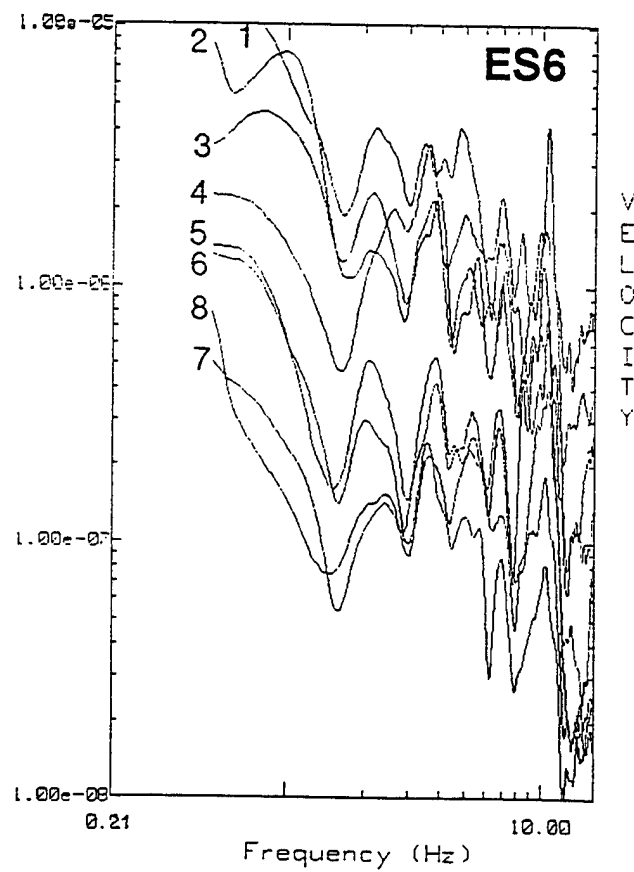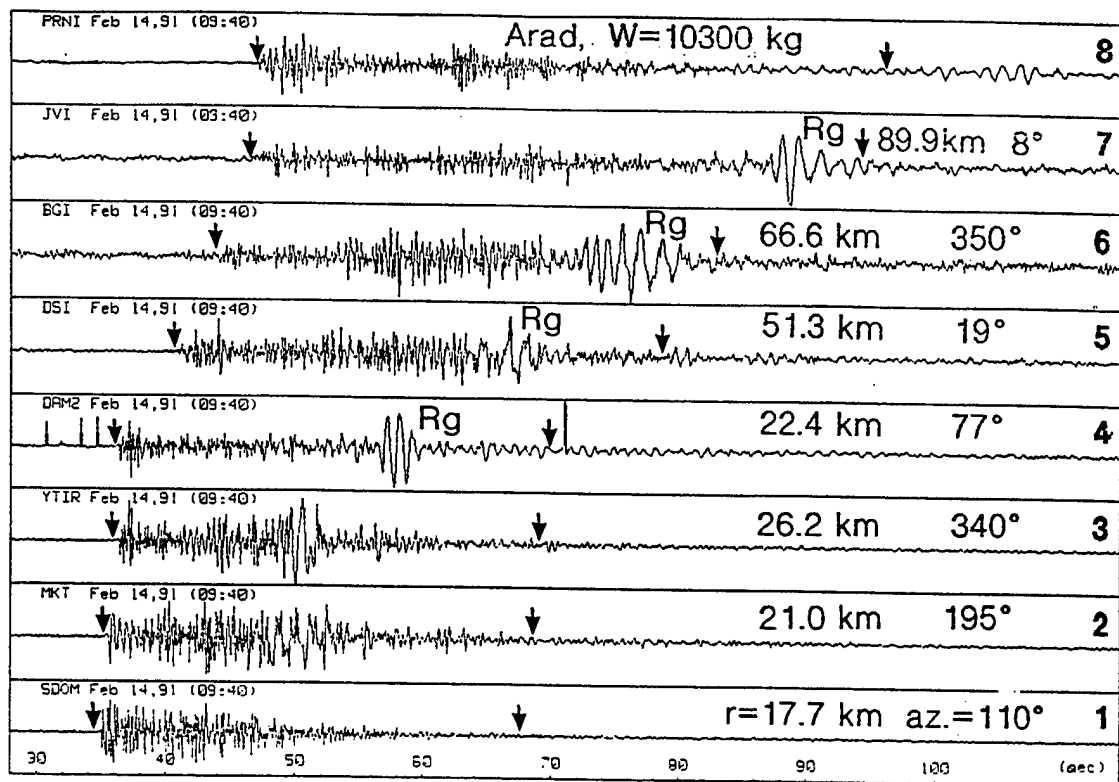
Fig. 15. Examples of recordings at different ISN stations and appropriate spectra: (a) a ripple-fired blast (ES6) from a Negev quarry, showing distinct azimuth and distance-independent spectral modulation, and low-frequency spectral content due to strong surface (Rg) waves.

26
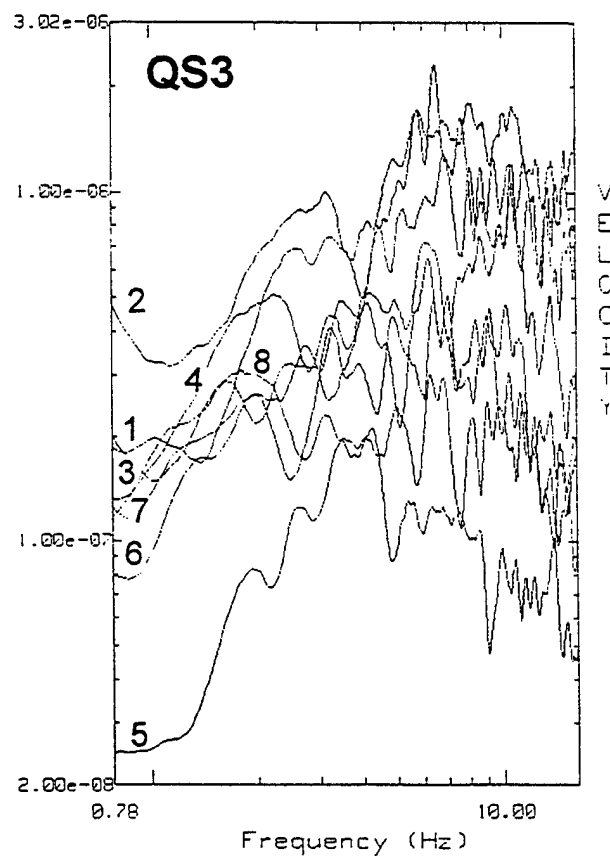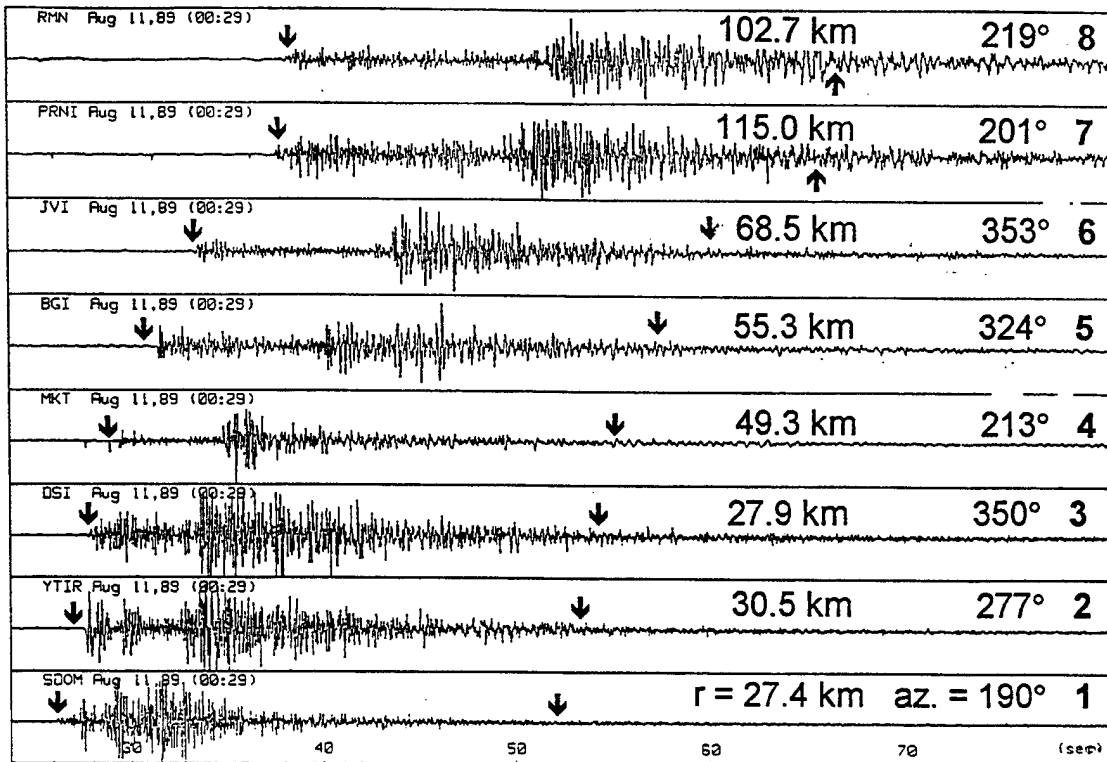
Fig 15b. An earthquake from the Dead Sea (QS3), demonstrating non-coherency of spectral shapes and high-frequency energy. Arrows show analyzed time windows.

Folkman, 1980), trapping low frequency energy and absorbing high frequencies along propagation paths. This explanation is supported by similar observations from New England (Li et al., 1996) and by the reverse situation for quarry blasts in the Scandinavian shield (Baumgardt and Young, 1990).

We utilized this effect in the energy spectral ratio R_E of seismic energy in the low-frequency range $[f_1, f_2]$ and the high-frequency range $[f_3, f_4]$ (Gitterman and Shapira, 1993):

$$R_E = \int_{f_1}^{f_2} |S(f)|^2 df \Big/ \int_{f_3}^{f_4} |S(f)|^2 df \qquad (4.2)$$

where $|S(f)|$ is the smoothed spectrum of ground velocity for the whole signal. This ratio, implying evident physical meaning, is similar to the ratios of average spectral amplitude (Bennett and Murphy, 1986, Walter et al., 1995), or power spectrum (Pulli, 1995), calculated for specific regional phases. For an event, R_E values at different stations show strong scattering; averaging over a subnet is crucial for separation between earthquakes and explosions (Shapira et al., 1996).

Spectrogram is a robust characterization of the seismic energy distribution across the specified frequency interval, often useful in the multivariate discrimination analysis (Dowla, 1995, Pulli, 1995). It is a vector statistic resulting from calculation of RMS of FFT amplitudes in the series of spectral windows. For the local data analysis spectrograms were calculated at the large enough time intervals comprising together all seismic phases: P, S, Lg, Rg and a part of coda. For teleseismic discrimination only, P and P-coda time intervals were considered.

P/P-coda ratio teleseismic discriminant resembles classic complexity statistics (Dahlman and Israelson, 1977) and was shown to be efficient for the NORESS teleseismic recordings (Tsvang et al., 1993).

P/P-coda ratio results from the following computations:
- *Spectra* are computed for the forward short time interval (2 seconds) and the following long time interval (30 seconds).
- *A spectrogram* is computed for each of the time intervals in several (six) equal frequency bands in specified spectral interval (from 0 to 5 Hz).
- The maximum coefficient is taken in each of the two *spectrograms* and averaged over a set of the network stations. The resulting statistics are used to calculate the *P/P-coda ratio* discriminant.

4.2 Newly Developed Procedures.

4.2.1 *Spectral Semblance (SS).* Distinctive features of the quarry blasts and underwater explosions records are clear spectral modulation patterns presented by coherent minima (or nulls) and maxima observed at low frequencies 1-10 Hz (Fig. 15a). This azimuth-independent modulation is caused by constructive-destructive interference of linearly superimposed waveforms from spaced charges exploded at millisecond delays ("ripple-firing") (e.g. Gitterman, 1982; Stump and Reinke, 1988), or from oscillations of gaseous bubbles in water and indicative of the source-effect. Another approach to reveal spectral modulation involves the time-independent pattern in a sonogram at a single station (e.g. Hedlin et al., 1989), but this kind of modulation can appear also due to a propagation path effect.

In contrast to a ripple-fired blast, the spectral pattern for an earthquake is strongly azimuth-dependent, owing partly to the directivity effect (e.g. Bakun et al., 1978), therefore, for stations with broad azimuthal coverage, we observe an irregular character of spectral shapes and minima for different azimuths (Fig. 15b).

The *semblance* and *cross-correlation* statistics are commonly used in seismic prospecting for phase correlation of seismic traces in the time domain (Neidell and Taner, 1971). We modified these statistics to assess quantitatively the coherency of spectral shapes for different stations. As expected, a clear equivalence between the two characteristics was observed (Gitterman et al., 1996), therefore, in the following we considered only *spectral semblance* (SS), i.e.:

$$S_f = \frac{1}{N} \sum_{F_1}^{F_2} \left[\sum_{k=1}^{N} (S_{ki} - \overline{S}_k) \right]^2 \bigg/ \sum_{F_1}^{F_2} \sum_{k=1}^{N} (S_{ki} - \overline{S}_k)^2 \tag{8}$$

where $S_{ki} = \log_{10} S_k(f_i)$ - log spectral amplitude at k station; $\overline{S}_k$ is the average spectral level; N is the number of used stations and $[F_1, F_2]$ is the frequency band for the analysis.

4.2.2 *Velogram Analysis Statistics.* Another new RDSN oriented discriminant is based on velograms - signal envelopes versus group velocity. The signal envelopes are calculated using RMS in the moving window, and group velocities are the ratios of R/T, where R is the distance and T is the lapse time. The analysis is based on computation of the group velocity V_{ms} value corresponding to the local maximum of the velogram in the range of 1-4 km/sec (see Fig. 16).

The relationship between the S-waves group velocity V_{ms} and the distance R (in the range 10-150 km) differs for blasts and earthquakes (Fig. 17). The effect should probably be attributed to the different excitation of surface waves from these two types of seismic events or/and different S-waves group velocities for shallow and deep sources emphasized in many studies (Kafka, 1990; Walter et al., 1996; Alexander et al., 1995). It was shown (Pinsky and Shapira, 1997), that a simple "C" statistic, derived from the parametric approximation

$$V_{ms}(R) = a + b*\ln(R) \qquad\qquad (4.4)$$

$$C = b + 0.33*a, \qquad\qquad (4.5)$$

provides the true identification of the events from the Galilee data base recorded by the ISN stations.

4.3   Multivariate Procedures of Pattern Recognition

An additional effect is achieved using an Integrative Approach (IA) using a number of different physically signal features. Wuster (1993) showed that even the simple *majority voting* of several different physical discriminants with equal weights provides improvement of classification result.

4.3.1 Linear Discrimination Function (LDF) - commonly used in discrimination seismology statistical procedure which accounts for different weights of discriminants and their mutual correlation. It is based on the assumption that the vectors X of observed parameters generated by two stochastic (physical) mechanisms H_1, H_2 (earthquakes and explosions), are described by Gaussian distribution with equal covariance matrices $S = S_1 = S_2$ and different mathematical expectations M_i. The optimal decision rule, based on log-likelihood ratio function V(X), is (Tsvang et al., 1993):

$$\{\text{assign X to } H_1, \text{ if } V(X) > 0 \text{ and assign X to } H_2, \text{ if } V(X) < 0\} \qquad (4.6)$$

where $V(X) = F_1(X) - F_2(X) = 2(M_2 - M_1)^T S^{-1} X - M_1^T S^{-1} M_1 + M_2^T S^{-1} M_2$ is a linear function of vector X.

Practically, instead of covariance matrix S_i and expectation M_i corresponding statistics are substituted based on appropriate data samples. The assumption that $S_1 = S_2$, yielding separation of the two data sets by the hyperplane V(x)=0, is rarely realized and the general
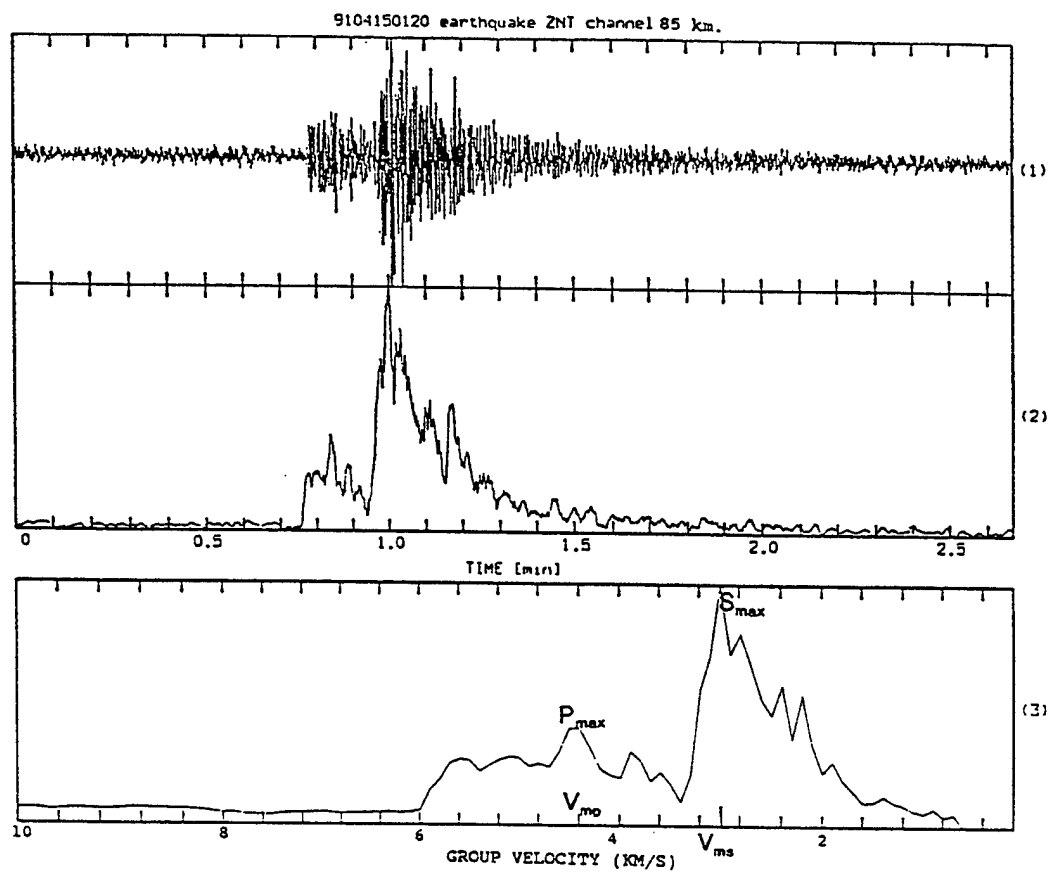
Fig. 16. Velogram analysis: example of data processing of an earthquake at station ZNT.
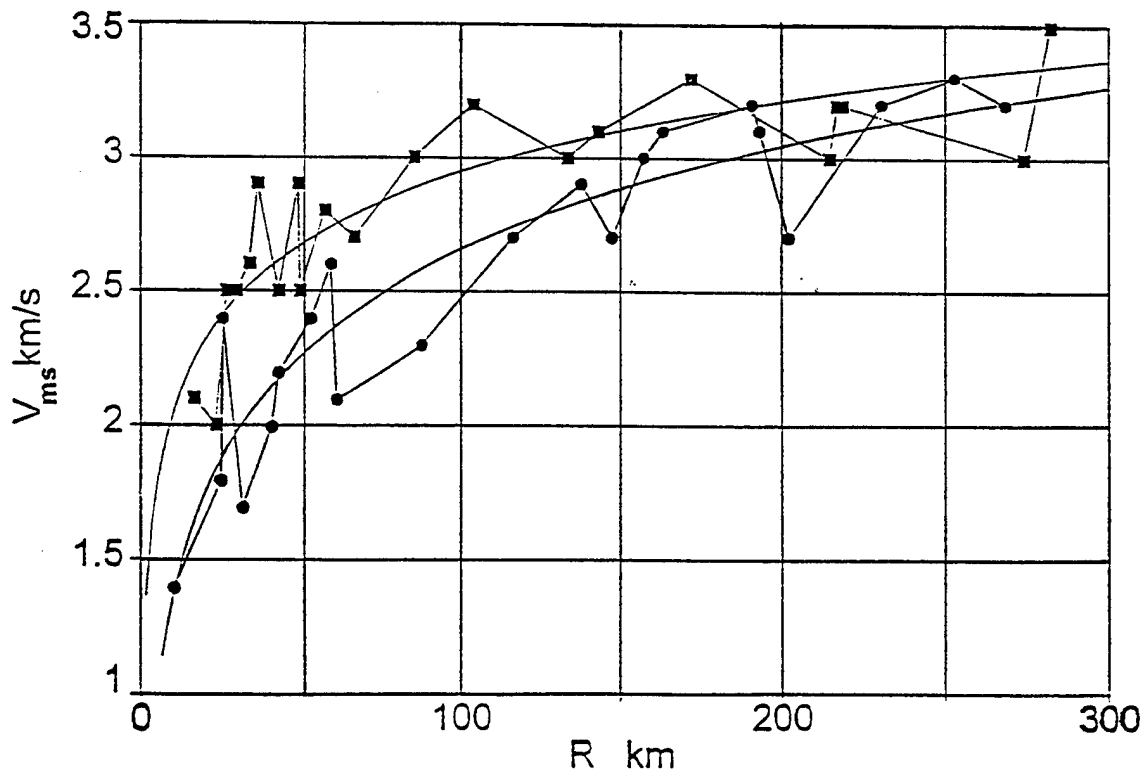
Fig. 17. Velogram analysis: V_{ms}-distance curves for an earthquake and an explosion.

expression for the likelihood function should be used for optimal decisions. However, in practice even in this case, the algorithm usually works fine if sample covariances S_1 and S_2 are substituted by their average value.

4.3.2 *Artificial Neural Network (ANN)* should have an advantage over the LDF in the case where the separating surface between the data sets is essentially nonlinear.

We have used the ANN program, which was kindly provided by Dr. F. Dowla (LLNL, USA). This network is a classical example (Dowla, 1995) of a supervised learning network applying backpropagation learning algorithm to associate inputs with corresponding outputs for all or most of the events in a training set. This algorithm uses a gradient descent method to systematically modify the weights in the network so as to minimize the network output error.

5. ANALYSIS OF DISCRIMINANT PERFORMANCE

5.1 Application of Energy Spectral Ratio and Spectral Semblance to Regional and Teleseismic ISN and NORESS Recordings.

Regional data. Initially, using data from the Galilee region, we tried for spectra radio $f_1=1$ Hz, $f_2=f_3=6$ Hz, $f_4=11$ Hz and $F_1=1$ Hz, $F_2=12$ Hz for spectral semblance (Gitterman et al., 1996), thus facilitating almost the whole recording frequency band. Application of another ratio (2-4 Hz)/(6-8 Hz), used by Li et al. (1996) for the Lg spectra to separate small events in New England, reduced the resolving power (Fig. 18a). However, after a low frequency shift, the (1-3 Hz)/(6-8 Hz) ratio enhanced separation between quarry blasts and earthquakes and provided the best discriminant performance (Fig. 18b). It is interesting to note that almost the same frequency bands (1-2 Hz)/(6-8 Hz), but calculated for separate seismic phases, were used for discrimination of NTS explosions and earthquakes at short distances, and performed well over magnitude 3.5 (Walter et al., 1995).

As expected, the semblance values are much higher for quarry blasts than for earthquakes and remain practically unchanged when using other (different from usual 0.5 Hz) windows of spectra smoothing (0.25 and 1 Hz).

For the few earthquakes originating on the main fault in the Sea of Galilee, we obtained anomalous high SR and SS values. A different range (1-7 Hz) provided "normal" semblance values for these earthquakes, but for the rest of events we obtained a worse separation. The best semblance performance for the Galilee and Gilad regions was obtained for the (1-8 Hz) band (Fig. 18c), nevertheless, due to worse results for quarry blasts and earthquakes from the southern Dead Sea/Negev area and single blasts (Fig. 18d), the optimal range remained valid as 1-12 Hz. In general, all earthquakes show consistent ratio and semblance values, lower than those for ripple-fired quarry blasts with the thresholds: $R_E = 6.1$, $S_f = 0.69$.

The discrimination results for all local events are presented in Fig. 19. Anomalous low ratio values for Dead Sea UWE are possibly associated with the higher frequency content of radiated seismic waves due to deeper source (70m) than that of the off-shore UWE near Tyre (assumed 10-30m), higher density of water and small charges (mostly 16 and 24 kg). According to Eq. 3.1, for the charge weight W=24 kg, the predicted dominant frequency due to the bubble-effect is $f_{1b} \approx 6.7$ Hz and is close to the observed value of 6.0-6.5 Hz (see Fig. 20). This observation could also be influenced by the f_d harmonic (6.3 Hz from Eq. 3) related to the detonation depth. It turned out that for small explosions the reverberation effect caused by the

a
Galilee dataset

b
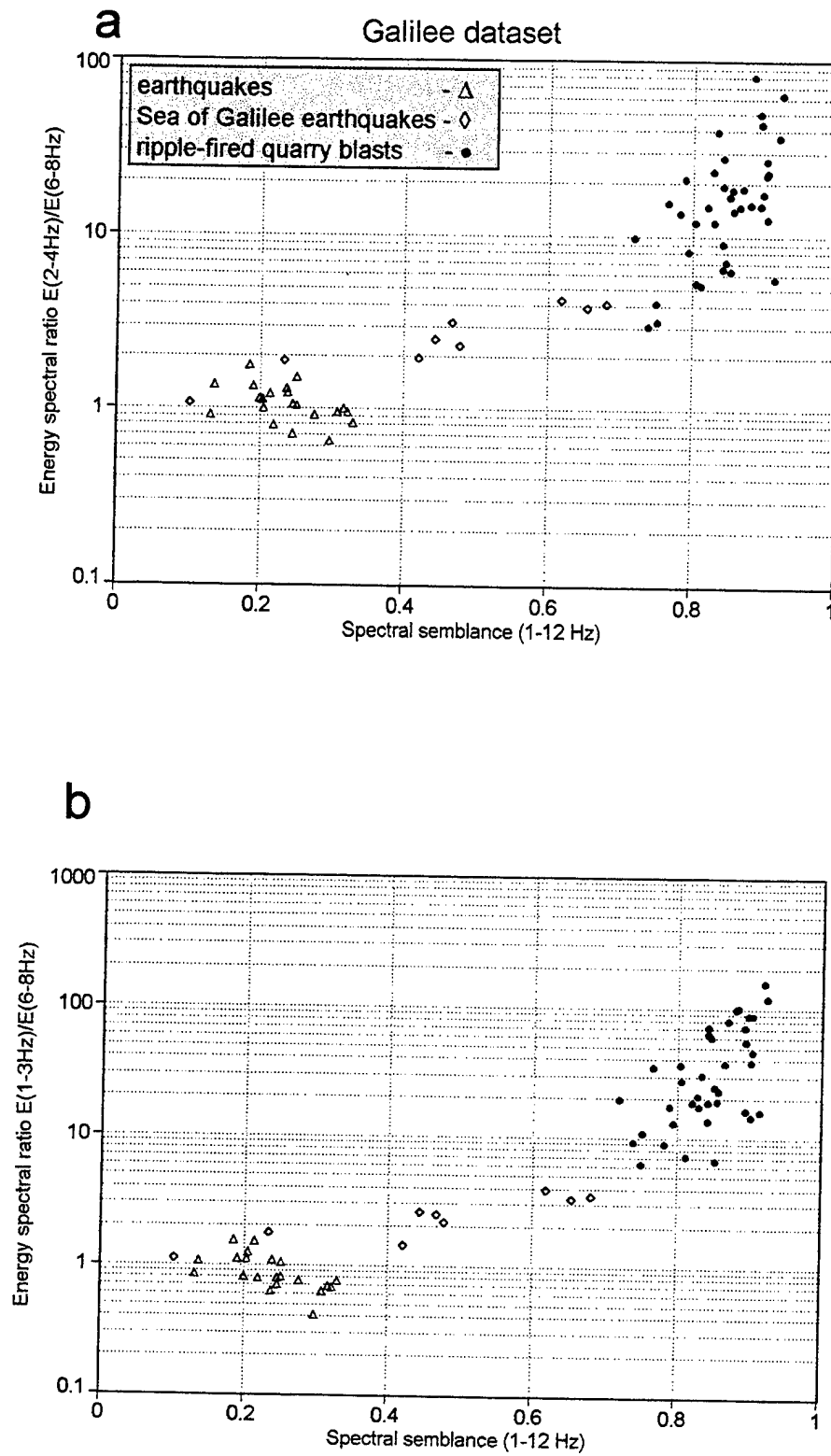
Fig. 18. Discrimination results (spectral semblance vs spectral ratio) for local events at different frequency ranges. Separation of earthquakes and quarry blasts in Galilee was improved after a shift of low-frequency band in the energy ratio from (2-4Hz) (a) to (1-3Hz) (b); the semblance range (1-8Hz) provided the best separation of the events from Galilee and Gilad regions (c), but showed a reduced resolving power for the Southern dataset and single quarry blasts (d).

c

Galilee&Gilad dataset

d

Southern Dead Sea/Negev dataset, Jordanian and single quarry blasts

Fig. 18 c,d.

35
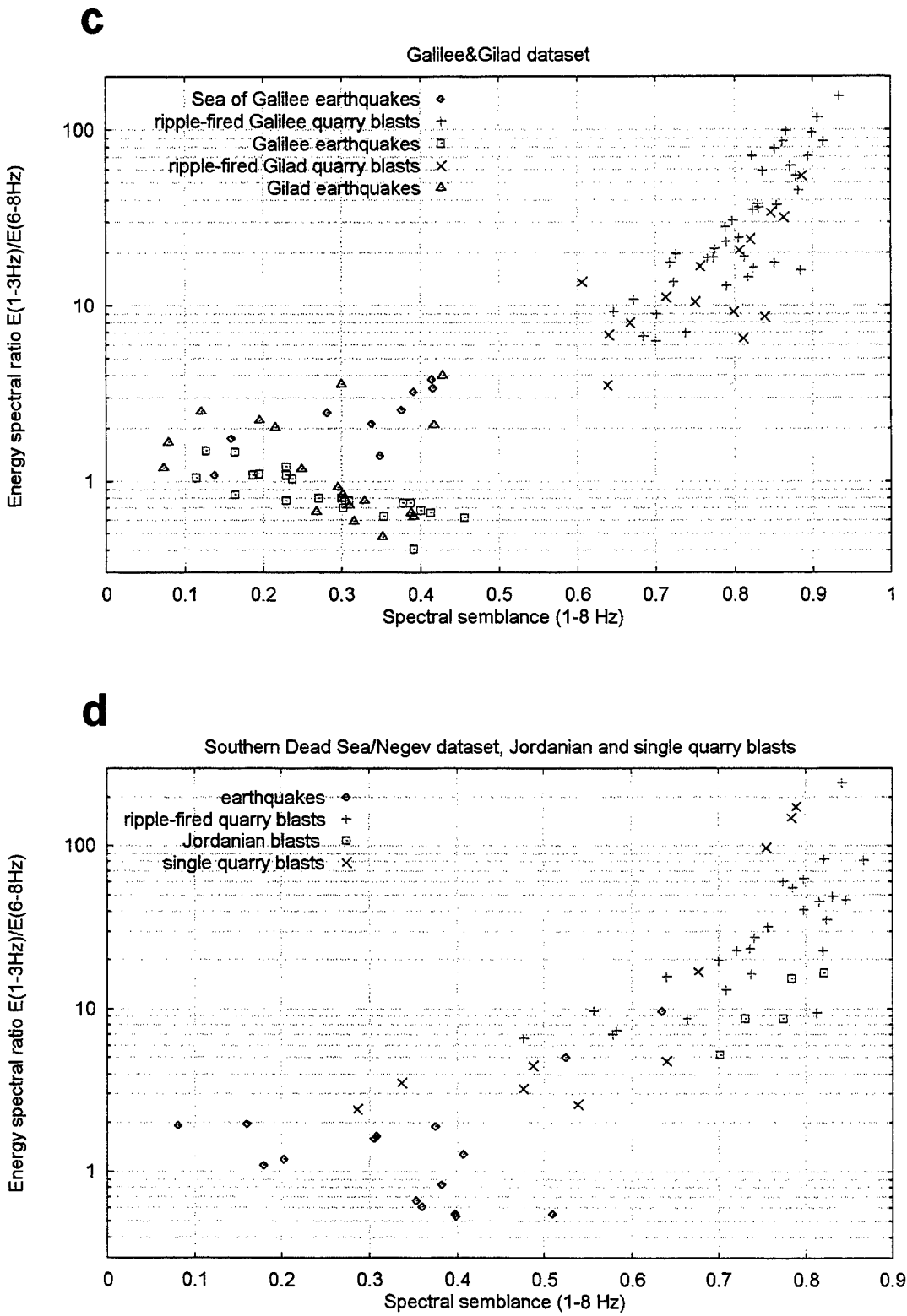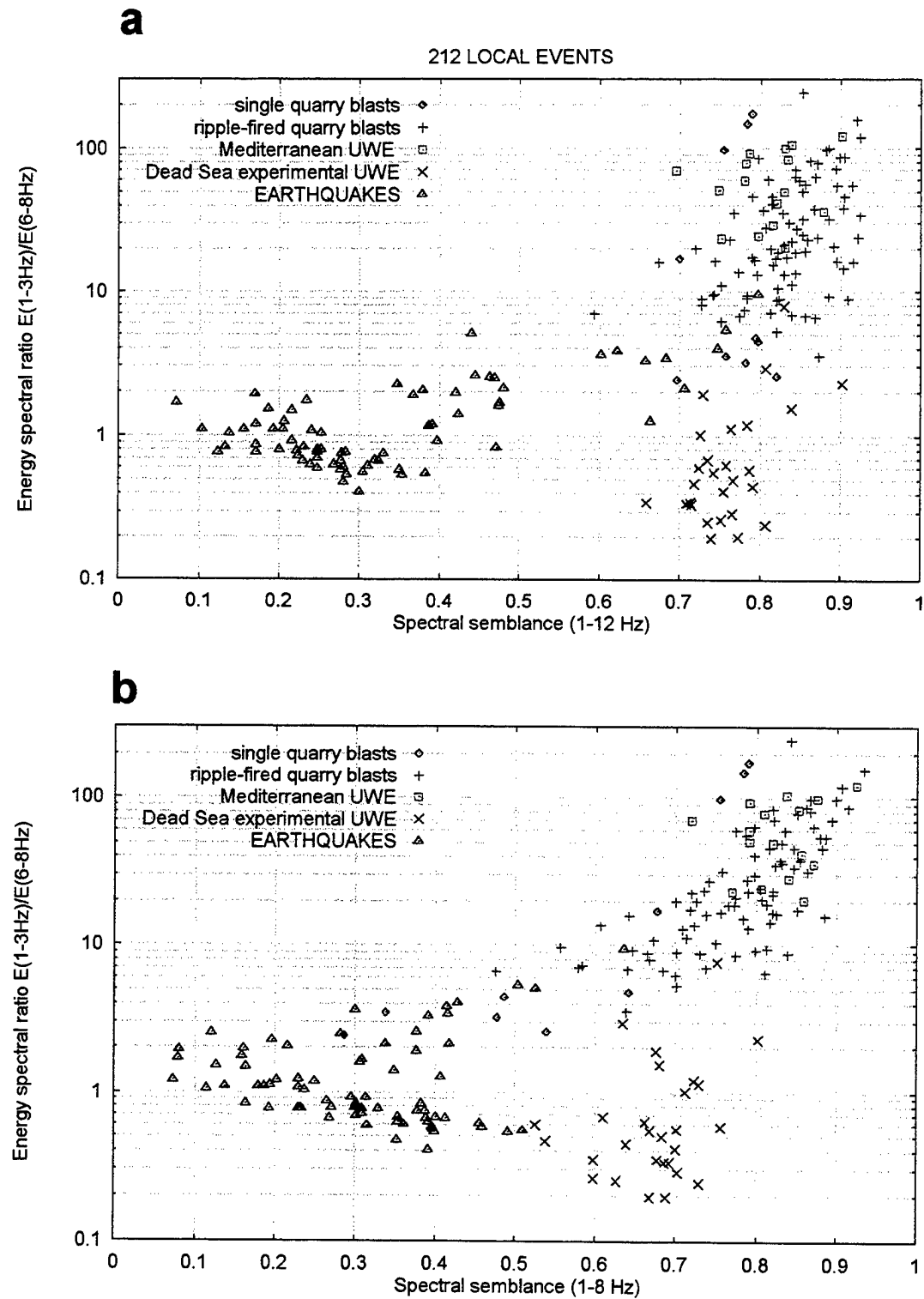
Fig. 19. Discrimination results (spectral semblance vs spectral ratio) for all local events at the optimal frequency ranges (a). The semblance frequency range (1-8 Hz) produces worser separation and stronger overlapping of earthquakes and explosions (b).

36
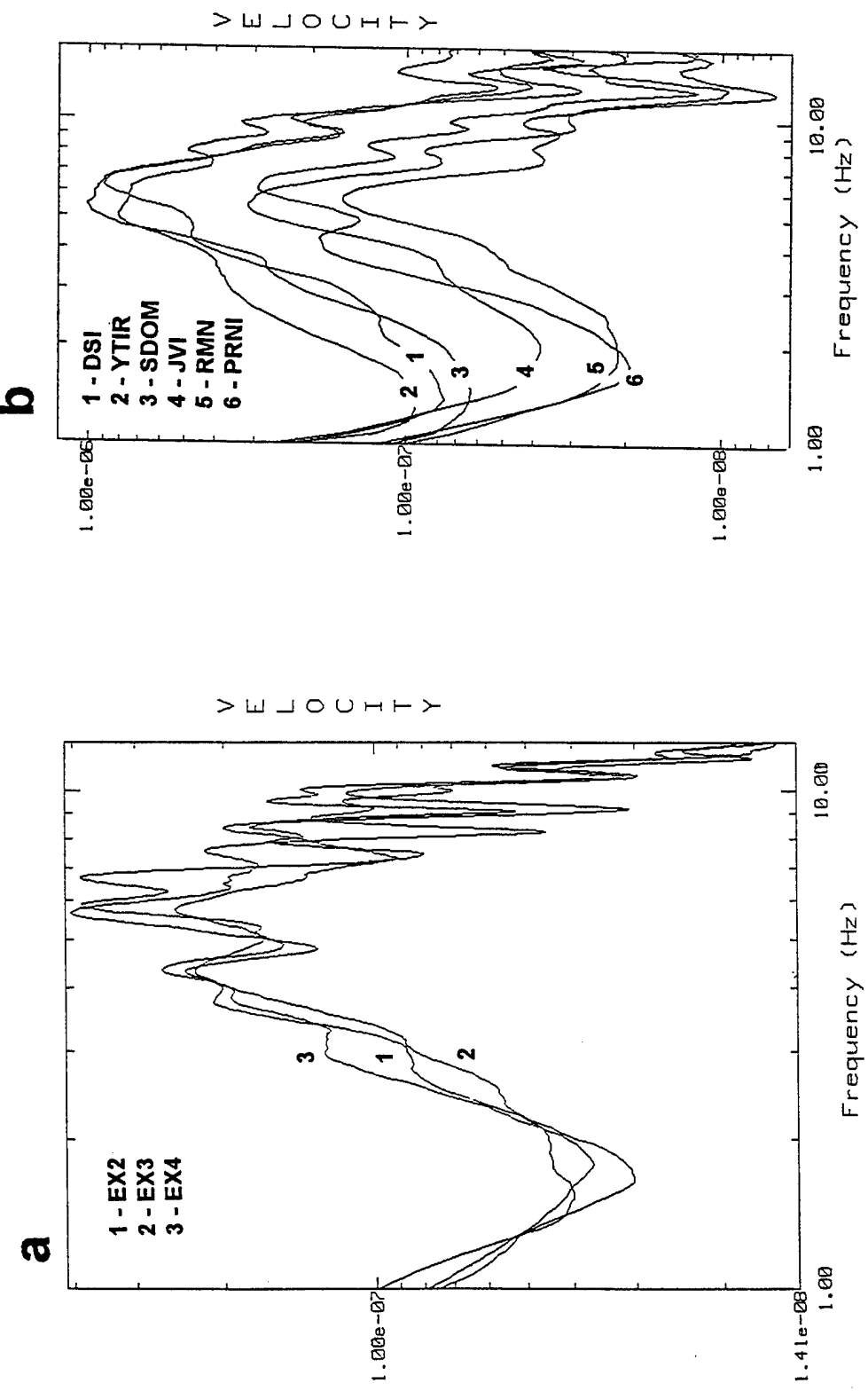
Fig. 20. Spectra of Dead Sea small underwater explosions (W = 24 kg): (a) for 3 events at station PRNI; (b) at different stations for a fixed event (EX2). Observed spectra similarity confirms high stability of blasting parameters for different explosions.

37

water depth H (and the appropriate frequency f_H) was not revealed and, therefore, did not contribute to the low-frequency energy in the band 1-3 Hz (unlike the largest EX1, see Fig. 5). We also suggest that compressional waves from small explosions are scattered stronger (and lose energy) during reverberational multiple reflections from the uneven bottom, due to smaller wave lengths ($\lambda=V_0/f_b=1770/6.7=260$ m), as compared to the explosion EX1 ($\lambda=610$ m).

The spectral ratios for seven instantaneous (single) blasts in the Mt. Nitzim quarry are low ($R_E=2-5$), unlike those for three single shot blasts at the Revaya quarry ($R_E>100$), demonstrating strong low-frequency seismic radiation (Fig. 21). This is possibly associated with the uppermost geology near the two quarries located in different regions (see map in Fig. 1). The Revaya quarry is located in the Beit-Shean sedimentary basin formed by soft river and lake deposits, and the propagation paths to the stations cross the basin, producing the low frequency surface waves due to channeling and the intrinsic absorption of high frequency energy. In contrast, the Mt. Nitzim site, containing consolidated massive carbonates, is more correspondent to the hardrock conditions producing high frequency seismic radiation (Fig.22).

The semblance values for single explosions are lower than those for ripple-fired blasts, but higher than for earthquakes (see Fig. 19). A possible explanation for this relates to the fact that single shots do not possess the azimuth-independent modulation in spectra caused by time delays and producing high semblance values. Nevertheless, they are, actually, point sources, and dependence of radiated waves on azimuth is less significant, than for earthquake line sources subjected to the directivity effect. Spectra at ISN stations from single explosions show some coherent gross-structure (envelope of random small scallops): a broad maximum at low frequencies (1-5 Hz), mainly due to surface waves, and steep descend at high frequencies (5-12 Hz), caused by intrinsic attenuation (see Fig. 21,22). This gross-structure provides a significant contribution to higher (than for earthquakes) semblance values. This effect is inherent also in spectra of ripple-fired blasts.

Teleseismic data: The same SR and SS procedures were applied to 68 Eurasian teleseismic events, with the only evident correction (compared with local events) being the shift of spectral bands to lower frequencies.

The analyzed waves (*P* and *P*-coda) from teleseismic earthquakes have more low-frequency energy and more coherent spectral shapes than nuclear explosions (see Figs. 12-14). Therefore, the semblance and spectral ratio values of ISN records of the earthquakes are higher than those for the explosions (see Fig. 23), which is opposite to observations for local events (see Figs. 18 and 19). There is a number of short-period observations of Soviet and
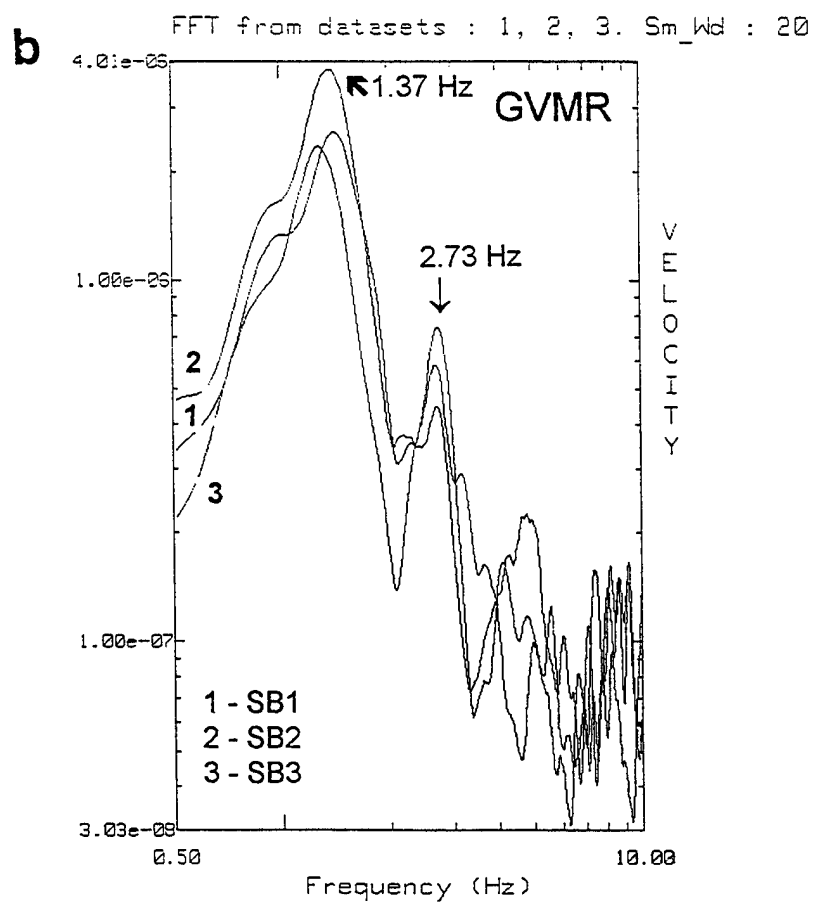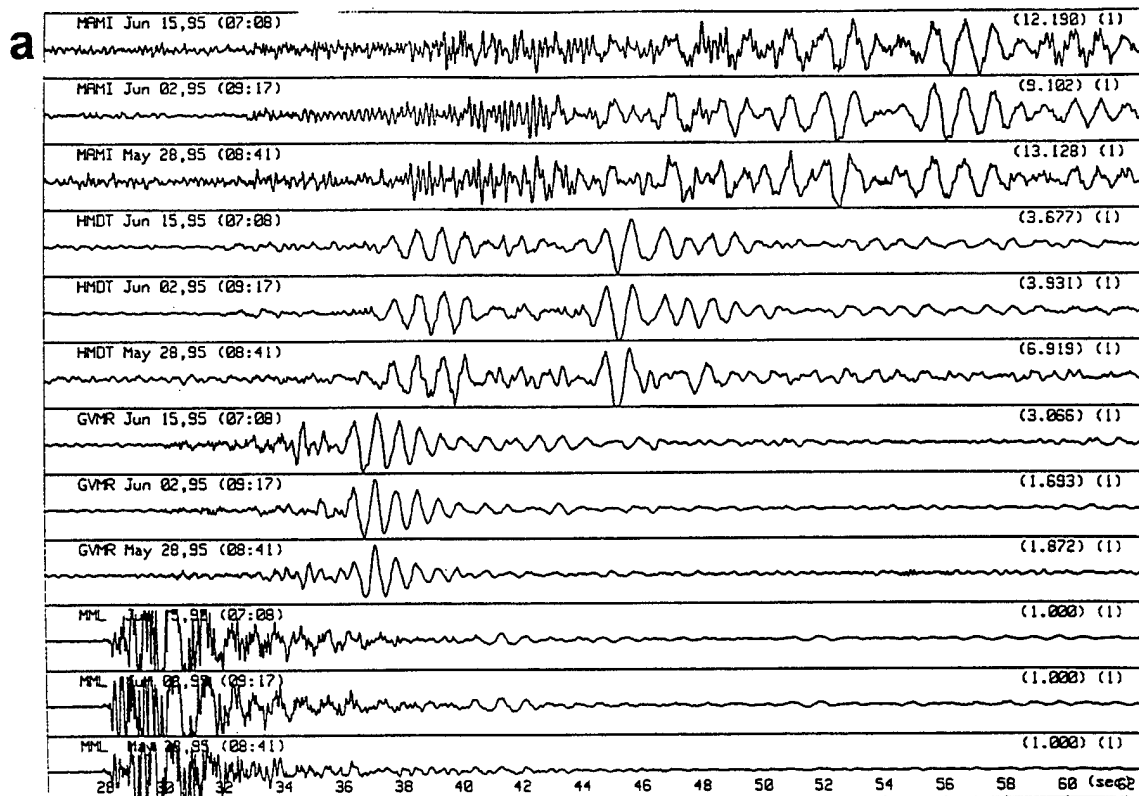
Fig. 21. Three single blasts at Revaya quarry (SB1,SB2,SB3, W=1946-2840kg, r=3-29 km), with prominent surface waves, showing a high identity of wave forms (a) and spectral shapes (b) at station GVMR (analyzed time window t ≈ 20 sec).
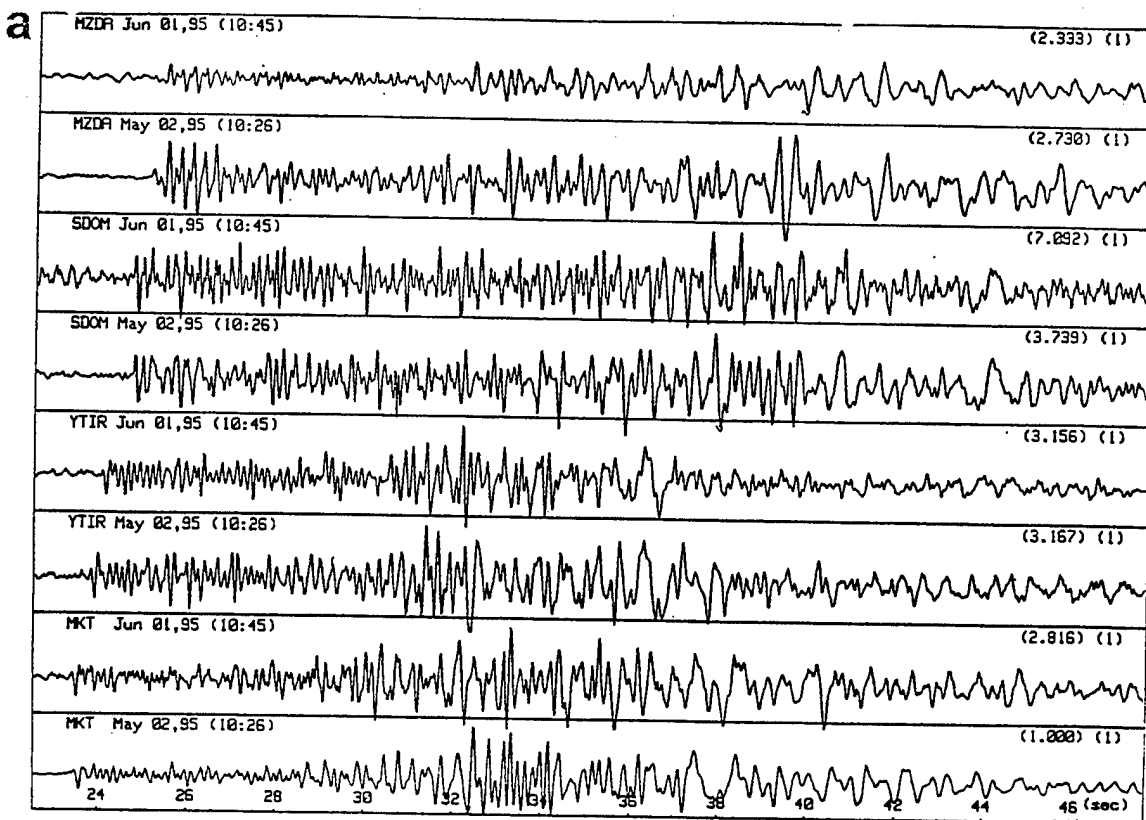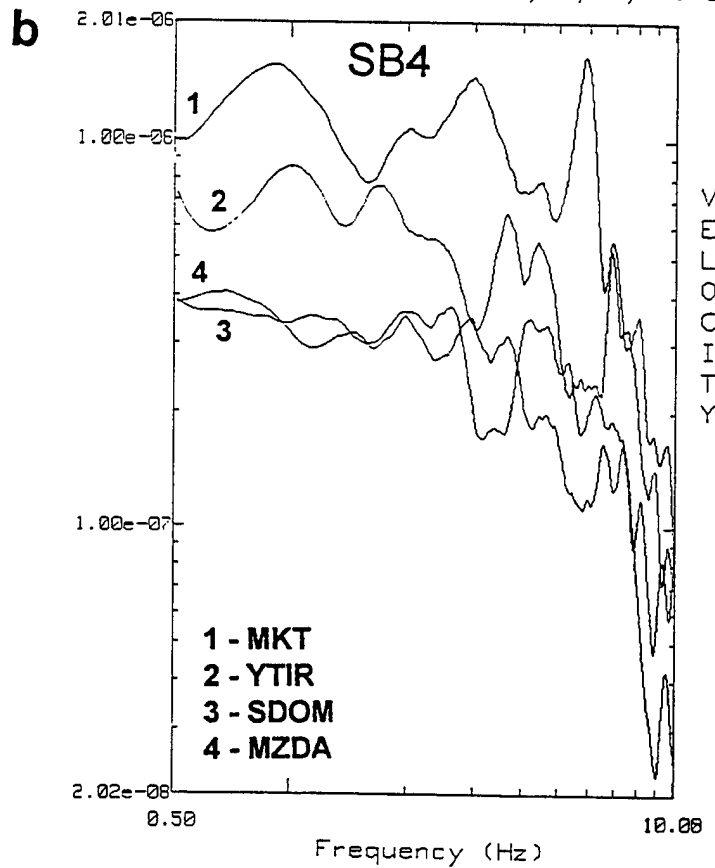
Fig. 22. Two single blasts at Mt.Nitzim quarry (SB4, W=2400kg, SB5, 2200kg, r=22-35km) demonstrating non-regular wave forms (a) and high-frequency spectra (b) at different stations (analyzed time window t ≈ 20 sec).

40

a

Eurasian teleseismic events (ISN records, normins)

29 nuclear tests (•), 39 earthquakes (△)

b

Eurasian teleseismic events (ISN records, rmins)

29 nuclear tests (•), 39 earthquakes (△)
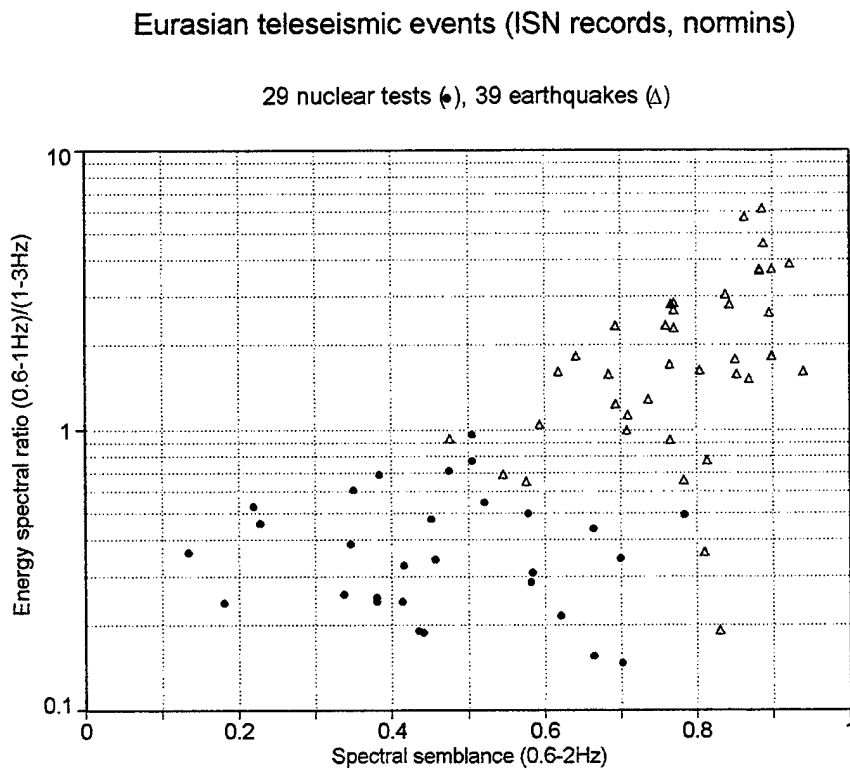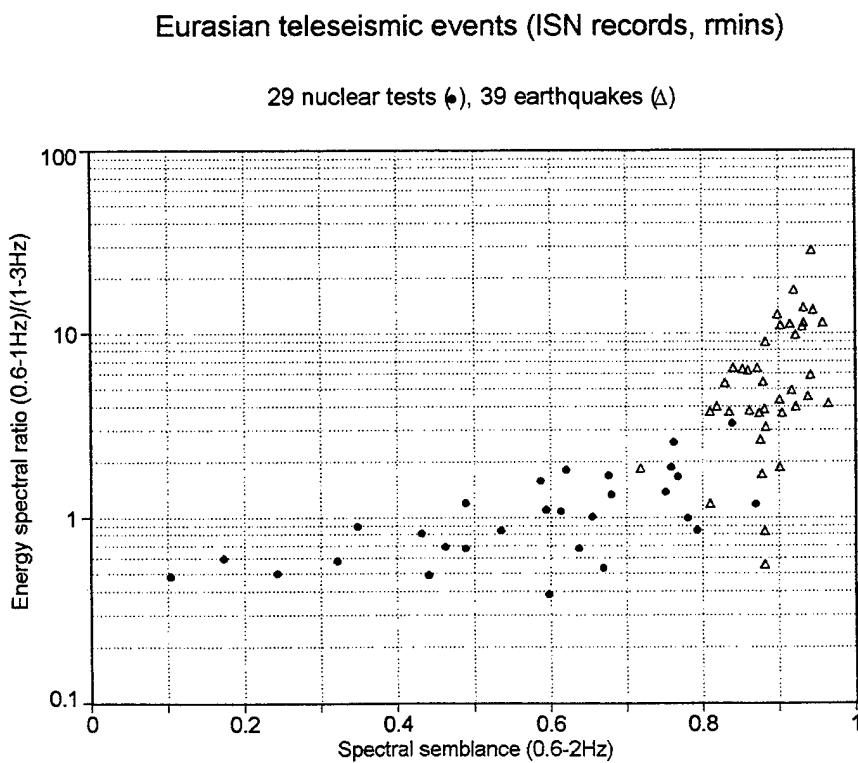
Fig. 23. Discrimination results (spectral semblance vs spectral ratio, at optimal frequency ranges) for teleseismic Eurasian earthquakes and nuclear explosions, based on ISN recordings, without (a) and with (b) remove instrument response.

Chinese nuclear tests at different sites, confirming more high-frequency energy for the explosions than for the shallow crustal earthquakes (e.g. Tailor and Marshall, 1991, for UK teleseismic arrays). This can be explained by a smaller spatial area of energy release for nuclear tests (the finite elastic radius) and shorter duration of the source function (the time rise), as compared to earthquakes (Savage, 1972), which produces a shorter wave length of P-waves. Azimuths of a teleseismic event to the stations are very close (in contrast to local earthquakes), thus significantly increasing spectra coherency. Nevertheless, short-period explosion signals (including scattered waves in P-coda), are more influenced by inhomogeneities in the upper crust beneath the ISN stations spaced several dozen kilometers apart, producing a decreasing of spectra coherency.

The best discrimination performance was provided in the frequency range (0.6-1 Hz)/(1-3 Hz) for averaged spectral ratios and in (0.6-2 Hz) for semblance, calculated over 10-15 ISN stations. It turned out that removing instrument response from the spectra significantly improves the spectral semblance performance (Fig. 23 a,b). Joint application of the two discriminants provided good separation between the earthquake and explosion populations with a few events overlapping.

We tried to track a possible dependence of SS and SR statistics on magnitude and depth (for earthquakes only). The results are presented on Figs. 24 and 25. The only relationship observed is between the spectral ratio and the magnitude (Fig. 24a), which can be explained by increasing the wavelength and low-frequency component of radiated energy for larger events. A visible saturation of this dependence for $m_b>6$ is possibly due to a shift of a fraction of low-frequency energy beyond the high pass cut off (0.2Hz), or the analysis band (0.6-3Hz).

In the NORESS data we found a similar high-frequency character of the P-arrivals for explosions relative to earthquakes (see Figures 26,27), consistent with results of Tsvang et al. (1993). Therefore, spectral ratios, which were calculated (without removing instrument response) for 8-10 stations placed over the entire array (Fig. 26c), showed the same (as for ISN) interrelation between the two populations, whereas the character of the semblance changed to the opposite, i.e. very high ($S_f >0.94$) close values for explosions and lower, in-average, dispersed values for earthquakes (Fig. 28). In this case, owing to the small dimensions of the array (diameter about 3 km), local inhomogeneities in the upper crust and azimuth differences are negligible. We therefore suggest that the main factor affecting station spectra coherency is a waveform character in the 0-15 sec window: a simple predominant P-signal pulse for explosions, and several equal-amplitude signals of different shape for earthquakes.
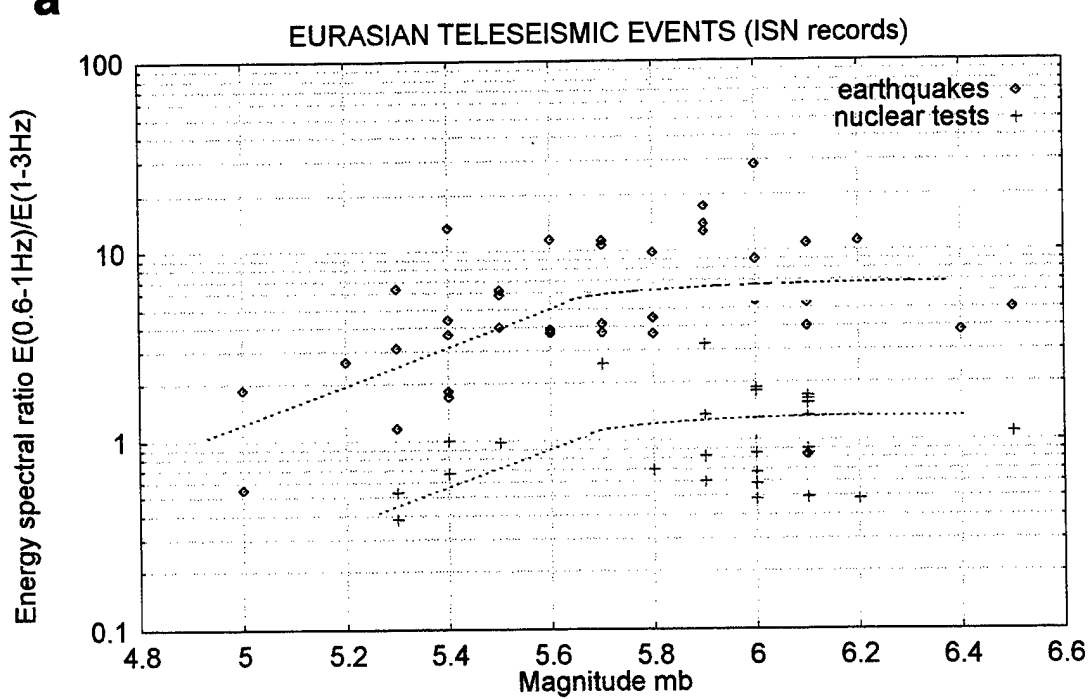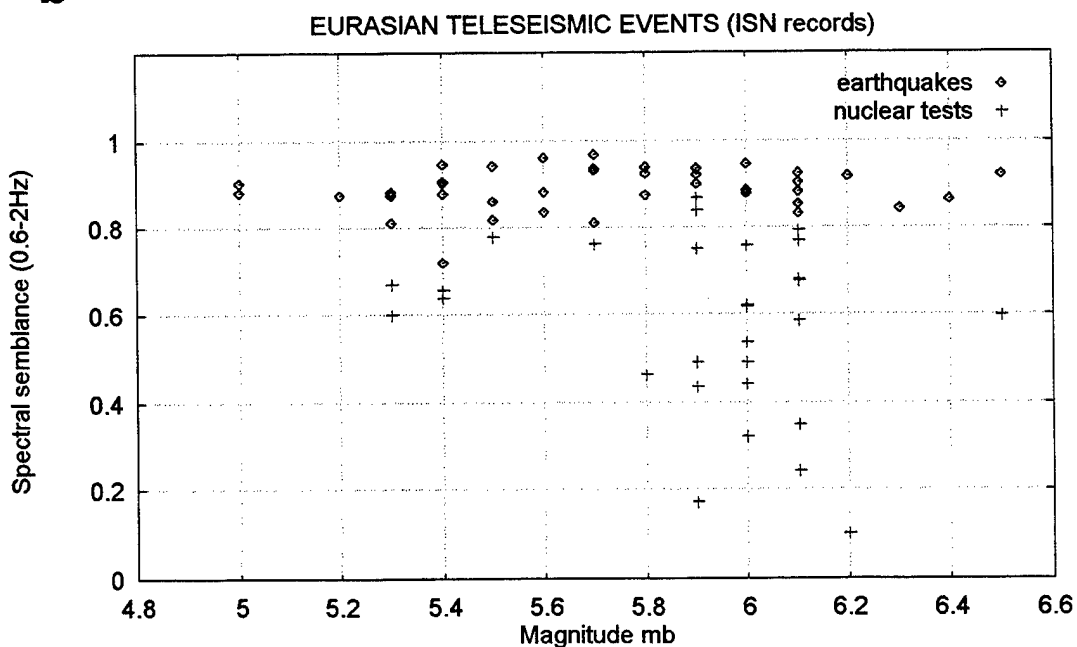
Fig. 24. Spectral energy ratio (a) and spectral semblance (b) vs magnitude for ISN
records of teleseismic events.

a

EURASIAN TELESEISMIC EVENTS (ISN records)

b

EURASIAN TELESEISMIC EVENTS (ISN records)
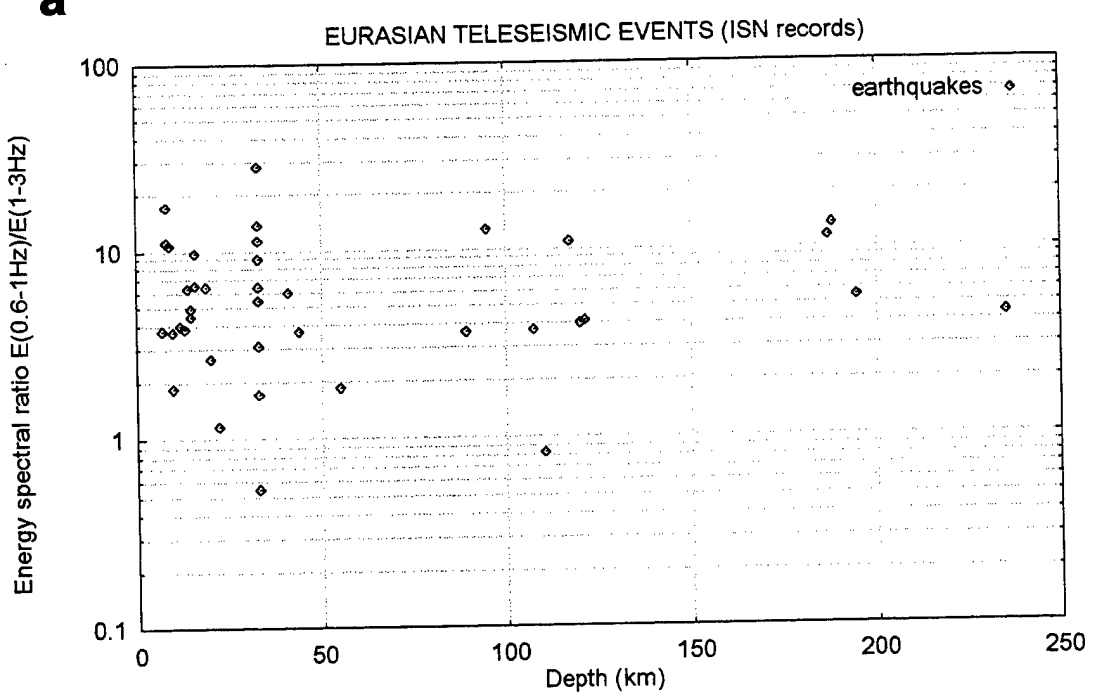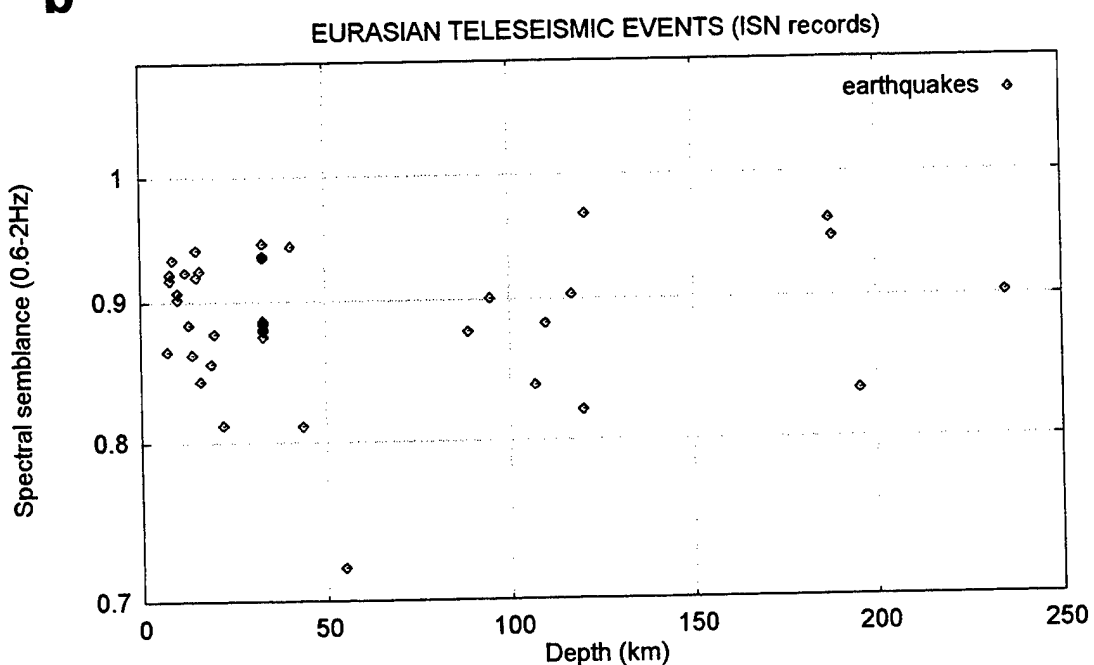
Fig. 25. Spectral ratio (a) and spectral semblance (b) vs depth for ISN records of teleseismic earthquakes.
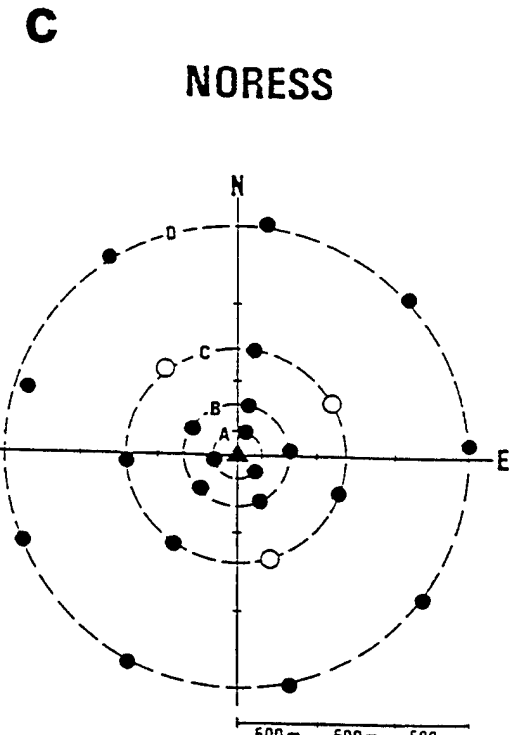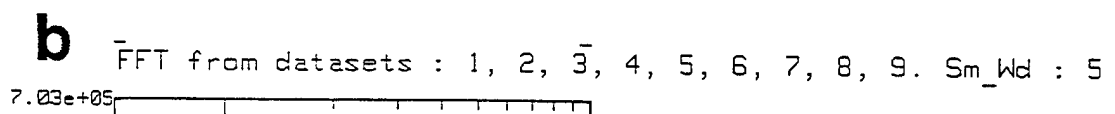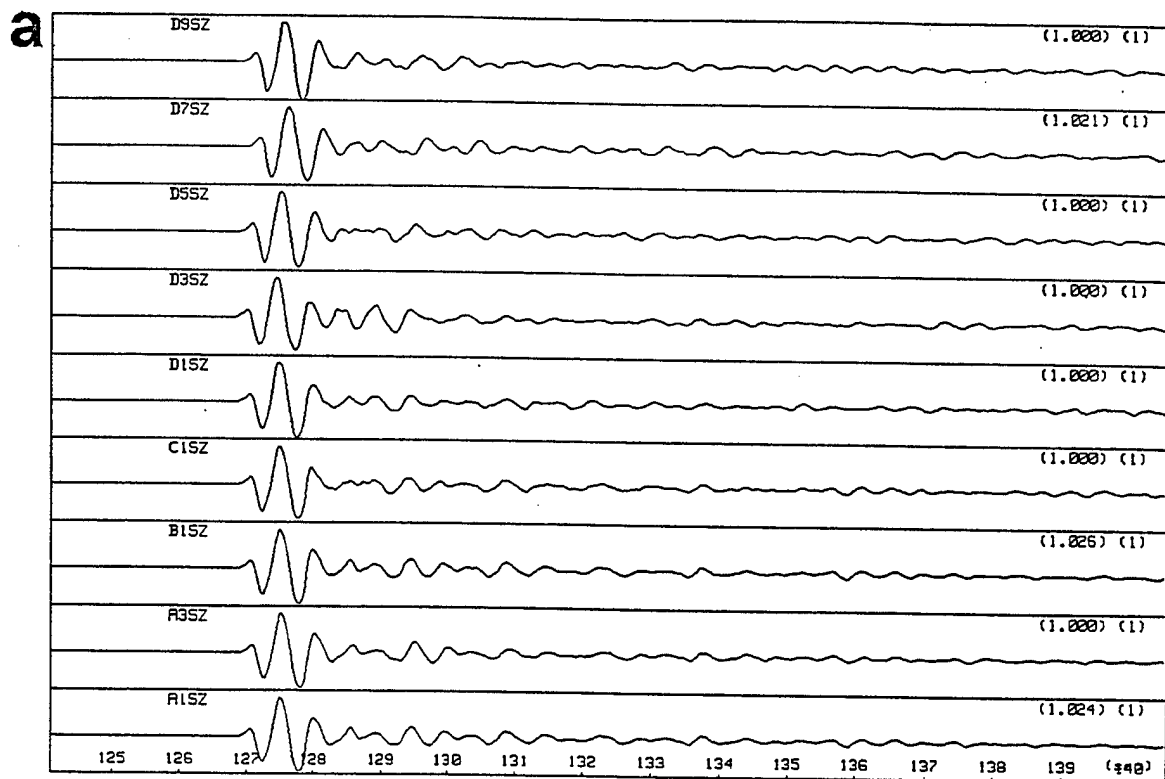
44

Fig. 26. Typical seismograms (a) and spectra (b) of a nuclear test (NT14) recorded at NORESS. The stations used for the analysis are placed on all array rings (c).

45
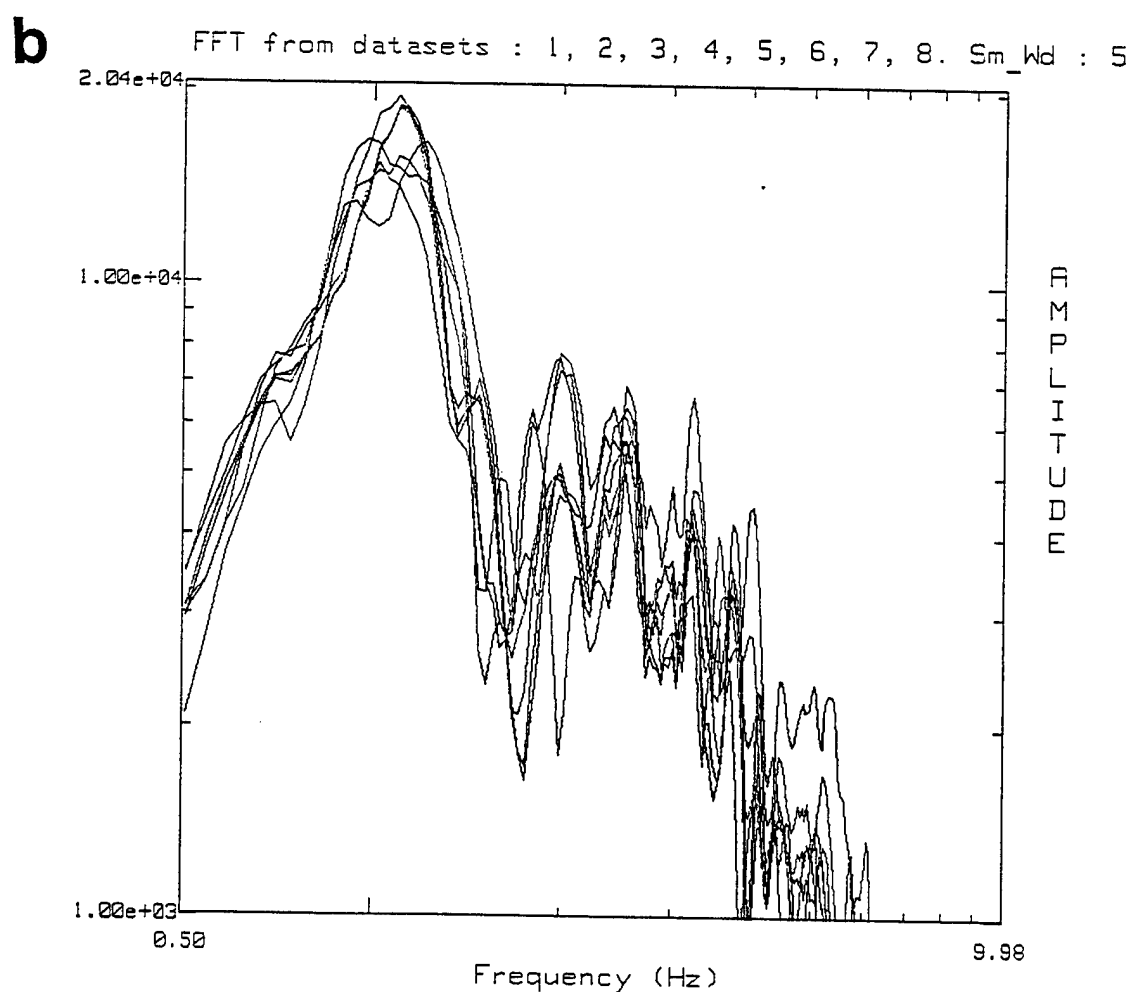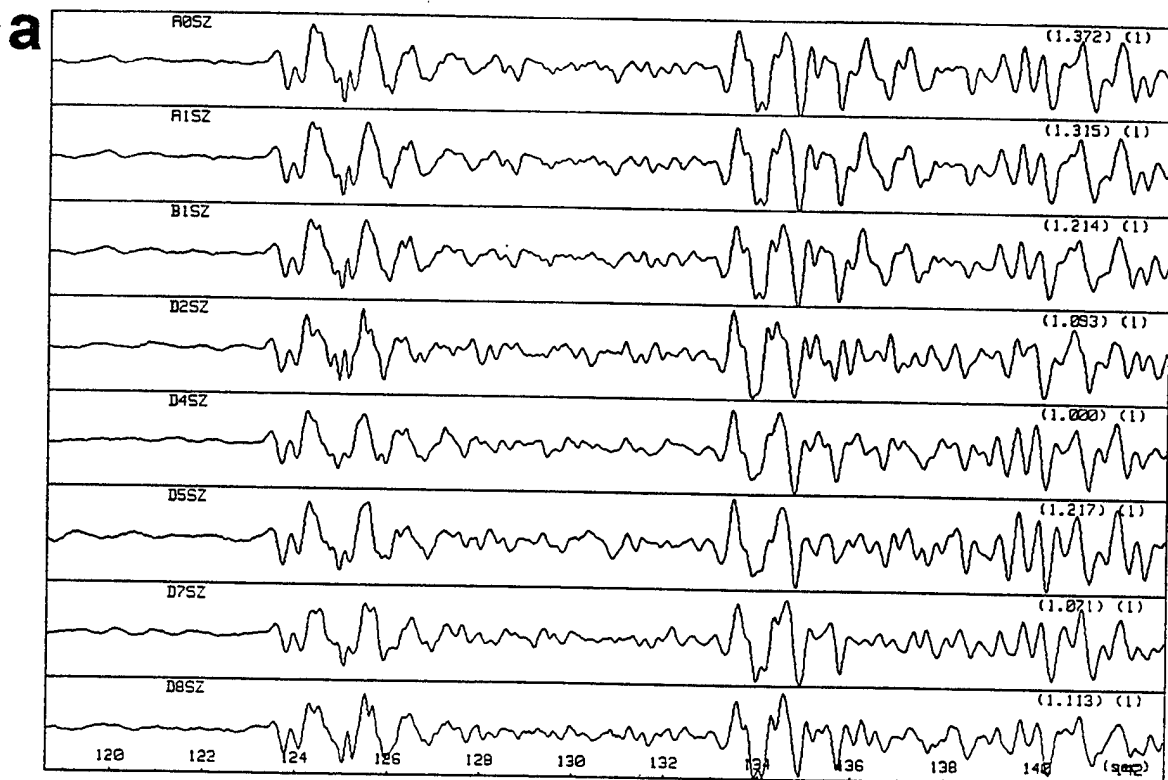
Fig. 27. Typical seismograms (a) and spectra (b) of an earthquake (QU27) recorded at NORESS (analyzed time window t ≈ 13 sec).

46

a

Eurasian teleseismic events (NORESS records)

20 nuclear tests (•), 16 earthquakes (△)

b
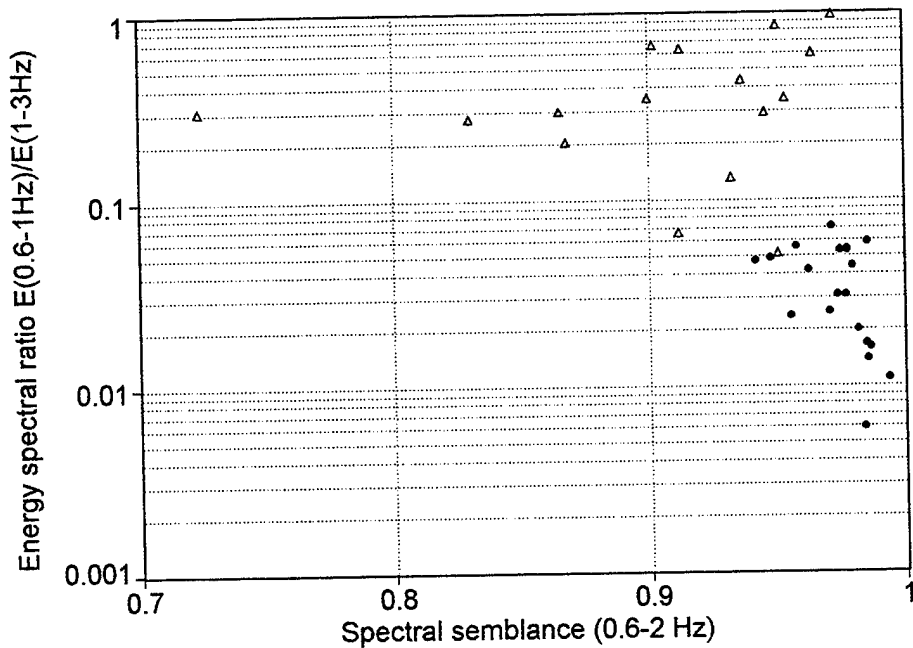
Eurasian teleseismic events (NORESS records)

20 nuclear tests (•), 16 earthquakes (△)
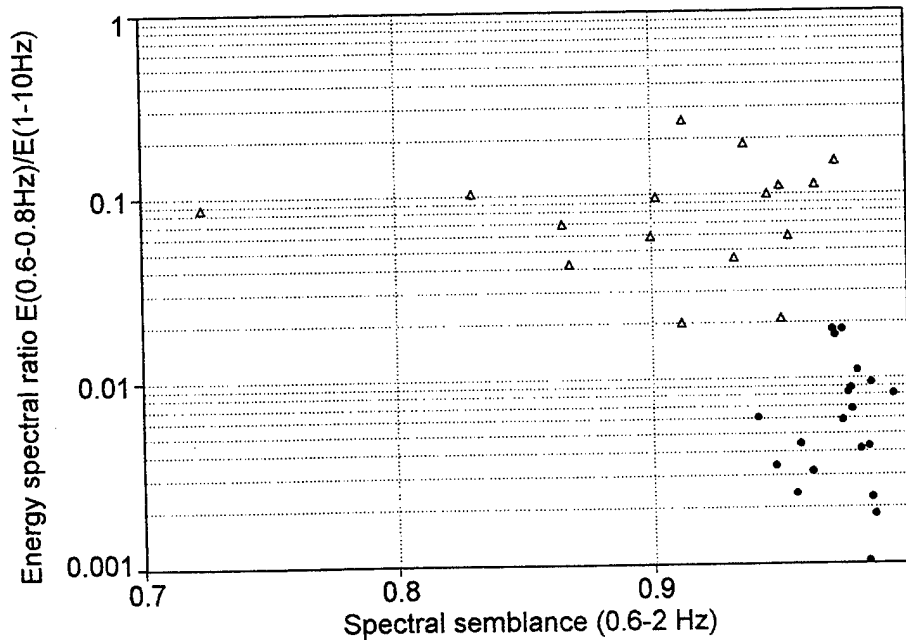
Fig. 28. Discrimination results (spectral semblance vs spectral ratio) for teleseismic earthquakes and nuclear tests, recorded by NORESS. Different frequency bands for spectral ratio are used: (0.6-0.8Hz)/(1-3Hz) (a), and (0.6-0.8Hz)/(0.6-10Hz) (b).

47

Joint application of the two statistics with the same as for ISN frequency bands (0.6-1 Hz)/(1-3 Hz) provided reliable discrimination between the two types of seismic events, with the only outlier being the deep Afghanistan earthquake QU10 (Fig. 28a). By applying different frequency bands (0.6-0.8 Hz)/(0.6-10 Hz), which is actually the normalized low-frequency energy in the very narrow band, we obtained full separation of the earthquake and explosion populations (Fig. 28b).

In general, the spectral ratio performance appears to be better for NORESS recordings, whereas the semblance is better for ISN data.

5.2 Automated classifiers for local and teleseismic ISN records.

Automated Signal Classification (ASC) is a significant challenge in the monitoring of a CTBT. We constructed a reliable automated classifier for regional and teleseismic events identification as a combination of the most promising discriminants and using the advantage provided by the ISN as a regional dense seismic network (RDSN).

Method. We select several useful parameters, choose empirical thresholds and evaluate rate of errors, integrated by the majority voting scheme. Simple majority voting appears to be useful for multidimensional classification analysis of local events, but it does not, however, account for the mutual dependency (cross-correlation) and different weights of scalar statistics and may be regarded only as the first order approximation of error probability. We therefore address more sophisticated classifiers such as the LDF and ANN, applying them to some of the most promising combinations of parameters and evaluate the error probability through the leave-one-out cross-validation test (Fukunaga and Hummels, 1989) to create an independent test data base. The flow chart of the multivariate classification used in the study is presented on Figure 29.

Local training data set for construction of ASC comprises 80 quarry blasts and 65 earthquakes with a magnitude range M_L=1.5-2.5 and a depth range H=0-28 km, from three geologically different non-overlapped regions of Israel and Jordan: the Galilee, southern Dead Sea and Gilad (see map in Fig. 1 and Table 1). These data are part of the general data base described in Chapter 2.1. The events are characterized by enhanced excitation of surface waves for explosions as compared to earthquakes. This is possibly the main reason for the predominant *low frequency* and *coherency* of spectral shapes at different stations, as well as the *lagging behind* of the S-wave trains for explosions as compared to earthquakes.

These three phenomena have been quantified using the following discriminants:

FLOW CHART OF THE MULTIVARIATE CLASSIFICATION
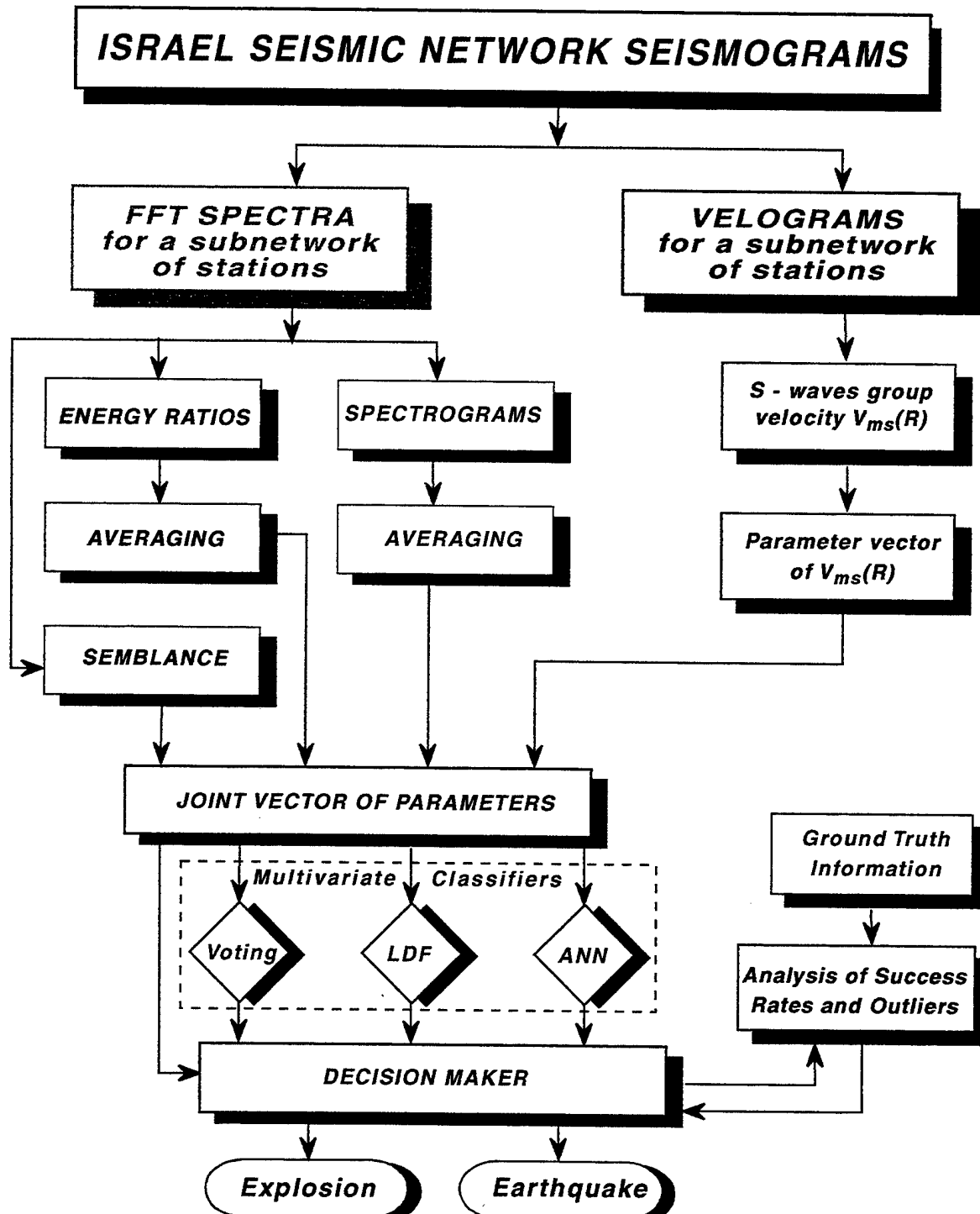
Fig. 29 Flow chart of the multivariate classification

- **spectrogram** for different partition of the (1-11 Hz) frequency band. Two types of *spectrogram* were considered, depending on the normalization coefficient: "spectrogram S1"-normalization by the maximum of the spectrogram coefficients; "spectrogram S2"- by the squared vector norm (signal energy). Separate coefficients of the spectrogram vectors were also considered.

- **energy spectral ratio** - low-/high-frequency ratio, averaged over a set of stations;

- **spectral semblance** - coherency measure of spectral shapes for a set of stations;

- **velogram parameter C** - kinematic scalar discriminant.

All the discriminants mentioned integratively utilize the multistation character of the recordings. Combinations of the discriminants are presented in Table 3. Thresholds for individual statistics, separating blasts and earthquakes, were chosen empirically, to minimize the number of errors. The majority voting, LDF and ANN procedures were applied to the different combinations of statistics. The number of errors for LDF and ANN was estimated by the leave-one-out test.

Table 3. Discrimination results for the local training dataset by Multivariate Procedures

Parameter	Statistic/ Spectral Band	Threshold Level	Number of Errors		
			Voting	leave-one-out-test	
				LDF	ANN
N1	log, spectral ratio, (1-3 Hz)/6-8 Hz)	1.8	2	2	3
N2	spectral semblance, (1-12 Hz)	0.7	4	8	6
N3	velogram parameter, C (1-10 Hz)	0.68	4	9	8
N4	spectrogram S1 coef. N4, (7-9 Hz), 1 band	1.8	2	4	2
N5	spectrogram S1, (1-11 Hz), 5 bands	-	-	4	1
N6	spectrogram S1, (1-11 Hz), 10 bands	-	-	4	5
N7	spectrogram S1, (1-11 Hz), 20 bands	-	-	6	7
N8	spectrogram S2, (1-11 Hz), 5 bands	-	-	6	4
N9	parameter vector (N1, N2, N3)	-	2	4	4
N10	parameter vector (N1, N2, N3, N5)	-	1	4	3

Results of the local events classification using the four scalar statistics specified in Table 3 are presented in Fig. 30 together with depth specification at the top and the results of majority voting at the bottom. The data in Fig. 3 are split according to regions of the event locations. The Voting is defined as the sum of units for the "correct vote" and zeroes for the "wrong vote"; hence a "correct" majority decision corresponds to the Voting>2 for the four voters case. The results of the analysis of Fig. 30 are as follows:

- The statistics selected exhibit from good (four errors for the _semblance_ and the _velogram parameter C_) to excellent (two errors for the _spectrogram_ 7-9 Hz and the _spectral ratio_); 144 events out of 145 are correctly classified using the majority _Voting_ >2 criterion.

- The worst _Voting_=1 is obtained for event N119 (QS9) - an earthquake from the Dead Sea region with zero depth specification. The only positive voice for it belongs to the _velogram parameter C_.

- 11 events have _Voting_=3 value and are correctly classified. Only one of these earthquakes, event N120 (QS10), may be specified as shallow.

Fig. 31 A,B presents the results of the _Error probability_ estimation by the leave-one-out test for the LDF and ANN, applied to the statistics described in Table 3. Fig. 31 shows that the error probability for the classifiers varies between 0.6% to 6.2%, where, on average, ANN performs better than LDF. The best computational scheme is ANN + _spectrogram N1 (5 band case)_, which provided only one mistake for the Dead Sea earthquake (QS9). The second place with an error probability of 1.4 % shares the ANN + _spectrogram N1 (7-9 Hz)_ (relative energy in the 7-9 Hz band) and LDF + Energy _Spectral ratio_ - both scalar statistics.

Teleseismic training data set is described in Chapter 2.2. The seismograms of the nuclear test are characterized by relatively higher frequencies of particle motion and impulse shape of the P-wave onset. Most of the explosions (18) are from the Shagan river (Semipalatinsk) test site, eight from China (Lop Nor), one from Western Siberia and two from Novaya Zemlya test sites. The nuclear detonations took place in various geological conditions and show significantly different waveforms, sometimes similar to those of earthquakes. The deep events, mostly from northern Afghanistan, exhibit usually impulsive P wave seismograms similar to most of nuclear tests mentioned above (see Fig. 32).

On this data set we investigated the combinations of _P/P-coda ratio, spectral semblance_ (0.6-2 Hz) and _energy spectral ratio_ (0.6-1 Hz)/(1-3 Hz) statistics. The last two spectral statistics were investigated in two modes: with and without prefiltering of the seismograms by the (0.5-5 Hz) Butterworth filter.
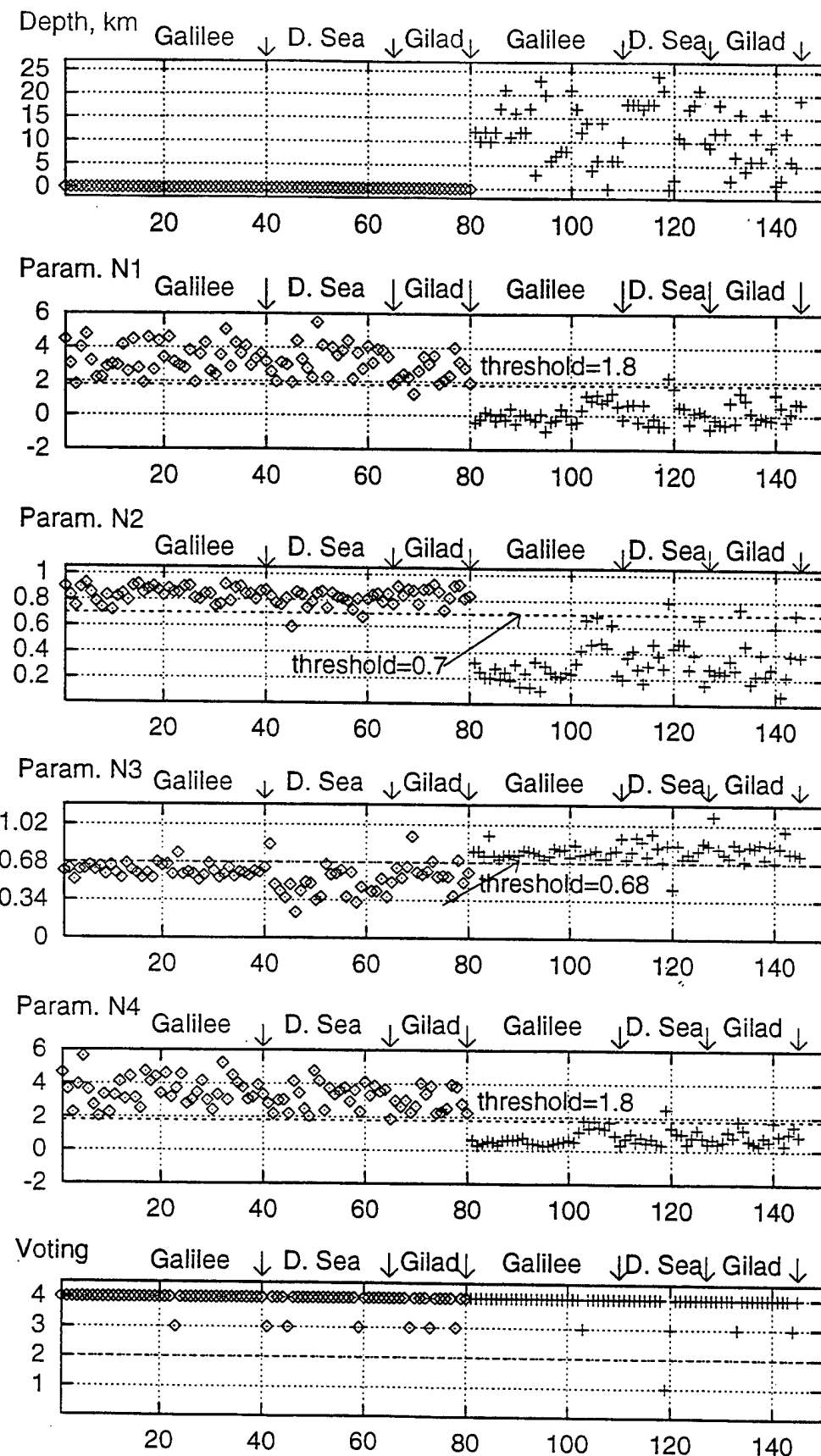
Fig. 30. Majority voting for the four main scalar statistics (parameter numbers from Table 3), applied to the ISN records of 80 quarry blasts (◊) and 65 earthquakes (+) from Galilee, Dead Sea and Gilad region (local training data set).
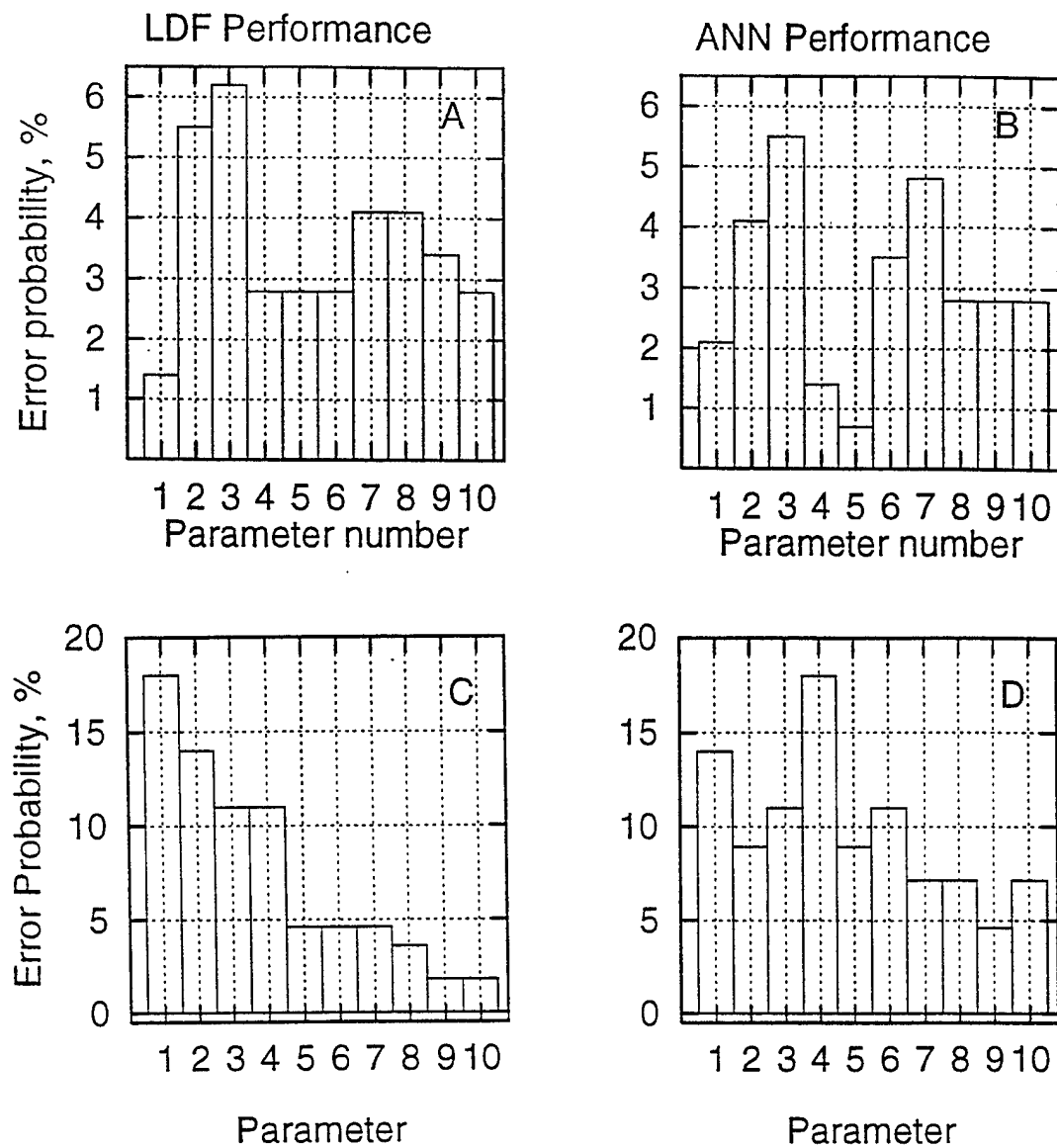
Fig. 31. Error probability estimation by the leave-one-out test of the LDF and ANN procedures, applied to: (A,B)-local training data set (parameter numbers from Table 3); (C,D)-teleseismic training data set (parameter numbers from Table 4).
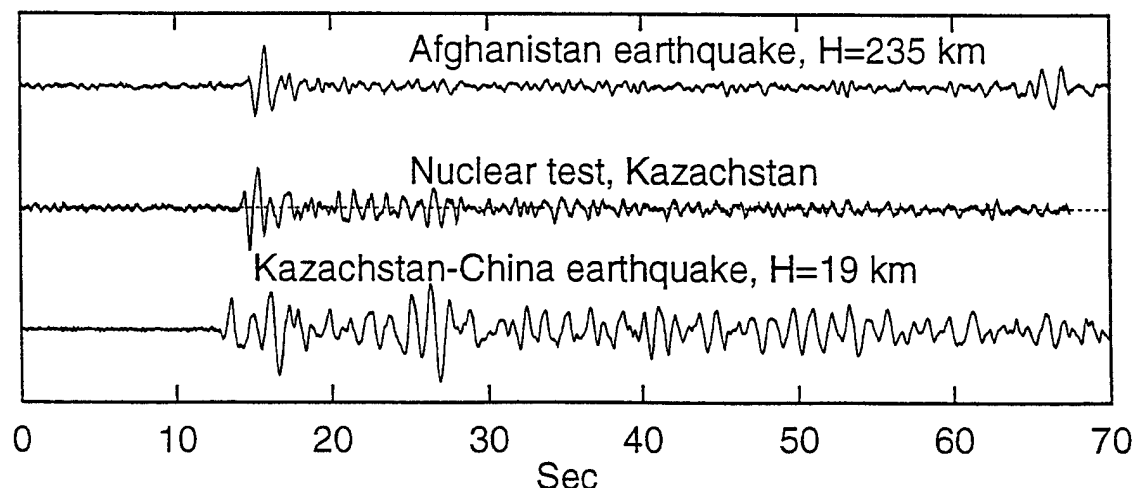
Fig. 32. Examples of typical teleseismic records from the DSI station of the ISN: deep earthquake, nuclear test and shallow earthquake.

For calculating the P/P-coda parameter the only automatically selected channels are those with SNR>3. As a result there were 3 to 30 ISN channels per event which were used to calculate the statistic average. The above mentioned scalar discriminators and their combinations are presented in Table 4.

Results of the teleseismic events classification are presented in Appendix Tables A3 and A4 (together with depth specification and empirical thresholds), Table 4 and Fig. 31 C,D. From the 3-voice majority voting analysis it follows that:

- Nuclear tests have on average larger values of P/P-coda ratio than earthquakes and lower values of Semblance (0.6-2 Hz) and Energy Spectral ratio (0.6-1 Hz)/(1-3 Hz), but no single parameter separates the data sets completely.

- Each threshold corresponds to a pair: number of wrongly classified nuclear tests and number of wrongly classified earthquakes. For empirically selected thresholds these numbers are: {0,9} for P/P-coda ratio, {5,5.5} for Semblance 1, {1,6} for Spectral ratio 1, {2,1} for Semblance 2 and {6,4} for Spectral ratio 2.

- When only shallow earthquakes are considered the relative number of errors is reduced: {0,2} for P/P-coda ratio, {5,2.5} for Semblance 1, {1,2} for Spectral ratio 1, {2,0} for Semblance 2, {6,3} for Spectral ratio 2.

- Voting procedure for the case "with prefiltering", applied to the whole data set, results in five errors: earthquakes QT10 (deep Afghanistan), QT30 (deep Tibet), QT25 and QT38 (shallow, China) and QT36 (shallow, Kirgizia) with no misclassifications for nuclear tests. If only 27 shallow earthquakes are considered, we observe identification errors for three earthquakes.

- Voting procedure for the case "without prefiltering", applied to the whole data set, results in two errors: nuclear test NT18 (Novaya Zemlya) and earthquake QT30 (deep Tibet).

- If only shallow earthquakes are used for classification, then the combination of all five parameters mentioned is error free as a result of majority voting (see Table 4).

The LDF and ANN classifiers applied to the three selected scalar discriminators and their combinations were tested on the reduced data set comprising 29 nuclear tests and 27 shallow earthquakes. The results of the leave-one-out cross-validation test, presented in Table 4 and Fig. 31 C,D are as follows:

- Each of the scalar discriminators provides some misclassifications for {LDF, ANN} on the selected data base: *P/P-coda* - {3,5} mistakes, *Spectral ratio1* - {6,6} mistakes, *Spectral ratio2* - {6,10} mistakes, *Semblance1* - {10,8} mistakes, *Semblance2* - {8,5} mistakes.

- Combinations of the scalar discriminants reduce classification mistakes with the best variant giving one classification mistake: the vector (T1,T2,T3,T5)+LDF. The error is in identifying the nuclear test NT18 (Novaya Zemlya).

Table 4. Discrimination results for the teleseismic dataset (27 shallow earthquakes and 29 nuclear tests) by multivariate procedures.

Parameter	Name, Spectral Bands	Threshold	Voting	leave-one-out-test LDF	leave-one-out-test ANN
T1	SEMBLANCE 1 Spectral semblance (0.6-2 Hz) with prefiltering (0.5-5 Hz)	0.65	7.5	10	8
T2	SEMBLANCE 2 Spectral semblance (0.6-2 Hz) without prefiltering	0.8	2	8	5
T3	LOGSPECTRAL RATIO 1: Logarithm of spectral ratio (0.6-1Hz)/1-3Hz) with prefiltering (0.5-5 Hz)	-0.11	3	6	6
T4	LOGSPECTRAL RATIO 2: Logarithm of spectral ratio (0.6-1Hz)/1-3Hz) without prefiltering	0.47	9	6	10
T5	P/P-CODA RATIO with prefiltering (0.5-5 Hz)	2.3	2	3	5
T6	Parameter vector (T2,T3,T5)	-	3	3	6
T7	Parameter vector (T2,T4,T5)	-	1	3	4
T8	Parameter vector (T1,T3,T5)	-	2	2	4
T9	Parameter vector (T1,T2,T3,T5)	-	3	1	3
T10	Parameter vector (T1,T2,T3,T4,T5)	-	0	1	4

As a result of the analysis facilitating the *multistation Integrative Approach*, the Fisher Linear Discriminator Function and the Artificial Neural Network procedure, we selected the following features most informative for classification of man-made and natural seismic events and drew the following **conclusions**:

Local events

- The best classification results with an error probability equal to 0.006 were achieved by ANN at the 5 band Spectrogram S1.

- The scalar statistics of Spectral ratio (1-3 Hz)/(6-8 Hz) and the Spectrogram S1 (7-9 Hz), which greatly resemble each other, are the closest competitors. Their success is explained by the physical phenomenon of the excitation of the long period surface waves by explosions in the region with thick subsurface sediments.

- The more complicated and interesting spectral semblance and velogram parameter C discriminators lag slightly behind with an error probability equal to ~0.04.

- The only event of 145 which is misclassified in the best case mentioned above, is the Dead Sea earthquake which is estimated as being located at a very shallow depth. Misclassification occurred due to the excitation of low frequency (about 0.6 Hz) surface wave energy observed at some of the nearby stations.

- Although the data belong to three different geological areas, it was handled without splitting and with good classification results, thus showing robustness and transportability of the classification procedures designed.

Teleseismic events

- Events of magnitude 5 and higher provide sufficient signal-to-noise ratio at the ISN stations to perform reliable classification of earthquakes and nuclear tests from Eurasia.

- P/P-coda ratio classifier, as well as the energy spectral ratio seem to be favorable at NORESS, appear to be useful at ISN, when the statistics, evaluated for the individual channels, are averaged over subnetworks of stations.

- The new spectral semblance statistic, measuring coherency of spectra at different stations, demonstrates high performance in the classification of earthquakes and nuclear tests in the low frequency range (0.6-2 Hz). The effect may be explained by frequency dependent subsurface scattering.

- BP filtering of the seismograms (0.5-5 Hz) enhances performance of the spectral ratio statistic and reduces performance of the semblance statistic.

- Joint application of the five selected parameters in the majority voting procedure provides full separation of the data set, comprising nuclear tests and shallow earthquakes.

6. APPLICATION OF ARRAY METHODS TO TELESEISMIC ISN RECORDS.

6.1 Characterization of the Array Technique.

Array technique, namely beamforming and F-K analysis applied to the closely spaced and synchronized stations has the potential to extract signals with greater detectability than the network technique. This has been proved by the experience obtained from the European seismic arrays such as NORESS, ARCESS in Norway (Mykkeltveit et al., 1990), FINESS in Finland (Uski, 1990), GERESS in Germany (Jost, 1996) and others.

Two main conditions are required for realization of this advantage: coherency of signals at different stations and stationary noise. Statistically, in the case when signal is coherent and noise is stationary multivariate random process with independent equal variance components, the SNR is enhanced at the output of a beamformer as a factor of N, where N is the number of stations. Experimentally the standard beamforming has proved to be efficient at the NORESS-type microarrays (25 short period stations, ~3 km radius) for enhancing weak event signals. Utilization of the noise covariance matrix function leads to an increase in microarray efficiency. As shown by Kushnir et al. (1990), application of the adaptive beamforming technique (ABT) to the microarray data may enhance SNR dramatically (much more than a factor of N), provided the noise is coherent.

The large aperture arrays, such as NORSAR (100*100 km area) are probably less effective in signal detection, but, for relatively large events, provide far greater precision in location than microarrays. Similar results are expected from the application of the array procedures to ISN subnetworks. This is explained by the fact that the signal is no more coherent at the stations separated by tens of kilometers even for teleseismic events and noise is often not stationary and not coherent at the time intervals of interest.

An important feature of the regional network is that the level of noise at different stations may vary considerably, so that it may be reasonable to expect higher detection capabilities from the best station rather than by applying the array technique. We applied array technique to the ISN channels and carried out the following experiments:

- Investigation of pure noise suppression and weak signals extraction using beamforming and adaptive beamforming techniques for the ISN subnetworks.

- Apparent velocity and azimuth estimation for the relatively small teleseismic events using advanced statistical methods for the P-phase onset estimation and alignment of records.

6.2 Regional Network Noise Investigation

The above question can be statistically formulated in terms of the following:

Theorem: Let us assume that noise components are independent stationary Gaussian time series. Let W, denote spectral density (j=1,.., N-number of stations) at a fixed frequency, and the signal is a scalar Gaussian stationary process (true approximation in a small time window) similar for all channels $S(t)=S_j(t)$, with spectral density F at the same frequency as above. Let us evaluate SNR at the output of beamformer as spectral ratio. Then:

$$SNR = N^2 F / \Sigma(W_j) < N F / W_{min} \tag{6.1}$$

and SNR at the output of adaptive beamformer will be

$$SNR = F \Sigma(1/W_j) > F / W_{min}. \tag{6.2}$$

Corollary: If NW_{min} is less than average W_j, then it is better to select a channel with a noise level lower than the beam, but an adaptive beamformer will always be better. From Eqs. (6.1) and (6.2) it is may also be seen that if the noise level is the same and uncorrelated at all the stations, the beam SNR = F*N/W , is equal to the SNR at the output of the adaptive beamformer.

Experimental results. We selected a 2.6 minute interval of pure noise from 14 stations spread over the ISN as shown on Figs. 33a and 33b, where traces are scaled together. A stationary noise character in most of the traces and a lack of correlation between stations are observed and from Fig. 33b we see that the noise level from station to station differs significantly. The standard beamforming technique (SBT) of traces (simple stack) and adaptive beamforming technique (ABT) were applied to the different ISN subnetworks.

The results of application of the SBT and ABT (10 coefficients, 100 sec adaptation interval) to all the 14 stations are shown on Fig. 34. Station HRI has the lowest noise level (three times less than the second to it, PRNI station). From Fig. 34a it is obvious that the SBT output noise level is worse than that for the best HRI channel, while the ABT has approximately the same noise level as HRI. When HRI is excluded from observations, PRNI becomes the channel with minimum noise level, but there are nine channels (3, 6-14) with approximately the same noise level (Fig. 33b).
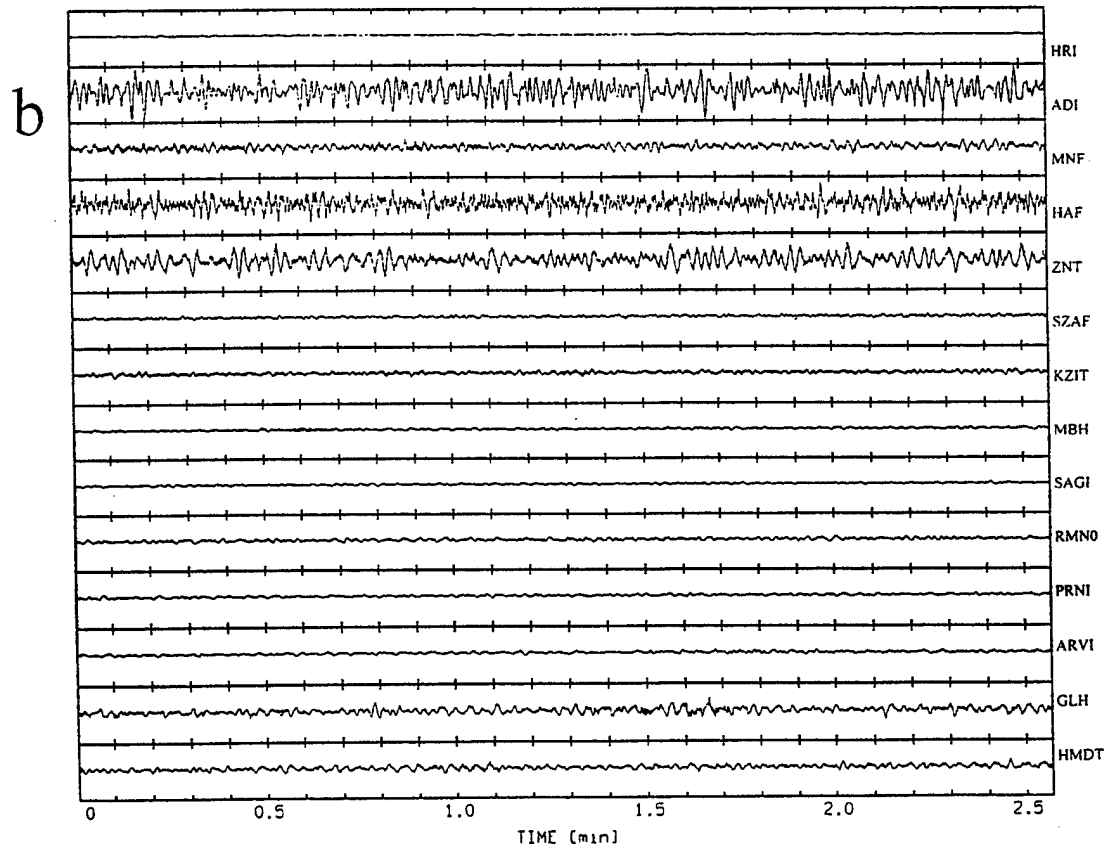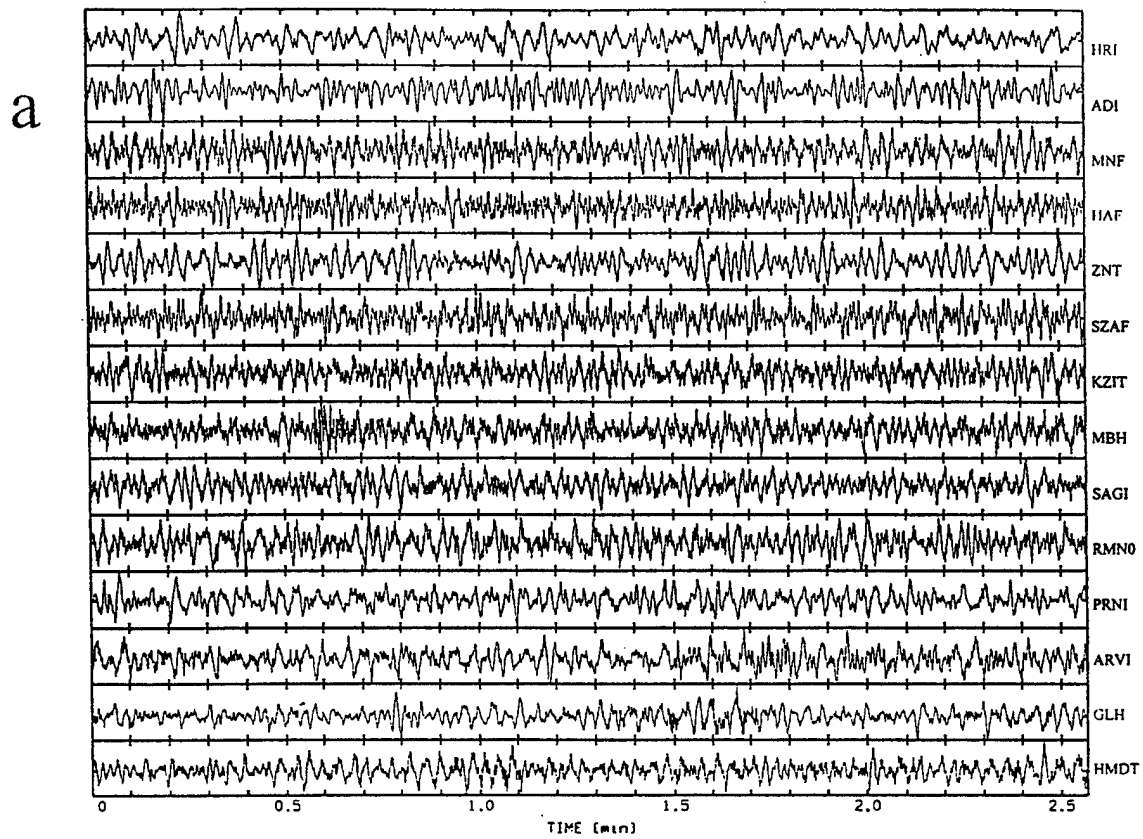
Fig. 33. Seismic noise recordings at the 14 ISN stations before (a), and after (b) normalization.

59
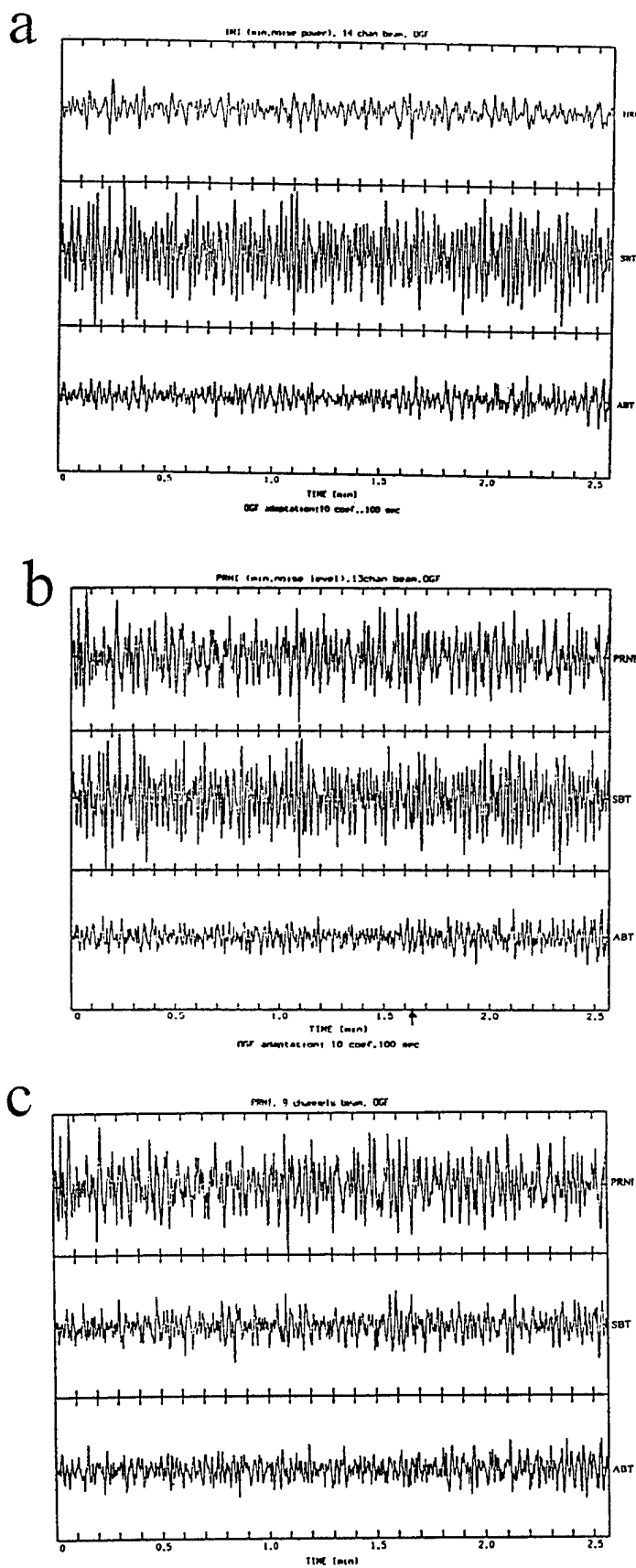
Fig. 34. Application of the standard beamforming (SBT) and the adaptive beamforming (ABT) to ISN noise for: (a) 14 channels including the most "quiet" HRI station; (b) 13 channels without HRI; (c) 9 channels with approximately equal noise level.

Fig. 34b illustrates application of the SBT and ABT to the remaining ISN channels (13). We see that the beam trace here is still worse than the channel with minimum noise level and the ABT is the best trace. While applied to the nine channels (3, 6-14) with approximately equal noise level, the beam and the ABT have approximately equal noise levels at the output, but less than that at PRNI station, having minimum noise level in the selected subnetwork (see Fig. 34c)

The experimental results agree with the theoretical expectations that in the case where noise levels vary significantly from station to station, selection of the station with minimum noise level should be preferred to the evaluation of beam, but an adaptive beamformer will provide results which are not worth than simple selection of the best channel.

We tested also detectability of the array methods using ISN records of real signals of relatively weak and remote events. On the Fig. 35 there is an example of the seven ISN stations records of the small (m_b=5.4) teleseismic event QT18 from Afghanistan. The simple waveform and high coherency of the signal may be observed here. The SNR for the individual ISN channels is low and was enhanced by the application of the array technique (see Fig. 35b), yielding a higher SNR than for that of the best channel (station RMN). The ABT (25 sec of adaptation, 5 coefficients) further improves the SNR. The traces were preliminary aligned using the method described below. For another event QT25 (m_b=5.3) from China, the results of application of the beam and ABT are similar to the previous example (Fig.36).

6.3 Apparent Velocity and Azimuth Evaluation.

The beam detector is based on scanning the SNR for arriving seismic phases over a pre-specified grid of slowness S=(Sx,Sy). The beam largest SNR provides estimate S_{max} and corresponding seismic phase apparent velocity $v=1/|S_{max}|$ and azimuth $Az(S_{max})$ to the source. Each grid point Sx=|S|*cos(Az), Sy=|S|*sin(Az) corresponds to the specific delay of signal arrivals to the array stations due to their different locations in space. Thus the estimator can be found through a grid search to which best frequency band may be added, through prefiltering by a series of band-path filters or Fourier transform. The large scale scanning renders this search rather exhausting and complicated for providing accurate solutions, which is why we preferred to use somewhat different logic.

For the alignment of seismograms we used an automatic procedure comprising high sensitivity, 1-component optimal detector (OD) (Kushnir et al, 1983), accurate 1-component maximum likelihood on-set estimator (MLOE) (Pisarenko et al., 1987) and advanced phase

61
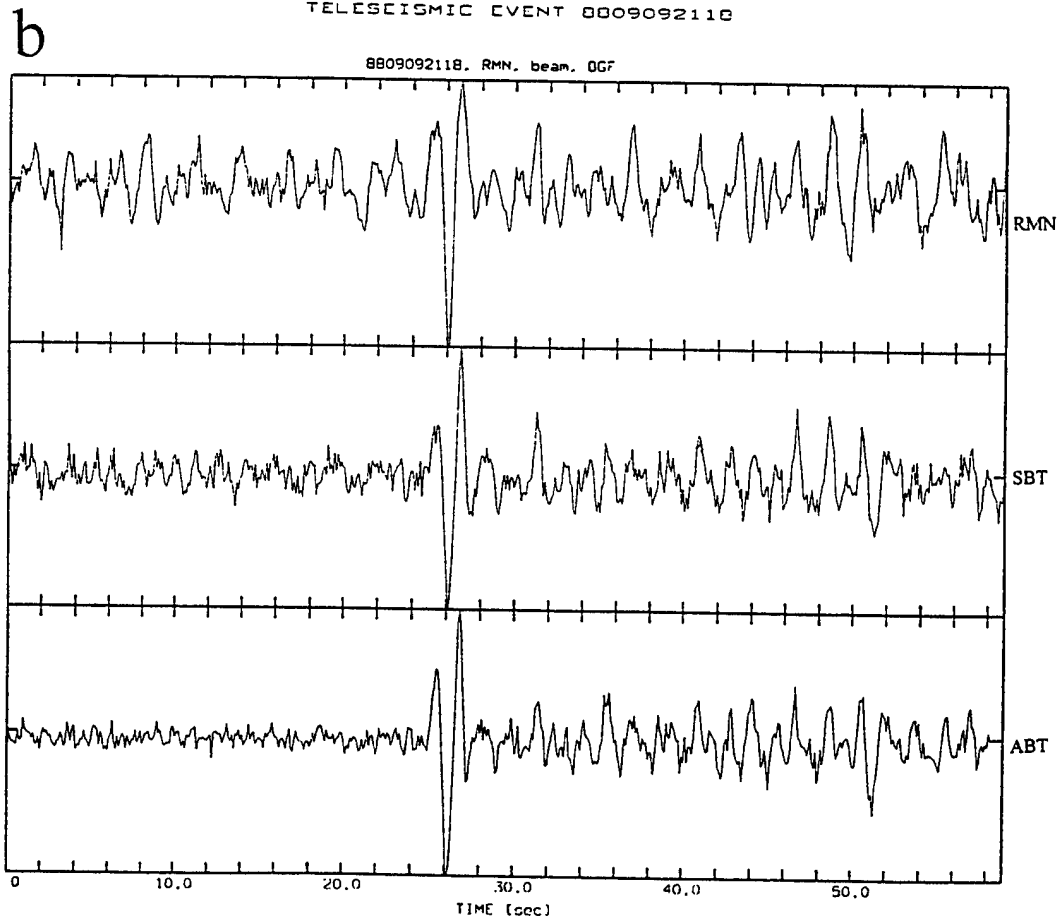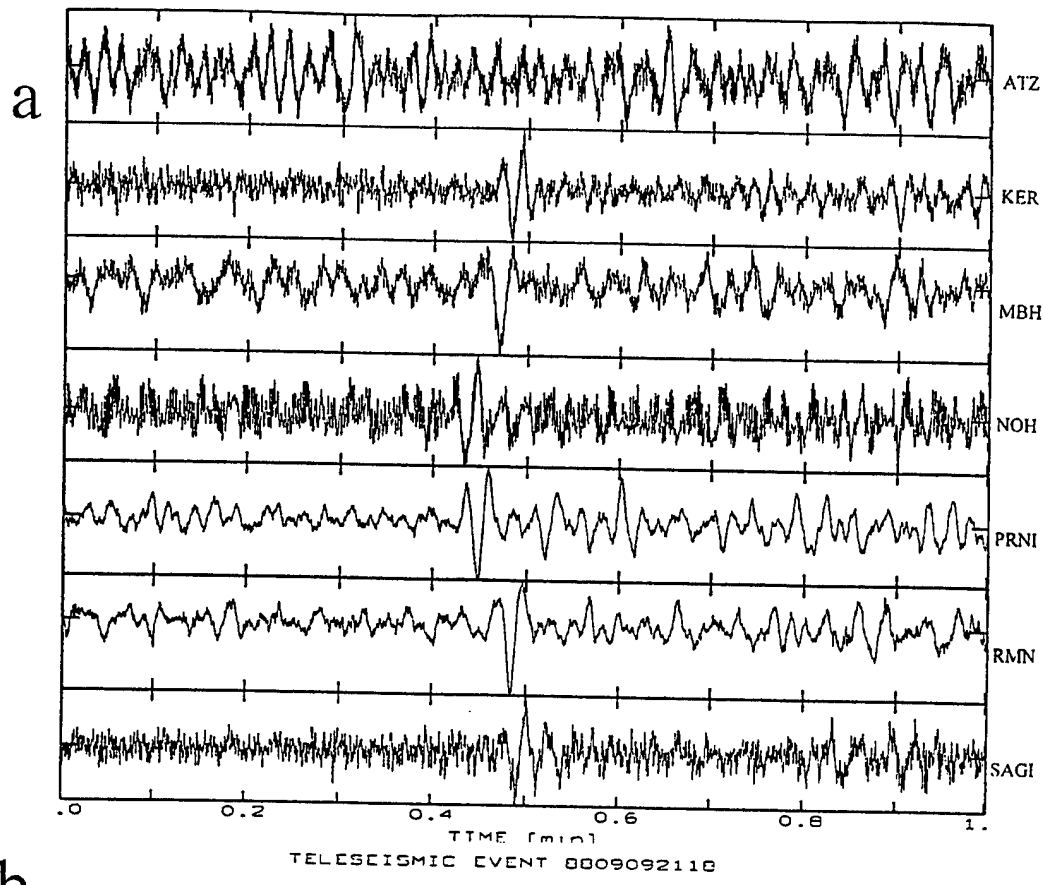
Fig. 35. Aligned traces of the small (m_b=5.4) teleseismic event QT18 from Afghanistan at 7 ISN stations (a); application of standard beam (SBT) and adaptive beamforming techniques (ABT) to the ISN subnetwork and comparison with the "best" RMN station (b).

62

a

KSR
KZIT
MAMI
PRNI
RMN
RTMM
SDOM
ZNT
SBT

TIME [min]

9010242345.PRNI (best of 8).OGF

b

PRNI

SBT

ABT

TIME [min]

adaptation:25 sec.5 OGF coefficients
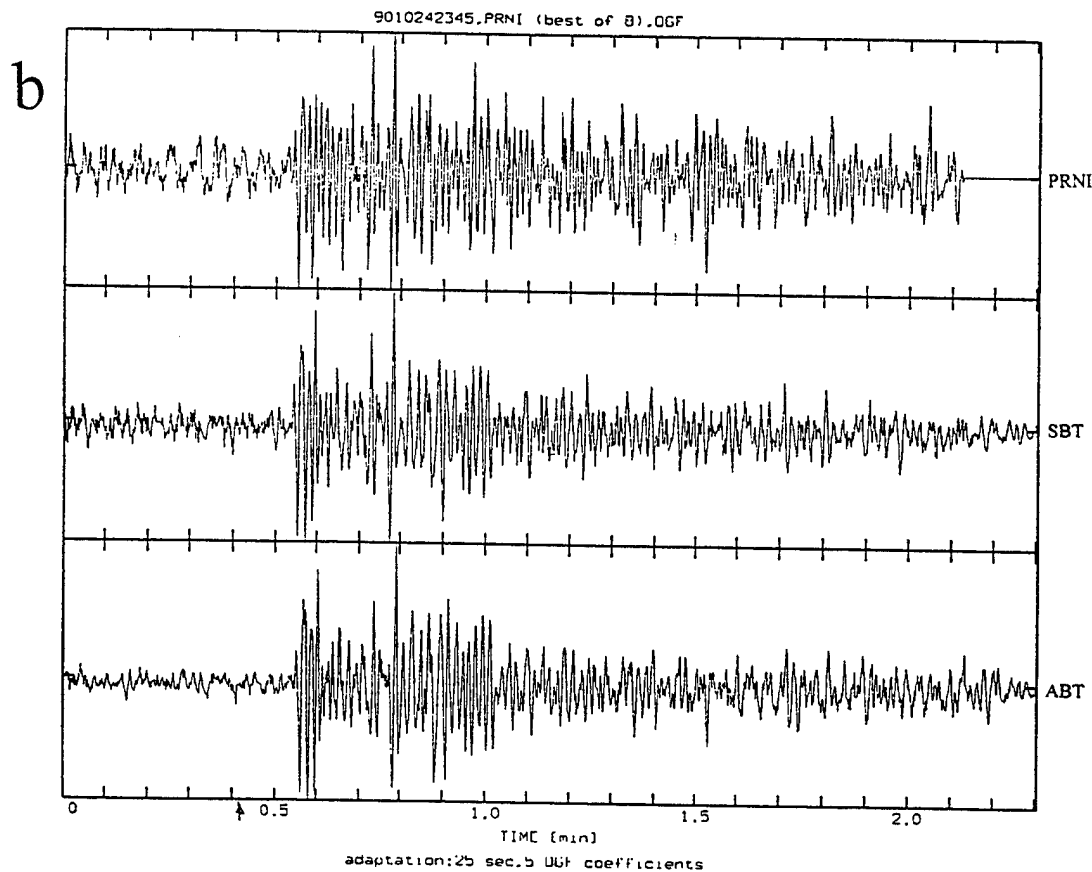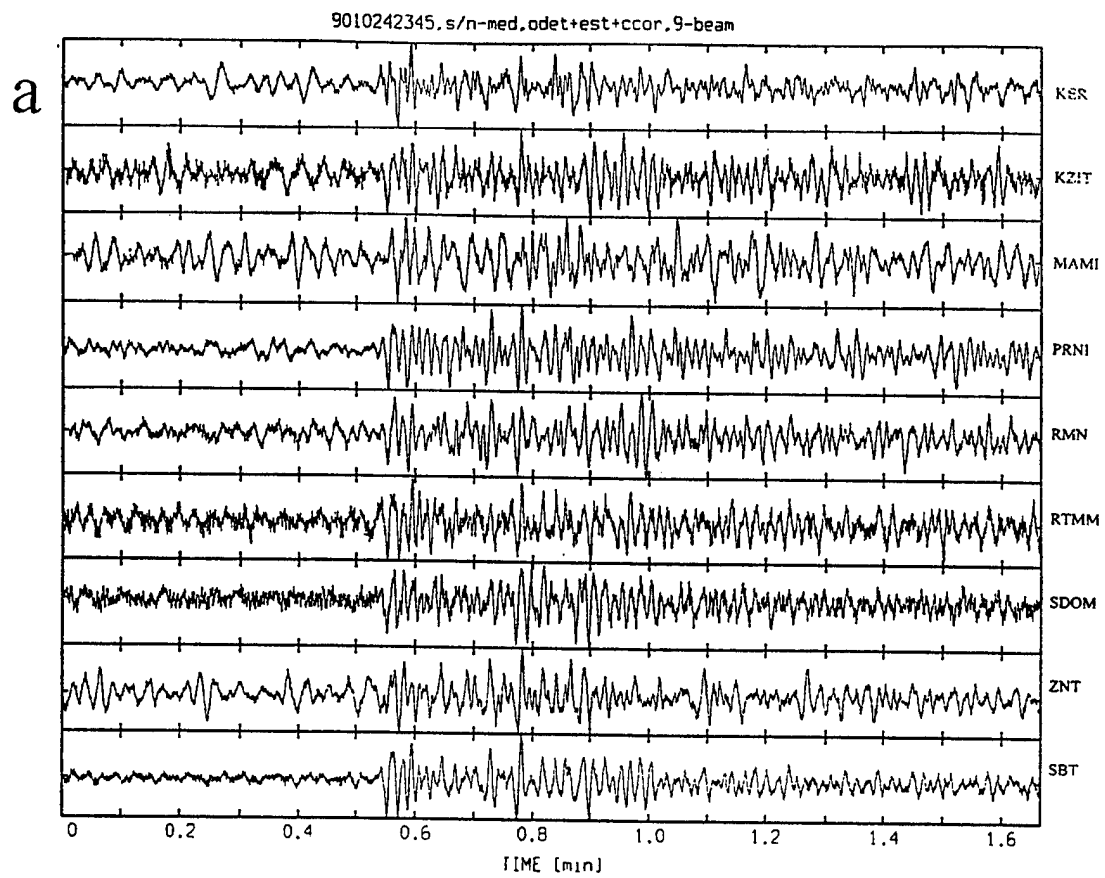
Fig. 36. Aligned records of the small (m_b=5.3) Chinese earthquake QT25 at 8 ISN stations (a); application of SBT and ABT to the subnetwork and comparison with the "best" PRNI station (b).

63

correlation technique (PCT) (Gelchinsky et al., 1985), thus estimating accurately the relative shift between P-wave arrivals to different ISN stations. The OD provides a preliminary estimate of the P-wave shift dT between the stations by evaluating the position of its output maximum (see Fig. 37a). The estimate is corrected by applying the MLOE on the time interval between the trace starting point and the evaluated position of the OD output maximum. Finally, a small uncertainty time interval is used to evaluate the maximum *Phase Correlation Function* for different pairs of records. The final vector shift dT is estimated as the sum of shifts at all three steps. The accuracy of the alignment is checked by stacking the traces (see Fig. 37b). The *Apparent velocity* and *Azimuth* are finally estimated as the least square solution from the system of linear equations

$$SR = dT \qquad (6.3)$$

where S is the unknown slowness and R is the matrix of the stations relative local coordinates $R=(x_j-x_0, y_j-y_0)$. The results of the slowness estimation for two weak teleseismic events (the Semipalatinsk nuclear test NT17, $m_b=5.3$ and the Chinese earthquake QT24, $m_b=5.2$) are presented in Table 5 together with theoretical evaluations from the standard Earth model. Records of the seven stations were used in the first case and 8 stations in the second. From the table it is seen that in spite of the small SNR for many of the channels the estimations of Slowness and Azimuth are very close to the theoretical ones.

Table 5. Slowness and azimuth estimated from the P-phase alignment.

EVENT			EARTH MODEL			REF. STATION			LEAST SQUARE SOLUTION		
No	Lat.	Long.	Dist.	Slow. sec/km	Azim	Name	Lat.	Long.	Slow. sec/km	Azim.	RMS
1	50.08	78.98	36.42	0.081	48.58	ATZ	32.82	35.28	0.079	49.07	0.14
2	44.12	83.86	40.85	0.074	56.50	RMN	30.51	34.63	0.071	56.46	0.43
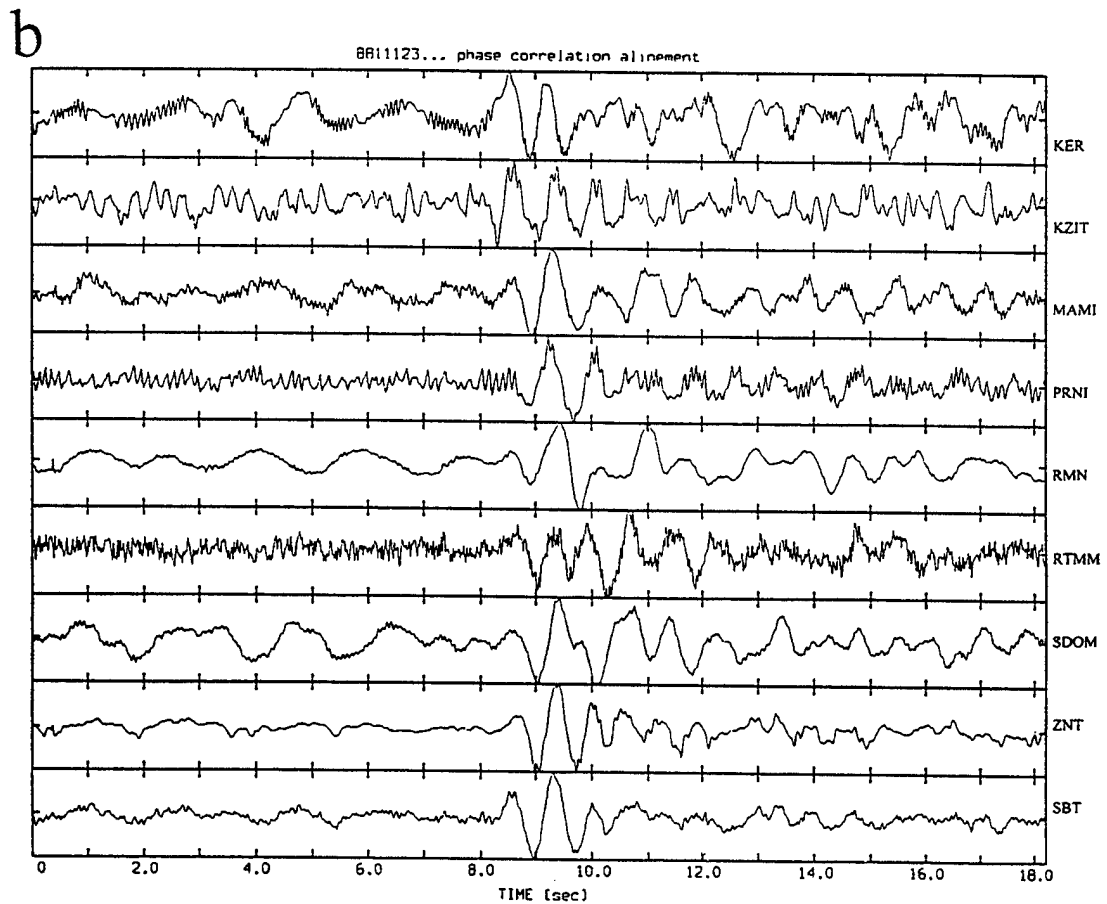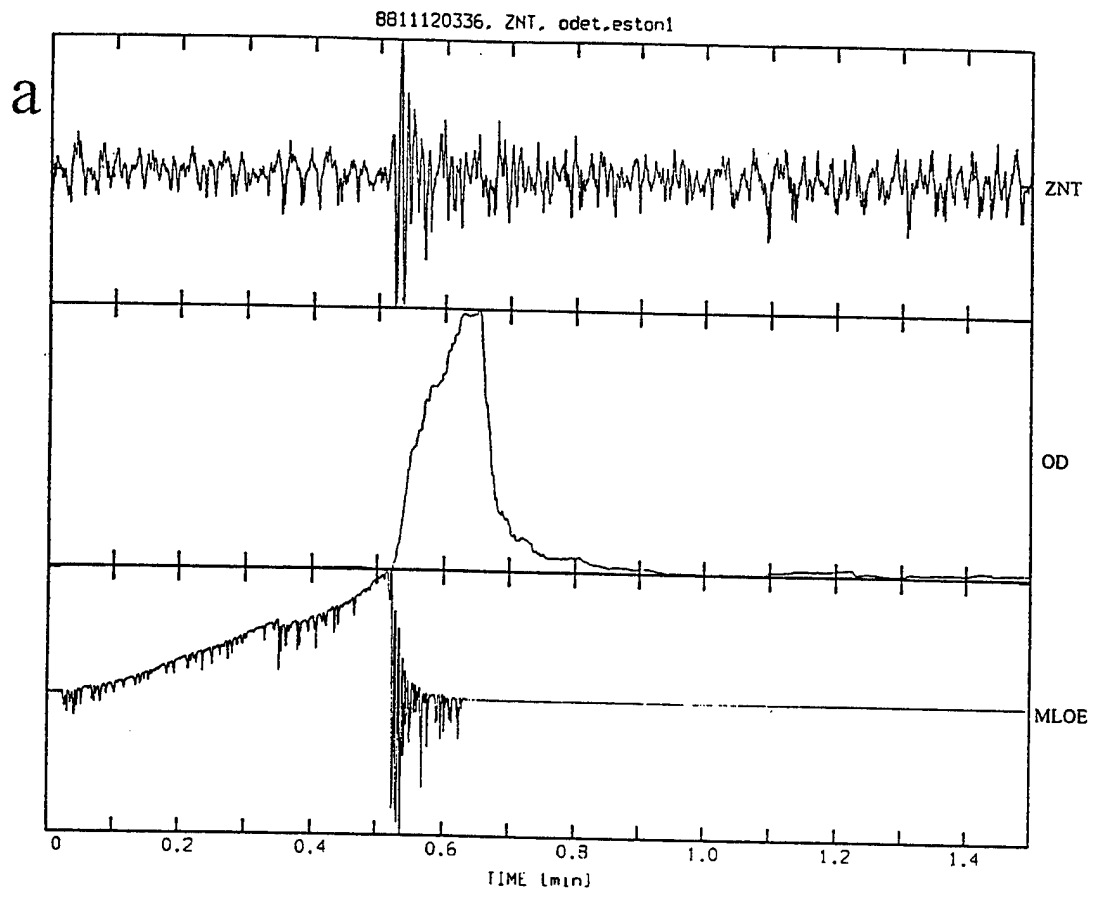
Fig. 37. Apparent velocity and azimuth evaluation for the small Kazakh nuclear test NT17: (a) application of the Optimal Detector (OD) and Maximum Likelihood Onset Estimator (MLOE) to ZNT station of the ISN; (b) the traces alignment for 8 ISN stations by application of phase correlation algorithm (the bottom trace is the stack).

65

Conclusions: Theoretical analysis and experimental results of array technique application to subnetworks of Israel Seismic Network show us that:

- Standard beamforming is hardly useful for enhancing array detection since it may be more reasonable to accept detections from those stations with the best SNR.

- Adaptive beamforming techniques may be useful for teleseismic detection because it provides SNR at the output no worse than the subnetwork best channel; however, computational cost should be additionally analyzed.

- We tested new techniques for estimating the slowness and azimuth of teleseismic events using subnetworks of the ISN and algorithms for detection and alignment of signal traces as well as phase correlation technique. For the two small events with SNR ~ 3 and with known source locations, comparison with theoretical results showed deviation of slowness estimation <0.003 sec/km (0.31 km/sec of apparent velocity) and deviation of azimuth <0.5 deg, corresponding to a location error of about 30-40 km at a distance of 3500-4000 km.

7. CONCLUSIONS AND RECOMMENDATIONS.

The potential of the Israel Seismic Network to contribute to the CTBT in detection, location and identification of clandestine nuclear tests was investigated using seismic signals at local and teleseismic distance ranges. The system was tested for different kinds of local events: ripple-fired and instantaneous quarry blasts, earthquakes and underwater explosions, with considerable success. The magnitude range for regional events was M_L~ (1.0-3.1) and for the Eurasian nuclear tests and distant earthquakes m_b ~ (5.3-6.5).

The success of classification is attributed mainly to the fact that through analysis of dynamic and kinematic features of the mentioned events, we managed to predict theoretically and/or observe characteristic physical phenomena related to the concrete class of sources and to design some statistics based on seismograms or spectra (*velogram parameter C, spectral semblance, energy spectral ratio* and *spectrogram* determined for specific frequency bands, *P/Pcoda*) that most accurately measure these features.

Analysis of the physical phenomena related to explosive sources contributed to correct interpretation of the estimated statistics values and results of discrimination between explosions and earthquakes. Preliminary experimental relationships (charge weight vs magnitude, and peak particle velocity vs scaled distance) for local instantaneous quarry blasts and underwater Dead Sea explosions (demonstrating outstanding high coupling) provide a basis for the design and execution of effective calibration explosions currently lacking in the region.

For the local events the characteristic feature seems to be excitation of Rg, Lg surface waves by the near surface explosive sources, which together with ripple firing in quarry blasts and bubbling effect in the underwater explosions, imply enhancement of low frequencies in signal spectra, spectral modulation and coherency of spectral shapes at different stations. Additional coherency of the local explosions spectra may be attributed to the spherical symmetry of the source.

Teleseismic events are characterized by the impulsive P-onset and shifting of spectral energy to higher frequencies for nuclear detonations. Application of semblance revealed unpredictable larger coherency of earthquake spectral shapes compared to those of nuclear tests, possibly due to scattering effects.

Due to the dense distribution of the ISN stations over Israel, we had an opportunity to accumulate information contained in the ISN records and perform reliable event discrimination. Joint analysis of the above mentioned discriminants and averaging of feature vectors over the ISN sunbetworks provides additional discrimination effects and yields an almost correct separation of both local and teleseismic data bases. Both data bases were large enough to test performance of different automatic classifiers and select the best of them according to minimum error probability estimator criterion: ANN plus averaged *spectrogram* in the first case and LDF plus specific combination of the teleseismic discriminants in the second case.

The relatively dense character of the ISN subnetworks is attractive for the application of array techniques to enhance the network detectability and accuracy of location in far regional and teleseismic ranges. Possible enhancement of the ISN detectability may be achieved by adaptation to the current multichannel noise characteristics and studying the signal propagation characteristics across the ISN subnetworks to provide minimum detour of signal dynamic and kinematic features. As a result of the investigation of the ISN pure noise and weak seismograms of distant events, we proved the advantages of the adaptive beamforming technique over standard beamforming for the detection of teleseismic signals. Attempts to estimate azimuth and apparent velocity of weak teleseismic events were quite successful in the cases tested. The analysis showed that for the purposes of slowness vector estimation, a relatively limited station aperture should be used to avoid influence of regional crustal and mantle inhomogeneities.

For confirmation of the results and implementation of the automated detectors and classifiers in routine data processing, we recommend that they be tested in large scale experiments comprising hundreds of events from different regions.

REFERENCES

Aki, K. and Chouet, B., 1975. Origin of Coda Waves: Source, Attenuation, and Scattering Effects. J. Geoph. Res., Vol. 80, No. 23.

Alexander Shelton, S., Hsu, R.C., Karl, S.L., Gupta, I.N. and Salzberg, D.H., 1995. New techniques for estimating source depth and other diagnostic source characteristics of shallow events from regional observations of P, Lg and Rg signals. Proceedings of 17th Seismic Research Symposium on Monitoring a CTBT, Scottsdale, AZ, 821-830. PL-TR-95-2108, ADA310037

Bakun, W.H., Stewart, R.M. and Bufe, C.G., 1978, Directivity in the high-frequency radiation of small earthquakes, Bull. Seism. Soc. Am., 68, 1253-1263.

Barker, T.G., McLaughlin, K.C. and Stevens, J.L., 1993, Numeral simulation of quarry blast sources, SSS-TR-93-13859, S-Cubed, La Jolla, CA.

Båth, M., 1975. Short-period Rayleigh waves from near-surface events, Phys. Earth. Planet. Inter., 10:369-376.

Baumgardt, D.R. and Young, G.V., 1990, Regional seismic waveform discriminants and case-based event identification using regional arrays, Bull. Seism. Soc. Am., 80:1874-1892.

Baumgardt, D.R., 1996. Characterization of regional phase propagation seismic discriminants for the Middle East, 18th Annual Seismic Research Symposium on Monitoring a CTBT, September 1996, Proceedings, 474-483. PL-TR-96-2153, ADA313692

Bennett, T.J. and Murphy, J.R., 1986, Analysis of seismic discrimination capabilities using regional data from Western United States events, Bull. Seism. Soc. Am., 76:1069-1086.

Dahlman, O. and Israelson, H., 1977. Monitoring Underground Nuclear Explosions, Elsevier, Amsterdam, 440pp.

Dowla, F., 1995. Neural networks in seismic discrimination, in: E.S. Husebye and A.M. Dainty (Eds.) Monitoring a Comprehensive Test Ban Treaty, NATO ASI Series, Series E: Applied Sciences - Vol. 303, 777-790.

Gelchinsky, B., Landa, E. and Shtivelman, V., 1985. Algorithms of Phase and Group Correlation. Geophys., 50:596-608.

Gitterman, Y., 1982, Assessment of dynamic parameters of seismic and air shock waves from multiple shot systems, Ph.D. Thesis, Academy of Sciences of the USSR, Novosibirsk..

Gitterman, Y., Pinsky, V. and Shapira, A., 1996, Discrimination of seismic sources using Israel Seismic Network, Scientific Report No.1, PL-TR-96-2207, Phillips Lab., MA, 98pp. ADA317385

Gitterman, Y. and Shapira, A., 1993, Spectral discrimination of underwater explosions, Isr.J.Earth Sci.,42:37-44.

Ginzburg, A. and Folkman, Y., 1980, The crustal structure between the Dead Sea rift and the Mediterranean Sea, Earth Planet. Sci. Lett., 41:181-188.

Grant, L., Wagner, R., Ryall, F., Rivers,W. and Henson, I., 1997. Ground truth database for regional seismic discrimination research in the Middle East and North Africa, Proceedings of the 19th Symposium on Monitoring a CTBT, Orlando, 867-876.

Fukunaga, K. and Hummels, D.M., 1989. Leave-one-out procedure for nonparametric error estimates, IEEE Trans. Pattern Anal. and Machine Intel., 11:421-423.

Jarpe, S.P., Moran, B., Goldstein, P. and Glenn, L.A., 1996. Implications of mining practices in an open-pit gold mine for monitoring of a Comprehensive Test Ban Treaty, LLNL report UCRL-ID-123017, 35pp.

Hedlin, M., Minster, J.G. and Orcutt, J.A., 1989, The time-frequency characteristics of quarry blasts and calibration explosions recorded in Kazakhstan, USSR, Geophys. J. Int., 99:109-121.

Jost, M., Schweitzer, J. and Harjes, H-P., 1996. Monitoring Nuclear Test Sites with GERESS, Bul. Seism. Soc. Am., 86, No 1A, 172-190.

Kafka, A.L., 1990. Rg as a depth discriminator for earthquakes and explosions: a case study in New England. Bull. Seism. Soc. Am., 80:373-395.

Khalturin, V.L. and Richards, P.G., 1997. The seismic signal strength of chemical explosions, Proceedings of the 19th Symposium on Monitoring a CTBT, Orlando, 632-641.

Kim, W.Y., Simpson, D.W. and Richards, P.G., 1994. High-frequency spectra of regional phases from earthquakes and chemical explosions, Bull. Seis. Soc. Am., 84:1365-1386.

Kulhanek, O., 1971. P wave amplitude spectra of Nevada undergroud nuclear explosions, Pure Appl. Geophys., 88, 121-136.

Kushnir, A.F., Nikiforov, I.V. and Savin, I.V., 1983. Statistical adaptive algorithms for automatic detection of seismic signals, in Computational Seismology, Allerton Press Inc., Vol.13, 146-151.

Kushnir, A.F., Lapshin, V.M., Pinsky, V.I. and Fyen, J., 1990. Statistically optimal event detection using small array data, Bull. Seism. Soc. Am., 80, Part B, 1874-1892.

Lay, T., 1991. Teleseismic manifestations of pP: problems and paradoxes, in Explosion Source Phenomenology, Editors S.R. Taylor, H.J. Patton and P.G. Richards, Geophysical Monograph 65, 109-125.

Leith, W., Adushkin, V. and Spivak, A., 1997. Large mining blasts from the Kursk mining region, Russia, Final Report, USGS/UC-LLL MOA B291532, 35pp.

Li, Y., Toksöz, M.N. and Rodi, W.L., 1996, Discrimination of small earthquakes and explosions, Proceedings of the 18th Symposium on Monitoring a Comprehensive Test Ban Treaty, Annapolis, PL-TR-96-2153, 574-583, ADA313692

Murphy, J.R., Stevens, J.L. and Rimer, N., 1987. High frequency seismic source characteristics of cavity decoupled underground nuclear explosions, Air Force Geophysics Laboratory Tecnical Report, AFGL-TR-88-0130, 51 pp. ADA198121

Mykkeltveit, S., Ringdal, F., Kvarna, T. and Alewein, R.W., 1990. Application of Regional Array in Seismic Verification. Bul. Seism. Soc. Am., 80, Part B, 1777-1800

Neev, D. and Hall, J.K., 1979. Geophysical investigation in the Dead Sea, Sedimentary Geology, 23:209-238.

Neidell, N.S. and Taner, M.T., 1971. Semblance and other coherency measures for multichannel data, Geophysics, 36:482-497.

Pinsky, V. and Shapira, A., 1997. Kinematic Multistation Discriminator Between Local Quarry Blasts and Earthquakes, Geoph. J. Int. (submitted).

Pisarenko, V.F., Kushnir, A.F. and Savin, I.V., 1987. Statistical adaptive algorithms for estimations of onset moments of seismic phases, Phys. Earth Planet. Inter. 47:4-10.

Pomeroy, P.W., Best, J.W. and McEvilly, Th.V., 1982. Test ban treaty verification with regional data - a review, Bull. Seism. Soc. Am., 72, No.6: S89-S129.

Pulli, J.J., 1995. Extracting and processing signal parameters for regional seismic event identification, in: Husebye, E.S. and Dainty, A.S. (eds.), Monitoring a CTBT, NATO ASI Series, 303:741-754.

Ringdal, F., Marshall, P.D. and Allewine, R.W., 1992. Seismic yield determination of Soviet underground nuclear explosions at the Shagan River test site, Geoph. J. Int., 109:65-77.

Savage, J.C., 1972. Relation of corner frequency to fault dimensions, JGR,77,577-592.

Shapira, A., 1988. Magnitude scales for regional earthquakes monitored in Israel, Isr. J. Earth Sci., Vol. 37:17-22.

Shapira, A., Gitterman, Y. and Pinsky, V., 1996. Discrimination of seismic sources using the Israel Seismic Network, Proceedings of the 18th Symposium on Monitoring a Comprehensive Test Ban Treaty, Annapolis, PL-TR-96-2153, 612-621. ADA313692

Stump, B.W. and Reinke, R.E., 1988, Experimental confirmation of superposition from small explosions, Bull. Seism. Soc. Am., 78:1059-1073.

Stump, B.W., Riviere-Barbier, F., Chernoby, I. and Koch, K., 1994. Monitoring a test ban treaty presents scientific challenges, EOS Transactions, Vol. 75, No. 24, June 14, 1994.

Su, F., Aki, K. and Biswas, N.N., 1991. Discriminating quarry blasts from earthquakes using coda waves, Bull. Seis. Soc. Am., 81:162-178.

Suteau-Henson, A. and Bache, T.C., 1988. Spectral characteristics of regional phases recorded at NORESS, Bull. Seis. Soc. Am., 708-725.

Taylor, S.R. and Marshall, P.D., 1991. Spectral discrimination between Soviet explosions and earthquakes using short-period array data, Geophys. J. Int., 106:265-273.

Tsvang, S.L., Pinsky, V.I. and Husebye, E.S., 1993. Enhanced seismic source discrimination using NORESS recordings from Eurasian events, GJI, 112:1-14.

Uski, M., 1990. Event Detection and Location Performance of the FINESA Array in Finland. Application of Regional Array in Seismic Verification. Bul. Seism. Soc. Am., 80, Part B, 1818-1832.

van Eck, T., 1988. Attenuation of coda waves in the Dead Sea region. Bull. Seis. Soc. Am., 78:770-779,.

Wallace, T., Blanford, R., Dainty, A., Lacoss, R., Maxion, R., Ryall, A., Stump, B. and Thurber, C., 1992. Report on the DARPA Seismic Identification Workshop.

Walter, W. R., Mayeda, K.M. and Patton, H.J., 1995. Phase and spectral ratio discrimination between NTS earthquakes and explosions. Part 1: Empirical observations, Bull. Seis. Soc. Am., 85:1050-1067.

Walter, W.R., Hunter, S.L. and Glenn, L.A., 1996. Preliminary report on LLNL mine seismicity deployment at the Twentymile Coal Mine. CTBT Seismic Monitoring Project Task S7.2, Deliverable #2, UCRL-ID-122800.

Walter, W. R., Harris, D.B. and Myers, S.C., 1997. Seismic discrimination between earthquakes and explosions in the Middle East and North Africa, Proceedings of the 19th Symposium on Monitoring a Comprehensive Test Ban Treaty, Orlando, 459-468.

Weinstein, M.S., 1968. Spectra of acoustic and seismic signals generated by underwater explosions during Chase experiment, J. Geoph. Res., 73, No. 16:5473-5476.

Wilburn, D., Francesco, C. and Bleiwas, D., 1996. Estimated use of explosives in the mining industries of Egypt, Jordan, Syria, Tunisia, and Turkey, USGS report UCRL-CR-125620, prepared for U.S. Department of Energy.

Willis, D.E., 1963. Seismic measurements of large underwater shots, Bull. Seism. Soc. Am., 53:789.

Wuster, J., 1993. Discrimination of chemical explosions and earthquakes in Central Europe - a case study, Bull. Seis. Soc. Am., 83:1184-1212.

APPENDIX A

Tables of teleseismic database and discrimination results.

Table A1. Underground nuclear tests used in the study.

	Location	Date hrmnsec	Lat, deg	Long, deg	Dist, deg	Azim, deg	m_b
*NT1	Kazakh	850615 005700.7	49.889	78.881	37	47	6.0
*NT2	Kazakh	850720 005314.5	49.951	78.829	37	47	5.9
*NT3	Kazakh	870312 015717.3	49.932	78.785	36	47	5.4
*NT4	Kazakh	870417 010304.8	49.886	78.691	36	47	6.0
*NT5	Kazakh	870506 040205.5	49.777	78.089	36	47	5.5
*NT6	China	870605 045958.3	41.584	88.737	43	61	6.2
NT7	Kazakh	870606 023706.9	49.865	78.143	36	47	5.4
*NT8	Kazakh	870802 005806.8	49.880	78.917	37	47	5.9
*NT9	Kazakh	871115 033106.7	49.871	78.791	36	47	6.0
NT10	Kazakh	871213 032104.8	49.989	78.844	37	47	6.1
NT11	Kazakh	871227 030504.7	49.864	78.758	36	47	6.1
NT12	Kazakh	880213 030505.9	49.954	78.910	37	47	6.1
NT13	Kazakh	880403 013305.8	49.917	78.945	37	47	6.1
NT14	Kazakh	880504 005706.8	49.928	78.769	36	47	6.1
NT15	W.Siberia	880822 161958.2	66.316	78.548	43	23	5.3
NT16	Kazakh	880914 035957.4	49.833	78.808	36	47	6.1
NT17	Kazakh	881112 033003.7	50.078	78.988	37	47	5.3
NT18	Nov.Zemlya	881204 051953.0	73.387	54.998	42	8	5.9
NT19	Kazakh	881217 041806.9	49.886	78.926	37	47	5.9
NT20	Kazakh	890122 035706.5	49.915	78.857	37	47	6.0
NT21	Kazakh	890212 041506.7	49.895	78.758	36	47	5.9
NT22	Nov.Zemlya	901024 145758.1	73.361	54.707	42	8	5.7
NT23	China	920521 045957.5	41.604	88.813	43.6	61	6.5
NT24	China	931005 015956.5	41.647	88.681	43	61	5.9
NT25	China	940610 062557.8	41.527	88.710	43.5	61	5.8
NT26	China	941007 032558.1	41.662	88.753	43.5	61	6.0
NT27	China	950515 040558.0	41.665	88.821	43.6	61	6.1
NT28	China	950817 010004.8	41.600	88.700	43.5	61	6.0
*NT29	China	960608 025558.0	41.600	88.600	43.4	61	6.0

Table A2. Selected Eurasian earthquakes.

No.	Location	Date hrmnsec	Lat, deg	Long, deg	Depth, km	Dist, deg	Azim, deg	m_b
*QT1	Uzbek	840319 202838.2	40.320	63.350	15	24	61	6.5
*QT2	Tajik	841026 202221.8	39.155	71.328	33	30	65	6.0
QT3	China	850823 124156.1	39.431	75.224	7	33	65	6.4
*QT4	China	850911 204549.5	39.356	75.407	15	33	65	5.8
QT5	Tajik	851013 155951.2	40.301	69.823	16	29	63	5.8
**QT6	Uzbek	860325 234934.4	40.336	63.658	33	24	61	5.2
*QT7	Afghanistan	860426 141507.6	36.495	71.114	187	29	71	5.6
*QT8	Afghanistan	860821 013417.3	36.472	71.083	235	29	71	5.4
*QT9	Afghanistan	860915 214229.2	36.714	71.092	89	29	70	5.8
QT10	Afghanistan	860917 120809.4	37.290	71.730	120	30	69	5.5
*QT11	China	870225 195636.4	38.029	91.144	33	45	66	5.7
*QT12	China	870430 051737.1	39.770	74.590	9	32	64	5.7
*QT13	China	870918 215836.6	47.276	89.674	33	43	53	5.3
*QT14	Afghanistan	871003 110005.2	36.454	71.437	95	30	71	5.9
*QT15	Tajik	880326 225842.8	38.309	73.234	121	31	67	5.7
QT16	Tajik	880720 062051.4	37.028	72.914	41	31	69	5.5
QT17	Afghanistan	880806 090321.9	36.461	71.043	195	29	71	6.1
QT18	Afghanistan	880909 211236.1	36.483	71.381	188	30	71	5.4
QT19	China	880923 044640.6	39.570	74.506	33	32	65	5.3
QT20	Afghanistan	880926 071700.2	36.294	71.374	107	30	71	5.6
QT21	Afghanistan	900205 051645.1	37.047	71.250	110	30	69	6.1
QT22	China	900417 015933.4	39.436	74.900	33	32	65	6.0
*QT23	Kazakh-China	900803 091539.6	47.949	84.958	19	40	51	6.1
QT24	China	901024 233815.1	44.117	83.856	20	39	57	5.2
QT25	China	901024 234657.6	44.119	83.876	22	39	57	5.3
*QT26	China	910819 060553.0	46.954	85.333	44	40	53	5.7
**QT27	China	930202 160510.7	42.212	86.126	10	41	60	5.7
QT28	Afghanistan	930918 050227.2	36.369	71.600	117	30	71	6.1
QT29	China	931002 084232.8	38.141	88.638	16	43	66	6.3
QT30	Tibet	860110 034629.9	28.648	86.527	55	44	80	5.4
QT31	Tibet	860620 171246.9	31.240	86.847	33	43	76	5.9
QT32	China	860826 094300.3	37.724	101.496	8	53	64	6.2
QT33	China	870810 121217.8	38.118	106.357	10	57	62	5.4
QT34	N.China	880103 213225.5	38.111	106.336	14	57	62	5.5
QT35	China	881105 021430.3	34.354	91.880	8	47	70	5.9
QT36	Kirgiz	881221 082103.7	41.220	72.298	33	31	61	5.4

74

QT37	China	890922 022553.5	31.545	102.464	33	56	71	6.0
QT38	China	891102 072239.2	36.206	106.346	10	57	64	5.0
QT39	China	900114 030319.2	37.819	91.971	12	46	66	6.1
QT40	Tibet	900602 003235.0	32.432	92.743	13	48	73	5.6
QT41	Kazakh-China	900927 211232.5	47.903	84.961	33	40	51	5.0

* - only ISN data are presented, ** - only NORESS data are presented.

Table A3. Majority voting analysis for the ISN teleseismic recordings with (0.5 - 5 Hz) prefiltering.

Nuclear tests			P/Pcoda		Semblance 1		Spec. Ratio 1		
No	Location	Depth	value	thr.=2.3	value	thr.=0.65	value	thr.=0.9	Voting
NT1	Kazach	0	3.844	+	0.311	+	0.32	+	3:0
NT 2	Kazakh	0	3.639	+	0.139	+	0.395	+	3:0
NT 3	Kazakh	0	3.781	+	0.551	+	0.317	+	3:0
NT 4	Kazakh	0	4.260	+	0.440	+	0.703	+	3:0
NT 5	Kazakh	0	4.400	+	0.665	+	0.455	+	3:0
NT 6	China	0	2.740	+	0.352	+	0.194	+	3:0
NT 7	Kazakh	0	2.563	+	0.391	+	0.376	+	3:0
NT 8	Kazakh	0	4.274	+	0.788	-	0.497	+	2:1
NT 9	Kazakh	0	4.302	+	0.348	+	0.403	+	3:0
NT 10	Kazakh	0	4.808	+	0.237	+	0.561	+	3:0
NT 11	Kazakh	0	4.253	+	0.336	+	0.662	+	3:0
NT 12	Kazakh	0	3.954	+	0.590	+	0.606	+	3:0
NT 13	Kazakh	0	4.499	+	0.456	+	0.419	+	3:0
NT 14	Kazakh	0	4.029	+	0.153	+	0.241	+	3:0
NT 15	W.Sib.	0	3.763	+	0.687	+	0.156	+	3:0
NT 16	Kazakh	0	3.317	+	0.696	-	0.349	+	2:1
NT 17	Kazakh	0	4.936	+	0.661	-	0.159	+	2:1
NT 18	N.Zemla	0	2.842	+	0.473	+	0.791	+	3:0
NT 19	Kazakh	0	5.430	+	0.617	+	0.488	+	3:0
NT 20	Kazakh	0	4.280	+	0.433	+	0.607	+	3:0
NT 21	Kazakh	0	4.241	+	0.366	+	0.667	+	3:0
NT 22	N.Zemlya	0	3.400	+	0.499	+	0.995	-	2:1
NT 23	China	0	2.430	+	0.420	+	0.378	+	3:0
NT 24	China	0	3.890	+	0.429	+	0.246	+	3:0
NT 25	China	0	4.142	+	0.323	+	0.262	+	3:0
NT 26	China	0	3.726	+	0.568	+	0.223	+	3:0
NT 27	China	0	3.800	+	0.399	+	0.201	+	3:0
NT 28	China	0	3.990	+	0.362	+	0.252	+	3:0
NT 29	China	0	3.611	+	0.635	+	0.336	+	3:0
Number of errors :				**0**		**5**		**1**	

Table A3. Continuation.

No.	Location	Depth	P/Pcoda value	thr.=2.3	Semblance 1 value	thr.=0.65	Spectral ratio 1 value	thr.=0.9	Voting
QT1	Uzbek	15	1.028	+	0.832	+	1.945	+	3:00
QT 2	Tajik	33	1.915	+	0.788	+	1.802	+	3:0
QT 3	China	7	0.802	. +	0.717	+	1.560	+	3:0
QT 4	China	15	1.255	+	0.909	+	1.858	+	3:0
QT 5	Tajik	16	1.331	+	0.771	+	3.577	+	3:0
QT 6	Uzbek	33	-	-	-	-	-	-	-
QT 7	Afghan	187	2.42	-	0.942	+	4.819	+	2:1
QT 8	Afghan	235	3.74	-	0.801	+	1.774	+	2:1
QT 9	Afghan	89	1.12	+	0.679	+	1.017	+	3:0
QT 10	Afghan	120	3.85	-	0.595	-	1.227	+	1:2
QT 11	China	33	2.160	+	0.891	+	3.606	+	3:0
QT 12	China	9	1.384	+	0.871	+	5.439	+	3:0
QT 13	China	33	1.307	+	0.808	+	2.927	+	3:0
QT 14	Afghan	95	1.89	+	0.792	+	3.222	+	3:0
QT 15	Tajik	121	4.16	-	0.947	+	1.737	+	2:1
QT 16	Tajik	41	1.352	+	0.840	+	2.759	+	3:0
QT 17	Afghan	195	1.76	+	0.600	-	1.739	+	2:1
QT 18	Afghan	188	3.76	-	0.914	+	4.352	+	2:1
QT 19	China	33	1.733	+	0.777	+	1.001	+	3:0
QT 20	Afghan	107	2.8	-	0.674	+	1.645	+	2:1
QT 21	Afghan	110	1.93	+	0.823	+	0.310	-	2:1
QT 22	China	33	1.304	+	0.886	+	7.050	+	3:0
QT 23	Kaz	19	1.241	+	0.651	+-	1.804	+	2:1
QT 24	China	20	1.330	+	0.681	+	0.938	+	3:0
QT 25	China	22	1.188	+	0.569	-	0.691	-	1:2
QT 26	China	44	1.763	+	0.529	+	0.999	+	3:0
QT 27	China	10	-	-	-	-	-	-	-
QT 28	Afghan	117	1.66	+	0.748	+	2.233	+	3:0
QT 29	China	16	1.288	+	0.634	-	1.965	+	2:1
QT 30	Tibet	55	3.360	-	0.548	-	0..691	-	0:3
QT 31	Tibet	33	2.232	+	0.885	+	3.732	+	3:0
QT 32	China	8	1.973	+	0.840	+	3.022	+	3:0
QT 33	China	10	0.543	+	0.855	+	1.573	+	3:0
QT 34	N.China	14	1.506	+	0.769	+	2.775	+	3:0
QT 35	China	8	1.375	+	0.865	+	5.754	+	3:0
QT 36	Kirgiz	33	4.522	-	0.785	+	0.659	-	1:2
QT 37	China	33	1.118	+	0.762	+	2.347	+	3:0
QT 38	China	10	3.301	-	0.815	+	0.774	-	1:2
QT 39	China	12	1.351	+	0.871	+	1.519	+	3:0
QT 40	Tibet	13	1.108	+	0.739	+	1.272	+	3:0
QT 41	Kaz-China	33	1.238	+	0.831	+	0.191	-	2:1
Number of errors: shallow/all			**2/7**		**2.5/3**		**2/4**		

Table A4. Majority voting analysis for the ISN teleseismic recordings without prefiltering.

Nuclear tests			P/Pcoda		Semblance 2		Spectral Ratio 2		
No.	Location	Depth	value	thr.=2.3	value	thr.=0.8	value	thr.=1.6	Voting
NT1	Kazach	0	3.844	+	0.537	+	0.853	+	3:0
NT 2	Kazakh	0	3.639	+	0.434	+	0.821	+	3:0
NT 3	Kazakh	0	3.781	+	0.638	+	0.676	+	3:0
NT 4	Kazakh	0	4.260	+	0.760	+	1.870	-	2:1
NT 5	Kazakh	0	4.400	+	0.782	+	0.988	+	3:0
NT 6	China	0	2.740	+	0.104	+	0.483	+	3:0
NT 7	Kazakh	0	2.563	+	0.656	+	1.003	+	3:0
NT 8	Kazakh	0	4.274	+	0.870	-	1.183	+	2:1
NT 9	Kazakh	0	4.302	+	0.615	+	1.075	+	3:0
NT 10	Kazakh	0	4.808	+	0.588	+	1.568	+	3:0
NT 11	Kazakh	0	4.253	+	0.678	+	1.701	-	2:1
NT 12	Kazakh	0	3.954	+	0.770	+	1.648	-	2:1
NT 13	Kazakh	0	4.499	+	0.681	+	1.331	+	3:0
NT 14	Kazakh	0	4.029	+	0.349	+	0.895	+	3:0
NT 15	W.Sib.	0	3.763	+	0.670	+	0.530	+	3:0
NT 16	Kazakh	0	3.317	+	0.794	+-	0.843	+	2:1
NT 17	Kazakh	0	4.936	+	0.599	+	0.387	+	3:0
NT 18	N.Zemlya	0	2.842	+	0.840	-	3.226	-	1:2
NT 19	Kazakh	0	5.430	+	0.752	+	1.364	+	3:0
NT 20	Kazakh	0	4.280	+	0.623	+	1.805	-	3:0
NT 21	Kazakh	0	4.241	+	0.491	+	1.200	+	3:0
NT 22	N.Zemlya	0	3.400	+	0.763	+	2.560	-	2:1
NT 23	China	0	2.430	+	0.595	+	1.103	+	3:0
NT 24	China	0	3.890	+	0.174	+	0.606	+	3:0
NT 25	China	0	4.142	+	0.463	+	0.696	+	3:0
NT 26	China	0	3.726	+	0.442	+	0.489	+	3:0
NT 27	China	0	3.800	+	0.243	+	0.498	+	3:0
NT 28	China	0	3.990	+	0.321	+	0.584	+	3:0
NT 29	China	0	3.611	+	0.491	+	0.676	+	3:0
Number of errors :				**0**		**2**		**6**	

Table A4. Continuation.

Eartquakes			P/Pcoda		Semblance 2		Spec.ratio 2		
No.	Location	Depth	value	thr.=2.3	value	thr.=0.8	value	thr.=1.6	Voting
QT1	Uzbek	15	1.028	+	0.920	+	4.93	+	3:0
QT 2	Tajik	33	1.915	+	0.880	+	5.40	+	3:0
QT 3	China	7	0.802	+	0.863	+	3.78	+	3:0
QT 4	China	15	1.255	+	0.940	+	4.49	+	3:0
QT 5	Tajik	16	1.331	+	0.925	+	9.81	+	3:0
QT 6	Uzbek	33	-	-	-	-	-	-	-
QT 7	Afghan	187	2.42	-	0.960	+	11.46	+	2:1
QT 8	Afghan	235	3.74	-	0.903	+	4.34	+	2:1
QT 9	Afghan	89	1.12	+	0.876	+	3.63	+	3:0
QT 10	Afghan	120	3.85	-	0.820	+	4.01	+	2:1
QT 11	China	33	2.160	+	0.935	+	11.32	+	3:0
QT 12	China	9	1.384	+	0.933	+	10.73	+	3:0
QT 13	China	33	1.307	+	0.874	+	6.43	+	3:0
QT 14	Afghan	95	1.89	+	0.901	+	12.69	+	3:0
QT 15	Tajik	121	4.16	-	0.967	+	4.13	+	2:1
QT 16	Tajik	41	1.352	+	0.943	+	5.95	+	3:0
QT 17	Afghan	195	1.76	+	0.832	+	5.36	+	2:1
QT 18	Afghan	188	3.76	-	0.946	+	13.26	+	2:1
QT 19	China	33	1.733	+	0.884	+	3.08	+	3:0
QT 20	Afghan	107	2.8	-	0.837	+	3.72	+	2:1
QT 21	Afghan	110	1.93	+	0.882	+	0.84	-	2:1
QT 22	China	33	1.304	+	0.945	+	28.35	+	3:0
QT 23	Kazach	19	1.241	+	0.854	+-	6.35	+	2:1
QT 24	China	20	1.330	+	0.877	+	2.64	+	3:0
QT 25	China	22	1.188	+	0.811	+	1.17	-	2:1
QT 26	China	44	1.763	+	0.811	+	3.70	+	3:0
QT 27	China	10	-	-	-	-	-	-	-
QT 28	Afghan	117	1.66	+	0.904	+	10.99	+	3:0
QT 29	China	16	1.288	+	0.843	+	6.48	+	2:1
QT 30	Tibet	55	3.36	-	0.720	-	1.843	+	1:2
QT 31	Tibet	33	0.31	+	0.935	+	13.82	+	3:0
QT 32	China	8	1.973	+	0.917	+	11.14	+	3:0
QT 33	China	10	0.543	+	0.907	+	3.673	+	3:0
QT 34	N.China	14	1.506	+	0.861	+	6.26	+	3:0
QT 35	China	8	1.375	+	0.922	+	17.22	+	3:0
QT36	Kirgiz	33	4.52	-	0.878	+	1.722	+	2:1
QT 37	China	33	1.118	+	0.886	+	8.965	+	3:0
QT 38	China	10	3.301	-	0.903	+	1.866	+	2:1
QT 39	China	12	1.351	+	0.923	+	3.999	+	3:0
QT 40	Tibet	13	1.107	+	0.883	+	3.86	+	3:0
QT 41	Kaz-Chi	33	1.238	+	0.883	+	0.550	-	3:0
Number of errors: shallow/all			2/7		0/1		1/3		

THOMAS AHRENS
SEISMOLOGICAL LABORATORY 252-21
CALIFORNIA INST. OF TECHNOLOGY
PASADENA, CA 91125

AIR FORCE RESEARCH LABORATORY
ATTN: VSOE
29 RANDOLPH ROAD
HANSCOM AFB, MA 01731-3010
(2 COPIES)

AIR FORCE RESEARCH LABORATORY
ATTN: RESEARCH LIBRARY/TL
5 WRIGHT STREET
HANSCOM AFB, MA 01731-3004

AIR FORCE RESEARCH LABORATORY
ATTN: AFRL/SUL
3550 ABERDEEN AVE SE
KIRTLAND AFB, NM 87117-5776
(2 COPIES)

RALPH ALEWINE
NTPO
1901 N. MOORE STREET, SUITE 609
ARLINGTON, VA 22209

MUAWIA BARAZANGI
INSTOC
3126 SNEE HALL
CORNELL UNIVERSITY
ITHACA, NY 14853

T.G. BARKER
MAXWELL TECHNOLOGIES
8888 BALBOA AVE.
SAN DIEGO, CA 92123-1506

DOUGLAS BAUMGARDT
ENSCO INC.
5400 PORT ROYAL ROAD
SPRINGFIELD, VA 22151

THERON J. BENNETT
MAXWELL TECHNOLOGIES
11800 SUNRISE VALLEY DRIVE, STE 1212
RESTON, VA 22091

WILLIAM BENSON
NAS/COS
ROOM HA372
2001 WISCONSIN AVE. NW
WASHINGTON DC 20007

JONATHAN BERGER
UNIVERSITY OF CA, SAN DIEGO
SCRIPPS INST. OF OCEANOGRAPHY
IGPP, 0225
9500 GILMAN DRIVE
LA JOLLA, CA 92093-0225

ROBERT BLANDFORD
AFTAC
1300 N. 17TH STREET
SUITE 1450
ARLINGTON, VA 22209-2308

LESLIE A. CASEY
DEPT. OF ENERGY/NN-20
1000 INDEPENDENCE AVE. SW
WASHINGTON DC 20585-0420

CENTER FOR MONITORING RESEARCH
ATTN: LIBRARIAN
1300 N. 17th STREET, SUITE 1450
ARLINGTON, VA 22209

ANTON DAINTY
HQ DSWA/PMA
6801 TELEGRAPH ROAD
ALEXANDRIA, VA 22310-3398

CATHERINE DE GROOT-HEDLIN
UNIV. OF CALIFORNIA, SAN DIEGO
INST. OF GEOP. & PLANETARY PHYSICS
8604 LA JOLLA SHORES DRIVE
SAN DIEGO, CA 92093

DTIC
8725 JOHN J. KINGMAN ROAD
FT BELVOIR, VA 22060-6218 (2 COPIES)

DIANE DOSER
DEPT OF GEOLOGICAL SCIENCES
THE UNIVERSITY OF TEXAS AT EL PASO
EL PASO, TX 79968

MARK D. FISK
MISSION RESEARCH CORPORATION
735 STATE STREET
P.O. DRAWER 719
SANTA BARBARA, CA 93102-0719

LORI GRANT
MULTIMAX, INC.
311C FOREST AVE. SUITE 3
PACIFIC GROVE, CA 93950

HENRY GRAY
SMU STATISTICS DEPARTMENT
P.O. BOX 750302
DALLAS, TX 75275-0302

I. N. GUPTA
MULTIMAX, INC.
1441 MCCORMICK DRIVE
LARGO, MD 20774

DAVID HARKRIDER
BOSTON COLLEGE
INSTITUTE FOR SPACE RESEARCH
140 COMMONWEALTH AVENUE
CHESTNUT HILL, MA 02167

THOMAS HEARN
NEW MEXICO STATE UNIVERSITY
DEPARTMENT OF PHYSICS
LAS CRUCES, NM 88003

MICHAEL HEDLIN
UNIV. OF CALIFORNIA, SAN DIEGO
SCRIPPS INST. OF OCEANOGRAPHY
IGPP, 0225
9500 GILMAN DRIVE
LA JOLLA, CA 92093-0225

DONALD HELMBERGER
CALIFORNIA INST. OF TECHNOLOGY
DIV. OF GEOL. & PLANETARY SCIENCES
SEISMOLOGICAL LABORATORY
PASADENA, CA 91125

EUGENE HERRIN
SOUTHERN METHODIST UNIVERSITY
DEPARTMENT OF GEOLOGICAL
SCIENCES
DALLAS, TX 75275-0395

ROBERT HERRMANN
ST. LOUIS UNIVERSITY
DEPT OF EARTH & ATMOS. SCIENCES
3507 LACLEDE AVENUE
ST. LOUIS, MO 63103

VINDELL HSU
HQ/AFTAC/TTR
1030 S. HIGHWAY A1A
PATRICK AFB, FL 32925-3002

RONG-SONG JIH
HQ DSWA/PMA
6801 TELEGRAPH ROAD
ALEXANDRIA, VA 22310-3398

THOMAS JORDAN
MASS. INST. OF TECHNOLOGY
BLDG 54-918
77 MASSACHUSETTS AVENUE
CAMBRIDGE, MA 02139

LAWRENCE LIVERMORE NAT'L LAB
ATTN: TECHNICAL STAFF (PLS ROUTE)
PO BOX 808, MS L-175
LIVERMORE, CA 94551

LAWRENCE LIVERMORE NAT'L LAB
ATTN: TECHNICAL STAFF (PLS ROUTE)
PO BOX 808, MS L-208
LIVERMORE, CA 94551

LAWRENCE LIVERMORE NAT'L LAB
ATTN: TECHNICAL STAFF (PLS ROUTE)
PO BOX 808, MS L-202
LIVERMORE, CA 94551

LAWRENCE LIVERMORE NAT'L LAB
ATTN: TECHNICAL STAFF (PLS ROUTE)
PO BOX 808, MS L-195
LIVERMORE, CA 94551

LAWRENCE LIVERMORE NAT'L LAB
ATTN: TECHNICAL STAFF (PLS ROUTE)
PO BOX 808, MS L-205
LIVERMORE, CA 94551

LAWRENCE LIVERMORE NAT'L LAB
ATTN: TECHNICAL STAFF (PLS ROUTE)
PO BOX 808, MS L-200
LIVERMORE, CA 94551

LAWRENCE LIVERMORE NAT'L LAB
ATTN: TECHNICAL STAFF (PLS ROUTE)
PO BOX 808, MS L-221
LIVERMORE, CA 94551

THORNE LAY
UNIV. OF CALIFORNIA, SANTA CRUZ
EARTH SCIENCES DEPARTMENT
EARTH & MARINE SCIENCE BUILDING
SANTA CRUZ, CA 95064

ANATOLI L. LEVSHIN
DEPARTMENT OF PHYSICS
UNIVERSITY OF COLORADO
CAMPUS BOX 390
BOULDER, CO 80309-0309

JAMES LEWKOWICZ
WESTON GEOPHYSICAL CORP.
325 WEST MAIN STREET
NORTHBORO, MA 01532

LOS ALAMOS NATIONAL LABORATORY
ATTN: TECHNICAL STAFF (PLS ROUTE)
PO BOX 1663, MS F659
LOS ALAMOS, NM 87545

LOS ALAMOS NATIONAL LABORATORY
ATTN: TECHNICAL STAFF (PLS ROUTE)
PO BOX 1663, MS F665
LOS ALAMOS, NM 87545

LOS ALAMOS NATIONAL LABORATORY
ATTN: TECHNICAL STAFF (PLS ROUTE)
PO BOX 1663, MS C335
LOS ALAMOS, NM 87545

GARY MCCARTOR
SOUTHERN METHODIST UNIVERSITY
DEPARTMENT OF PHYSICS
DALLAS, TX 75275-0395

KEITH MCLAUGHLIN
CENTER FOR MONITORING RESEARCH
SAIC
1300 N. 17TH STREET, SUITE 1450
ARLINGTON, VA 22209

BRIAN MITCHELL
DEPT OF EARTH & ATMOS. SCIENCES
ST. LOUIS UNIVERSITY
3507 LACLEDE AVENUE
ST. LOUIS, MO 63103

RICHARD MORROW
USACDA/IVI
320 21ST STREET, N.W.
WASHINGTON DC 20451

JOHN MURPHY
MAXWELL TECHNOLOGIES
11800 SUNRISE VALLEY DRIVE, STE 1212
RESTON, VA 22091

JAMES NI
NEW MEXICO STATE UNIVERSITY
DEPARTMENT OF PHYSICS
LAS CRUCES, NM 88003

ROBERT NORTH
CENTER FOR MONITORING RESEARCH
1300 N. 17th STREET, SUITE 1450
ARLINGTON, VA 22209

OFFICE OF THE SECRETARY OF DEFENSE
DDR&E
WASHINGTON DC 20330

JOHN ORCUTT
INST. OF GEOPH. & PLANETARY PHYSICS
UNIV. OF CALIFORNIA, SAN DIEGO
LA JOLLA, CA 92093

PACIFIC NORTHWEST NAT'L LAB
ATTN: TECHNICAL STAFF (PLS ROUTE)
PO BOX 999, MS K6-48
RICHLAND, WA 99352

PACIFIC NORTHWEST NAT'L LAB
ATTN: TECHNICAL STAFF (PLS ROUTE)
PO BOX 999, MS K6-40
RICHLAND, WA 99352

PACIFIC NORTHWEST NAT'L LAB
ATTN: TECHNICAL STAFF (PLS ROUTE)
PO BOX 999, MS K6-84
RICHLAND, WA 99352

PACIFIC NORTHWEST NAT'L LAB
ATTN: TECHNICAL STAFF (PLS ROUTE)
PO BOX 999, MS K5-12
RICHLAND, WA 99352

FRANK PILOTTE
HQ AFTAC/TT
1030 S. HIGHWAY A1A
PATRICK AFB, FL 32925-3002

KEITH PRIESTLEY
DEPARTMENT OF EARTH SCIENCES
UNIVERSITY OF CAMBRIDGE
MADINGLEY RISE, MADINGLEY ROAD
CAMBRIDGE, CB3 0EZ UK

JAY PULLI
BBN SYSTEMS AND TECHNOLOGIES, INC.
1300 NORTH 17TH STREET
ROSSLYN, VA 22209